Wide Bandwidth Film Bulk Acoustic Wave Resonator for Ku-band Filters

Submitted by

Nurul Izza Mohd Nor

M. Eng Microelectronics
B. Eng (Honours) Microelectronics

A thesis submitted in total fulfilment
of the requirements for the degree of

Doctor of Philosophy

School of Engineering and Mathematical Science

Faculty of Science, Technology and Engineering

La Trobe University
Bundoora, Victoria 3086
Australia

March 2013

…"Surely, we have granted you an open victory. So that God may forgive you of your previous and subsequent faults, and may complete His favour upon you, and may guide you to a straight path, and so that God may support you with a mighty support"…

…."This thesis is dedicated to my beloved husband Ayob Nazmy Nanyan, my dear son Muhammad Adam Izhan, my parents and family for their endless, unconditional support and prayers"….

TABLE OF CONTENTS

LIST OF FIGURES

LIST OF TABLES

LIST OF ACRONYMS

Al	Aluminium Nitride
AlN	Aluminium
Au	Gold
BAW	Bulk Acoustic Wave
BPF	Bandpass Filter
BVD	Butterworth Van Dyke
BW	Bandwidth
CdS	Cadmium Sulphide
CMOS	Complementary Metal Oxide Semiconductor
CPW	Coplanar Waveguide
CRF	Coupled Resonator Filters
DC	Direct Current
DGS	Defect Ground Structure
FBAR	Film Bulk Acoustic Wave Resonator
FEM	Finite Element Method
FOM	Figure of Merit
FPGA	Field-Programmable Gate Array
IC	Integrated Circuit
IDT	Interdigital Transducer
IF	Intermediate Frequency
I_L	Insertion Loss
IT	Information Technology
k^2_{eff}	Electromechanical Coupling Coefficient
KLM	Krimholtz-Leedom-Matthaei
LNA	Low-noise Amplifier
LoC	Lab-on-Chip

LTCC	Low Temperature Co-fired Ceramic
RF	Radio Frequency
MEMS	Micro-electro Mechanical System
μTAS	Micro Total Analysis Systems
MMIC	Microwave Monolithic Integrated Circuit
Mo	Molybdenum
MOS	Metal Oxide Semiconductor
NEMS	Nano-electro Mechanical System
NF	Noise Figure
ODU	Outdoor Unit
OoB	Out-of-Band
PA	Power Amplifier
PCB	Printed Circuit Board
Pt	Platinum
PZT	Lead Zirconate Titanate
PSN	Pseudorandom Noise
Q	Charge
Q factor	Quality Factor
Q_p	Parallel Quality Factor
Q_s	Series Quality Factor
RIE	Reactive Ion Etch
RF	Radio Frequency
Ru	Ruthenium
SAW	Surface Acoustic Wave
SCF	Stacked Crystal Filters
SiGe	Silicon Germanium
SMR	Solidly Mounted Resonator
SIP	System in Package
SOC	System on Chip

SOP	System on Package
S-parameters	Scattering-parameters
Ti	Titanium
VCO	Voltage-Controlled Oscillator
VSAT	Very Small Aperture Terminal
W	Tungsten
WiFi	Wireless Fidelity
WiMAX	Worldwide Interoperability for Microwave Access
WLAN	Wireless Local Area Network
WPAN	Wireless Personal Area Network
ZnO	Zinc Oxide

STATEMENT OF AUTHORSHIP

Except where reference is made in the text of the thesis, this thesis contains no material published elsewhere or extracted in whole or in part from a thesis submitted for the award of any other degree or diploma.

No other person's work has been used without due acknowledgement in the main text of the thesis.

The thesis has not been submitted for the award of any degree or diploma in any other tertiary institution.

20/03/2013

Nurul Izza Mohd Nor

LIST OF PUBLICATIONS

(a) Journal Paper:

1) N. Izza M. Nor, K. Shah, J. Singh, Z. Sauli, "Film Bulk Acoustic Wave Resonator for Ku-band Applications", Applied Mechanics and Materials, ISSN: 1660-9336, web 1662-7482, Vol. 321-324, pp.1614-1619, 2013
2) N. Izza M. Nor, K. Shah, J. Singh, Z. Sauli, "Design and Simulation of Film Bulk Acoustic Wave Resonator in Ku-band", Advanced Material Research, ISSN: 1022-6680, web 1662-8985, Vol. 662, pp. 556-561, 2013
3) N. Izza M. Nor, K. Shah, J. Singh, Z. Sauli, "Design and Analysis of Ladder-Type Ku-Band Filter based on Film Bulk Acoustic Wave Resonator", Active and Passive Electronic Components, Vol. 2013, Article ID 403516, 2013

(b) Conference Paper:

1) N. Izza M. Nor, K. Shah, J. Singh, Z. Sauli, "Film Bulk Acoustic Wave Resonator (FBAR) Filters for Ku-band Transceiver", Nanotech 2013, Washington D.C, 12-16 May 2013
2) N. Izza M. Nor, K. Shah, J. Singh, Z. Sauli, "Film Bulk Acoustic Wave Resonator for Ku-band Applications", International Conference on Mechatronics and Industrial Informatics (ICMII), China, 13-14 March 2013
3) N. Izza M. Nor, K. Shah, J. Singh, Z. Sauli, "Design and Simulation of Film Bulk Acoustic Wave Resonator in Ku-band", International Conference on Nanotechnology and Precision Engineering (ICNPE), China, 26-27 December 2012

4) N. Izza M. Nor, K. Shah, J. Singh, N. Khalid, Z. Sauli, "Design and analysis of Film Bulk Acoustic Wave Resonator in Ku-Band Frequency for Wireless Communications ", Proceedings of SPIE Vol. 8341, 83411R, USA, 13-15 March, 2012
5) N. Khalid, K. Shah, J. Singh, N. Izza M. Nor, Z. Sauli, "Design and analysis of a 10 GHz VCO using MEMS inductor", Proceedings of SPIE Vol. 8341, 83411Q, USA, 13-15 March, 2012
6) N. Izza M. Nor, K. Shah, J. Singh, Z. Sauli, “High Quality Factor RF MEMS/NEMS Resonators for Very High Frequency Wireless Systems", Regional Conference of Solid-State and Semiconductor Technology (RCSSST), Malaysia, December, 2009

ACKNOWLEDGMENT

In the name of Allah, most Gracious, most Merciful. This doctoral thesis would not have been possible without the guidance and help of several individuals, who in one way or another, contributed and extended their valuable assistance in the preparation and completion of this study.

First and foremost, I would like to express my gratitude to my supervisors, Professor Jugdutt (Jack) Singh, for sharing his expertise and for his support and guidance; and Dr. Kriyang Shah, for his continuous support, guidance and understanding during my thesis research. This thesis would not have been completed without the endless encouragement and supervision from both of them. I also would like to thank my other co-supervisor from Universiti Malaysia Perlis (UniMAP), Associate Professor Zaliman Sauli, for his advice and support.

I would like to acknowledge my deepest gratitude to my beloved husband and companion, Ayob Nazmy for his never-ending support each and every day, for dissipating my doubts; and for the sacrifices during the tough and long PhD years here. To my baby boy, Muhammad Adam Izhan, I love you so much and my life has never been the same since you were born. Thank you so much to my mother, my father, brother, sisters and in-laws for your endless support even though we were apart. Without the encouragement and support from my family, the completion of this thesis would have been impossible.

I would like to acknowledge all my colleagues and the staff in the Centre for Technology Institution (CTI) for providing a comfortable and friendly work environment. A special thanks goes to Miss Tracey Carpenter and Dr. Felix Acker for their immense and willing commitment to proof read my thesis.

I especially thank the Ministry of Higher Education Malaysia (MOHE) and Universiti Malaysia Perlis (UniMAP) for the scholarship so that I could realise my dream to become an academician.

No answers, just more questions…That's research!

THESIS ABSTRACT

As the demand for wireless communication data and video grows, the demand for more channels and wider bandwidths is increasing. The conventional frequency bands (below 6 GHz) are already congested, thus to satisfy this demand, the research into transceiver systems working at frequencies higher than 10 GHz has been growing. Ku-band, ranging from 12 GHz to 18 GHz, is one of these frequency bands that is being considered. Cost, area and power consumption are the key figures of merit for such Ku-band transceiver systems.

A literature survey shows that most of these transceivers are large and heavy due to use of discrete components such as filters and separately located modules. The multi-layer low temperature co-fired ceramic (LTCC) and the systems-on-package (SOP) implementations are capable of overcoming these issues by integrating active and passive components on one board. Various Ku-band filters are reported in the literature using different designs and manufacturing methods, for example, defect ground structure (DGS), inter-digital structure, coupled line filters and couple strip line filters, which have been integrated using LTCC technology. However, improvements in filter performance and better integration methods with microwave monolithic integrated circuits (MMIC) radio frequency microelectromechanical system (RF MEMS) technology is needed to further improve integration and reduce cost and power consumption. A high quality (Q) factor narrowband film bulk acoustic wave resonator (FBAR) filter and FBAR diplexer designed using MEMS technology have been developed for WiFi and WiMAX applications. However, an analysis of Ku-band transceivers and filters shows that FBARs with a bandwidth of around 500 MHz will be required for the design of Ku-

band FBAR filters. This research focuses on the design, analysis and optimisation of a suitable FBAR for Ku-band filters to achieve this aim.

In this research, a ladder-type FBAR filter is designed and analysed using the one-dimensional (1-D) closed-form expressions based on FBAR design variables, including series resonance frequency, parallel resonance frequency, electromechanical coupling coefficient (k^2_{eff}) along with filter design variables such as filter order (N), insertion loss (I_L) and out-of-band (*OoB*) rejection. The effect of design parameters such as the series resonance frequency and parallel resonance frequency of the series FBAR (f_s^s and f_s^p), the series resonance frequency and parallel resonance frequency of the shunt FBAR (f_p^s and f_p^p) and the frequencies where the electrical impedance of the series FBAR and shunt FBAR are equal (f_1 and f_2) are analysed and discussed. The obtained electrical impedances from the analysis are employed to compute the S-parameters of the FBAR filter by using the *ABCD* matrix method. From the result, it is concluded that by increasing the order of the FBAR filter, the *OoB* rejection is improved; however, the insertion loss and the 3 dB bandwidth is degraded. The Ku-band FBAR filter characteristics obtained from the analysis are then used to extract the expected Ku-band FBAR characteristics by using the Butterworth Van Dyke (BVD) equivalent circuit.

In order to further analyse and optimise the Ku-band FBAR design parameters evaluated using the 1-D numerical analysis, the 3-D finite element method (FEM) is used. The influence of various geometrical parameters including the thickness, width and length of the piezoelectric film and electrode layers on the performance of FBAR is analysed to find suitable solutions for designing a wide bandwidth and high Q factor Ku -band FBAR. A higher k^2_{eff} will result in wider bandwidth while a higher Q factor will result in an FBAR with better performance. Analysis shows that the k^2_{eff} of the Ku-band FBAR can be

improved by optimising the thickness ratio of the electrode to the piezoelectric material (t_m/t_p). The optimum t_m/t_p is from 0.05 to 0.15 in order to achieve the maximum value of k^2_{eff} of the FBAR.

In 3-D FEM, material damping coefficients (α and β) of AlN are estimated using Akhieser approximation instead of using material properties of silicon to achieve a more realistic value of the Q factor. The values of α and β obtained are 1.55 x 10^4/s and 3.84e^{-14}s at 15 GHz, respectively. The optimised Ku-band FBARs have achieved k^2_{eff} of 6.47%, Q_s of 263.26 and Q_p of 284.29 for series FBARs, and k^2_{eff} of 6.51%, Q_s of 286.84 and Q_p of 306.51 for shunt FBARs resulting in an overall bandwidth of 430 MHz for series and 400 MHz for shunt FBARs**.** The Ku-band FBAR designed in this work has higher bandwidth, better k^2_{eff} and Q factor compared to other studies.

Finally, the Ku-band FBAR filters implemented with the optimised Ku-band FBARs are characterised by using the *ABCD* matrix method. The designed Ku-band FBAR filter has centre frequency of 15.5 GHz, insertion loss of -3.36 dB, out-of-band rejection of -11.90 dB, bandwidth of 1.09 GHz and area size of 0.58x0.15 mm^2. To the author's best knowledge, this is the first FBAR filter designed in Ku-band. This Ku-band FBAR filter has comparable performance to the best-known Ku-band couple stripline filter and achieves an area reduction of 99.5%. Therefore, the designed Ku-band FBAR filter is a suitable candidate to be implemented on the Ku-band transceiver.

CHAPTER 1 : INTRODUCTION

1.1 Introduction

As the wireless communication of data and video grows, the demand for more channels and wider bandwidths is increasing. The conventional frequency bands (below 6 GHz) are already congested, thus to satisfy this demand, the research into transceiver systems working at frequencies higher than 10 GHz has been growing. Ku-band, ranging from 12 GHz to 18 GHz, is one of these frequency bands that are being considered.

Cost, area and power consumption are the key characteristics to consider for such a transceiver system. However, the literature shows that most of these transceivers are relatively large and heavy due to the use of discrete components such as filters and other sub-modules located on the same or different printed circuit board (PCB). The multi-layer low temperature co-fired ceramic (LTCC) and the systems-on-package (SOP) implementations are capable of overcoming these issues by integrating active and passive components on one board. Various Ku-band filters are reported in the literature using different designs and manufacturing methods, for example, defect ground structure (DGS), inter-digital structure, coupled line filters and couple stripline filters, which have been integrated using LTCC technology. However, improvements in filter performance and better integration methods with microwave monolithic integrated circuits (MMIC) and radio frequency microelectromechanical system (RF MEMS) technology is needed to improve integration and reduce power consumption.

Film bulk acoustic wave resonator (FBAR) filters and FBAR diplexers designed using MEMS technology have been developed for WiFi and WiMAX applications. Such MEMS components have shown better performance and a higher integration level, and the same performance is expected to be achieved in Ku-band transceivers by using FBAR filters. FBARs operating in the frequency range of 5 GHz to 20 GHz have been reported to show a very high quality (*Q*) factor, good power handling and small size.

In this thesis, an FBAR operating in Ku-band is designed and researched by using an air-gap type FBAR and optimisation of its geometrical parameters and material losses. The Ku-band FBAR filters are implemented with the proposed FBAR using one-dimensional (1-D) numerical analysis. The FBAR filter size is reduced to desirable dimensions and showed acceptable performance compared to the other Ku-band filters reported in the literature.

1.2 Motivation

Typical Ku-band transceivers consist of a low-noise amplifier (LNA), power amplifier (PA), voltage-controlled oscillator (VCO), upconveter, downconverter and filters. The filter is one of the key components in transceivers. The current drawbacks of most commercially available microwave and millimetre-wave front-ends, such as the Ku-band satellite transceivers for outdoor units, are their relatively large size and heavy weight, the latter primarily due to discrete components such as the filters, and separately located modules [1].

FBAR filters have a very high *Q* factor, good power handling and small size [2-4]. Thus, low insertion loss with steep roll-off filters can be designed in Ku-band, which will improve system performance and allow higher integration, resulting in reduced cost and low power consumption. In addition, FBARs can be manufactured on a flat silicon substrate using surface micromachining and befits mass production. This allows the filter components to become compact and cheap [4]. Furthermore, FBARs are compatible with complementary metal-oxide-semiconductor (CMOS), MMIC and MEMS technology, resulting in better integration to reduce the size and cost of Ku-band transceivers.

1.3 Research Aims

The aim of this research is to design filter based on FBAR in Ku-band to meet the requirement of Ku-band transceiver specifications. This research focuses on investigating issues in the design of such an FBAR filter and develops solutions to the issues. The specific aims are:

- To study the application of Ku-band transceiver;
- To study and investigate the design issues for Ku-band filters;
- To research and design high *Q* factor and wide bandwidth FBARs for Ku-band filters;
- To study and investigate the design issues for FBAR filters in frequency more than 10 GHz;
- To analyse the performance of FBAR filters using the newly designed FBAR;

1.4 Original Contributions

The major contribution of this research is the design of a high *Q* factor FBAR in Ku-band using the air-gap FBAR. Aluminium nitride (AlN) and ruthenium (Ru) are used as the piezoelectric material and electrodes respectively. The influence of various geometrical parameters including the thickness, width and length of the piezoelectric film and electrode layers on the performance of FBARs is analysed to find suitable solutions for designing a wide bandwidth and high *Q* factor Ku -band FBAR. Analysis shows that the k^2_{eff} of the Ku-band FBAR can be improved by optimising the thickness ratio of electrodes to the piezoelectric material (t_m/t_p). The optimum t_m/t_p is from 0.05 to 0.15 in order to achieve the maximum value of k^2_{eff} of the FBAR.

The material damping coefficients (a and β) of AlN are estimated using Akhieser approximation instead of using material properties of silicon to achieve a more realistic value of the Q factor. The value of a and β obtained are $1.55e^4$/s and $3.84e^{-14}$ s at 15 GHz respectively. The optimised Ku-band FBARs have achieved k^2_{eff} of 6.47%, Q_s of 263.26 and Q_p of 284.29 for series FBARs, and k^2_{eff} of 6.51%, Q_s of 286.84 and Q_p of 306.51 for shunt FBARs resulting in an overall bandwidth of 430 MHz for the series and 400 MHz for the shunt FBARs.

Ku-band FBAR filters implemented with the optimised Ku-band FBARs are characterised by using the *ABCD* matrix method. The designed Ku-band FBAR filter has centre frequency of 15.5 GHz, insertion loss of -3.36 dB, out-of-band rejection of -11.90 dB, bandwidth of 1.09 GHz and area size of 0.58 x 0.15 mm^2 which makes it a suitable candidate for implementation in a Ku-band transceiver system.

1.5 Significance of the Research

The designed FBAR filter features a minimum size compared to other Ku-band filters with acceptable performance for Ku-band transceivers. Another advantage of the FBAR filter is that it can integrate with other CMOS technology. Furthermore, FBARs can be manufactured at a very competitive cost using standard integrated circuit (IC) manufacturing. This will remove interconnect and off-chip components. The designed FBAR filter also will reduce power and signal losses in on-board routes due to its high Q factor. Thus, it will improve the overall performance of Ku-band transceivers.

1.6 Research Methodologies and Techniques

The research methodologies and techniques to achieve the aims of this research are as follows:

- Study the application of Ku-band transceivers;

  A detailed literature review on Ku-band transceivers is carried out. Detailed analysis of Ku-band transceiver architectures is conducted to identify the key issues to achieve compact transceivers. The analysis shows that separately located modules and discrete components such as filters are the causes of large and heavy weight Ku-band transceivers.

- Study and investigate the design issues for Ku-band filters;

  Detailed analysis of various types Ku-band filters is discussed. Analysis shows that these filters have wide passbands (>1 GHz). However, these filters have slow roll-off due to their low *Q* factor resonators. Another disadvantage of the currently implemented Ku-band filters is their requirement for a large volume area. A better filter can be achieved by implementing a high *Q* factor resonator with minimum size. FBAR filters and FBAR diplexers have been developed for WiFi and WiMAX applications. These components have shown better performance with reduced size and cost, due to a very high quality *Q* factor, good power handling and small size. This also can be achieved in Ku-band transceivers by implementing the FBAR filters.

- Study and investigate the design issues for FBAR filters with a frequency greater than 10 GHz;

  The analysis of FBAR filter design issues is carried out to find proper solutions for designing a wide bandwidth FBAR filter in Ku-band. The resonance frequency of FBARs is determined by the thickness and phase velocity of the piezoelectric layer. Therefore, for FBARs operating in frequencies higher than 10 GHz, the thickness of the piezoelectric layer is in the hundred nanometre (nm) scale. AlN and Ru are chosen as the piezoelectric material and electrode due to their high acoustic velocity and high acoustic impedance respectively. The air-gap type FBAR operating in Ku-band is designed using CoventorWare ® 2010 and the optimisation of the geometrical parameters of the FBAR is fully analysed and discussed.

- Research and design a high Q factor and wide bandwidth FBAR for Ku-band;

  The air-gap type FBAR operating in Ku-band is proposed and designed to achieve maximum k^2_{eff} and high Q. The design and analysis of the FBAR are performed using simple fabrication steps that have been developed for the air-gap type FBAR. The ratio electrode to piezoelectric material is used to estimate the value of k^2_{eff}. A maximum k^2_{eff} with high Q FBAR is achieved by optimising the geometrical parameters. The k^2_{eff} is an important parameter used in designing an FBAR filter to improve the bandwidth of the filter.

- Analyse the performance of the FBAR filter using the newly designed FBAR;

  The performance of the Ku-band FBAR filters using the proposed FBAR is analysed and discussed in detail with respect to the bandwidth at 3 dB (BW_{-3dB}), insertion loss (I_L) and out-of-band (OoB) rejection.

1.7 Thesis Organisation

This thesis will highlight the design issues for transceivers operating in Ku-band. This is based on the detailed literature studies of Ku-band transceiver systems to date. Filters are identified as one of the limiting factors in achieving a compact transceiver. The Ku-band FBAR filter implemented with the proposed Ku-band FBAR results in comparable performance with other Ku-band filters. This thesis is organised as follows:

Chapter 2 presents a detailed discussion of the available literature on the applications of Ku-band in wireless communications systems. Various types of Ku-band transceivers are discussed. The major issue for Ku-band transceivers is their large size and heavy weight due to discrete components such as filters and other separately located modules. This chapter also explores the various types of Ku-band filters that have been implemented in Ku-band transceivers and points out the advantages and disadvantages of the current integration and implementation of these Ku-band filters. Improvement in filter performance and better integration methods with microwave monolithic integrated circuit (MMIC) and radio frequency microelectromechanical systems (RF MEMS) technology are reviewed. FBAR filters operating at lower frequencies, which are widely used in wireless communications applications, are also presented. Different types of FBARs and FBAR filters along with their associated design methodologies are also discussed.

Chapter 3 explains the theory of FBARs and FBAR filters. The detailed discussions on the theory of FBARs such as piezoelectric and acoustic propagation theory and their important characteristics, such as Q factor and electromechanical coupling coefficient (k^2_{eff}) are presented. Detailed discussion on the design methodology of FBARs and FBAR filters using 1-dimensional (1-D) and 3-dimensional (3-D) finite element methods (FEM) are explained. A detailed discussion on the major losses from piezoelectric material such as thermoelastic damping and material damping are also presented. This chapter also discusses the film bulk acoustic wave resonator (FBAR) filter, which focuses on the ladder-type FBAR filter. The theory and important characteristics of filters such as the insertion loss (I_L), out-of-band (*OoB*) rejection, and bandwidth (*BW*) are discussed.

Chapter 4 describes the design and analysis of Ku-band FBAR filters using 1-D numerical analysis. The effects of varying the design parameters such as f_s^s, f_s^p, f_p^s, f_p^p, f_1 and f_2 on filter characteristics are presented. The 'mid-band dip' issue in wide-bandwidth FBAR filter is also analysed. The effects of filter order (*N)* on out-of-band (*OoB)* rejection and filter characteristics are also discussed. Finally, the characteristics of the FBAR are described using the BVD model.

Chapter 5 focuses on the design and analysis of FBARs using the 3-D Finite Element Method (FEM). This includes the layout design, fabrication process and the FBAR model. The characteristics of the proposed FBAR are based on the characteristics of FBARs obtained using the BVD model in Chapter 4. The influence of various geometrical parameters and material losses on FBAR performance is analysed and discussed in detail to find suitable solutions for designing a wide bandwidth and high *Q* factor Ku-band FBAR. The estimation of material damping coefficients (a and β) using the Akhieser approximation is carried out to estimate more accurate values of the coefficients, thus a more realistic value of the *Q* factor will be achieved. CoventorWare ® 2010 is used as the simulation tool and MemMech Analyzer is chosen as the solver.

Chapter 6 presents the optimisation and analysis of the proposed Ku-band Film Bulk Acoustic Wave Resonator (FBAR). The results of the optimisation are summarised and compared with other FBARs from the survey. This chapter also presents the design of a Ku-band FBAR filter implemented with the optimised Ku-band FBAR. This Ku-band FBAR filter will be characterised with respect to bandwidth at -3 dB (BW_{-3dB}), insertion loss (I_L) and out-of-band (*OoB*) rejection. The performance of the designed Ku-band FBAR filter is compared to the Ku-band FBAR filter designed using the 1-D modelling in Chapter 4. Finally, the results from the analysis are presented along with comparisons from the literature survey.

Chapter 7 concludes the thesis and presents the major outcomes of this research. This chapter also discusses the limitations, assumptions and future work of this research.

CHAPTER 2 : LITERATURE REVIEW

2.1 Introduction

This chapter presents the literature review of Ku-band applications in wireless communications systems. Various types of Ku-band transceivers are discussed. The major issue of Ku-band transceivers is their large size and heavy due to discrete components such as filters and other separately located modules. This chapter also explores the various types of Ku-band filters that have been implemented in Ku-band transceivers and points out the advantages and disadvantages of the current integration and implementation of these Ku-band filters. Radio frequency (RF) components using microelectromechanical systems (MEMS) technology are reviewed. FBAR filters operating at lower frequencies, which are widely used in wireless communications applications, are reviewed. In addition, different types of FBARs and FBAR filters along with their associated design methodologies are discussed.

2.2 Mobile and Wireless Communication Bands

The demand for more channels and wider bandwidths is increasing as the volume of wireless communication of data and video grows. The conventional frequency bands (below 6 GHz) are already congested, thus driving research to microwave and millimetre-wave frequencies. To satisfy this demand, the development of microwave communication systems at frequencies higher than 10 GHz using satellite systems is important. One of the frequency bands that is of interest to researchers is Ku-band due to its wide frequency range. The microwave frequency bands according to IEEE Standard 521 [5] are shown in Table 2.1. According to the standard, Ku-band ranges from 12 GHz to 18 GHz.

Table 2.1 Microwave Frequency Band

Designation	Frequency	Wavelength
HF	3 - 30 MHz	100 m – 10 m
VHF	30 - 300 MHz	10 m – 1 m
UHF	300 - 1000 MHz	100 cm – 30 cm
L Band	1 - 2 GHz	30 cm – 15 cm
S Band	2 - 4 GHz	15 cm – 7.5 cm
C Band	4 - 8 GHz	7.5 cm – 3.75 cm
X Band	8 - 12 GHz	3.75 cm – 2.5 cm
Ku Band	12 - 18 GHz	2.5 cm – 1.67 cm
K Band	18 - 27 GHz	1.67 cm – 1.11 cm
Ka Band	27 - 40 GHz	1.11 cm – 0.75 cm
V Band	40 – 75 GHz	7.5 mm – 4.0 mm
W Band	75 – 110 GHz	4.0 mm - 2.7 mm
mm Band	110 – 300 GHz	2.7 mm – 1.0 mm

Transceiver systems working in a Ku-band frequency range of 12-18 GHz are primarily used for satellite communications and radars, including digital video broadcasting-satellites (DVB-S), very small aperture terminals (VSAT), snow-covering monitoring, weather forecasts, and airborne scatterometers [6-18]. The era of satellite communications began in the early 1960s after the first launch of communications satellites such as Telstar and Relay in 1962, Syncom in 1963, and INTELSAT 1 and MOLNIYA 1 in 1965 [9]. Since then, the applications of satellite communications are rapidly growing. Most of the satellite systems operating in C-band are already congested, and hence, the applications have been expanding to Ku-band and K-band due to their large available bandwidths [19]. The next section will discuss various transceiver architectures which operating in Ku-band.

2.3 Ku-band Transceiver Architectures

Ku-band transceiver architectures and transceiver specifications vary with with the various applications for which they are designed. An overview of Ku-band transceivers and their specifications is discussed in this section. Different types of transceiver architectures have been used in Ku-band including the superheterodyne architecture, up-conversion architecture, direct conversion architecture, low IF architecture, band-pass sampling radio architecture and software-defined radio architecture.

A typical Ku-band transceiver consists of a low-noise amplifier (LNA), power amplifier (PA), voltage-controlled oscillator (VCO), local oscillator (LO), upconveter, downconverter, intermediate frequency (IF), low pass filters (LPF), bandpass filters (BPF), mixer and diplexer as presented in Figure 2.1. This typical transceiver is widely employed in the outdoor unit (ODU) for VSAT and other Ku-band applications. The specifications of the ODU are summarised in Table 2.2.

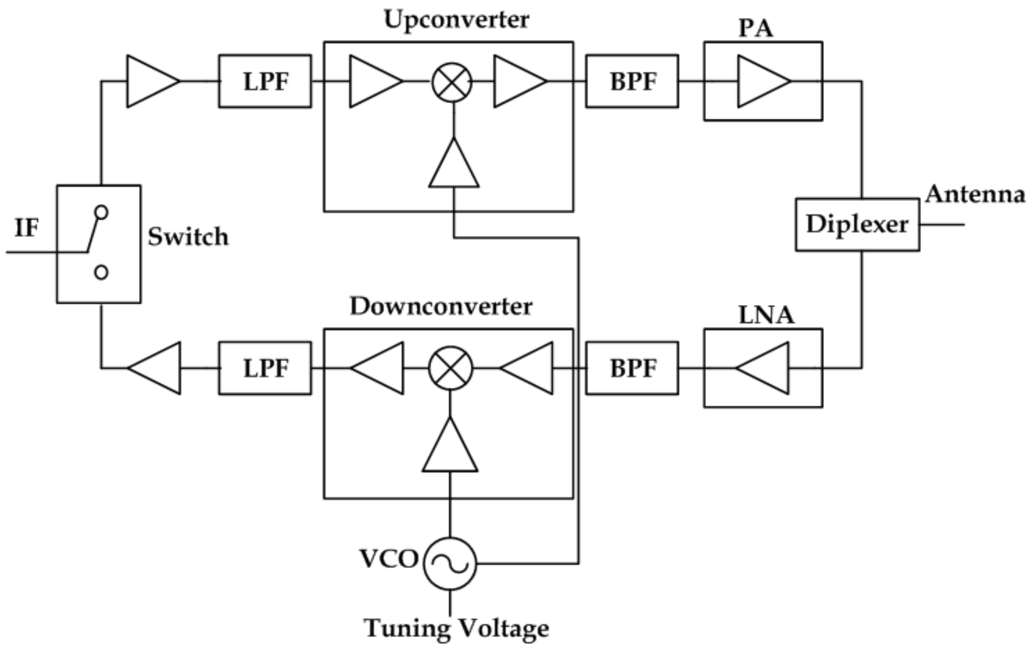

Figure 2.1 Typical Ku-band Transceiver Architecture [9]

In this architecture, the transmitter performs the modulation, up-conversion and power amplification. From the reference in [9], it is clearly shown that the transceiver has separately located modules and the VCO and filters are off-chip which contributes to the large size of the transceiver. Hence, components with better integration are needed to overcome this drawback.

Table 2.2 The Front-End Ku-band ODU Specification [6, 20]

	Frequency Band (GHz)	Input Power (dBm)	Output Power (Watt)	Gain (dB)	Noise Figure (dB)	1 dB compression	Spurious Output
Receiver	10.95-11.7 11.7-12.2 12.25-12.75	0 (min)	0.5-5	45-55	2.7 (max)	-15 dBm (min)	-
Transmitter	14.0-14.5	-15 +5 (IF)	1 W (-1, +2 dB)	-	-		-45 dBc (max)
IF	0.9-1.4						

Figure 2.2 shows the Ku-band retrodirective radar transceiver that is employed in military operations for the detection and tracking of sniper rifle bullets and other ballistic projectiles that work at 12.2 GHz. This transceiver has implemented the standard heterodyne RF front-end architecture.

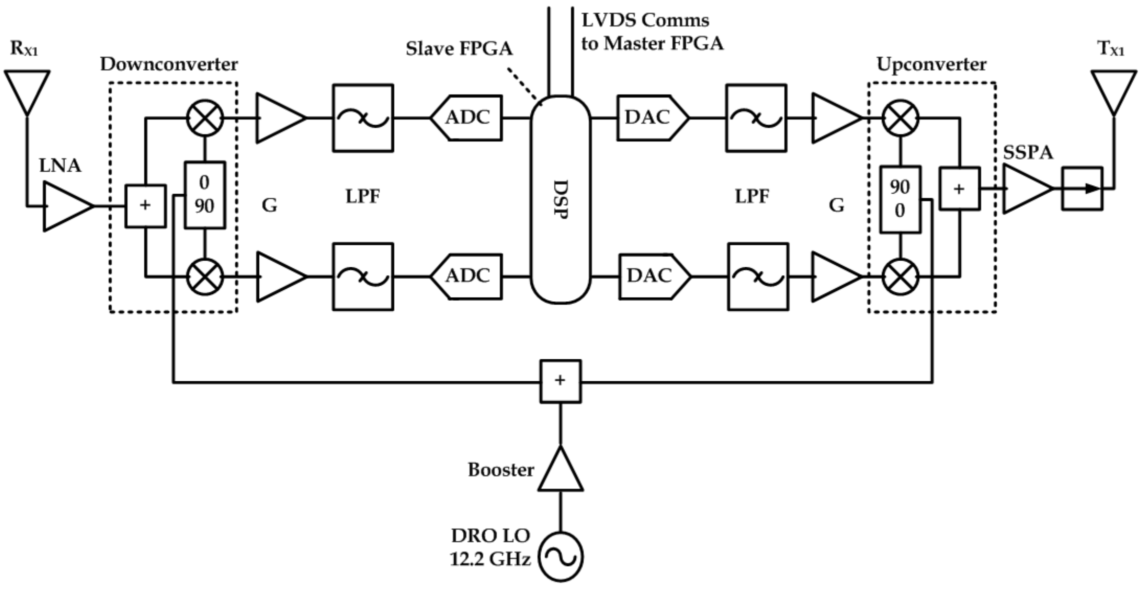

Figure 2.2 Ku-band Radar Transceiver [10]

The system carries out the entire signal processing digitally by using the field-programmable gate array (FPGA) due to the requirement of the fast preserving correlations and the need for flexibility with the pseudorandom noise (PRN) sequence and its length. This transceiver has a NF of ~2.0 dB and a gain of 60 dB. In this study [10], this transceiver has separately located modules and the VCO and filters are off-chip. Again, this results in a transceiver with a large size. Therefore, the replacement of the components with better integration is needed to overcome the disadvantage.

Figure 2.3 shows the front-end of the transceiver that works in Ku-band. This transceiver is implemented the superheterodyne architecture. The specifications of this transceiver are summarised in Table 2.3. In the research, the multi-layer low temperature co-fired ceramic (LTCC) technology was applied to overcome the large size issue. Yet, components with better integration are still needed such as an RF MEMS component that is compatible with other standard IC technology.

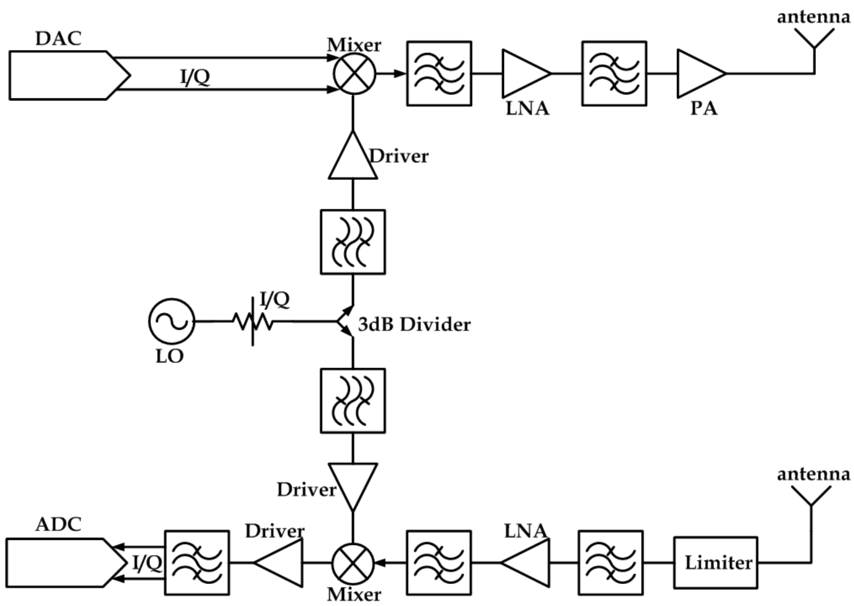

Figure 2.3 Front-End of Ku-band Transceiver [21]

Table 2.3 Specifications of Ku-band Transceiver Front-End [21]

	Input Frequency (GHz)	Output Frequency (GHz)	Input Power (dBm)	Output Power (dBm)	Gain (dB)	NF (dB)	Rejection (dBc)
Receiver	15.5±0.5	0.8±0.5	≤ -10	-	≥ 25	≤ 5.5	-
Transmitter	0.8±0.5	15.5±0.5	0	≥27	≥ 27	-	≥ 35
IF	LO frequency: 14.7 GHz Output power: 19 dBm						

Cost, area and power consumption are the key performance factors in such transceiver systems. The system-on-chip (SOC) is one of the alternatives to achieve a smaller transceiver. In this method, all the blocks of a transceiver are integrated on a chip. The drawbacks of this method are the long design time due to integration complexities, high wafer fabrication costs, test costs, and mixed-signal processing complexities requiring dozens of mask steps to provide digital, RF, optical, and MEMS-based components and intellectual property issues [22]. The system-in-package (SIP) approach is one integration technology that simplifies the implementation of RF components into modules using hybrid integration where the individual ICs are first packaged and then stacked to form a 3-D circuit [22-23]. Both SOC and SIP provide major opportunities in both miniaturisation and integration; however, they are limited by the CMOS process. The study in [24] successfully presented the integration of FBAR bandpass filters with LNA and mixers by using SIP for a WCDMA receiver.

Another method of integration is the systems-on-package (SOP) method. SOP technology is CMOS compatible as it uses CMOS-based silicon, which is good for transistor integration and digital integration by means of an IC-package-system co-design. By using this method, the passive and active components can be integrated on a chip as shown in Figure 2.4. The multi-layer LTCC technology is a suitable substrate to be used for SOP to achieve a small transceiver [25]. The LTCC has the advantage of high quality, low loss and high dielectric constant. Therefore, the implementation of LTCC and SOP are capable of overcoming the issues of cost, area and power consumption by integrating all components on one board. The literature shows that most of these transceivers are relatively large and heavy due to use of discrete components such as filters [1, 21, 26]. In the next section, the filters in Ku-band transceiver systems will be discussed.

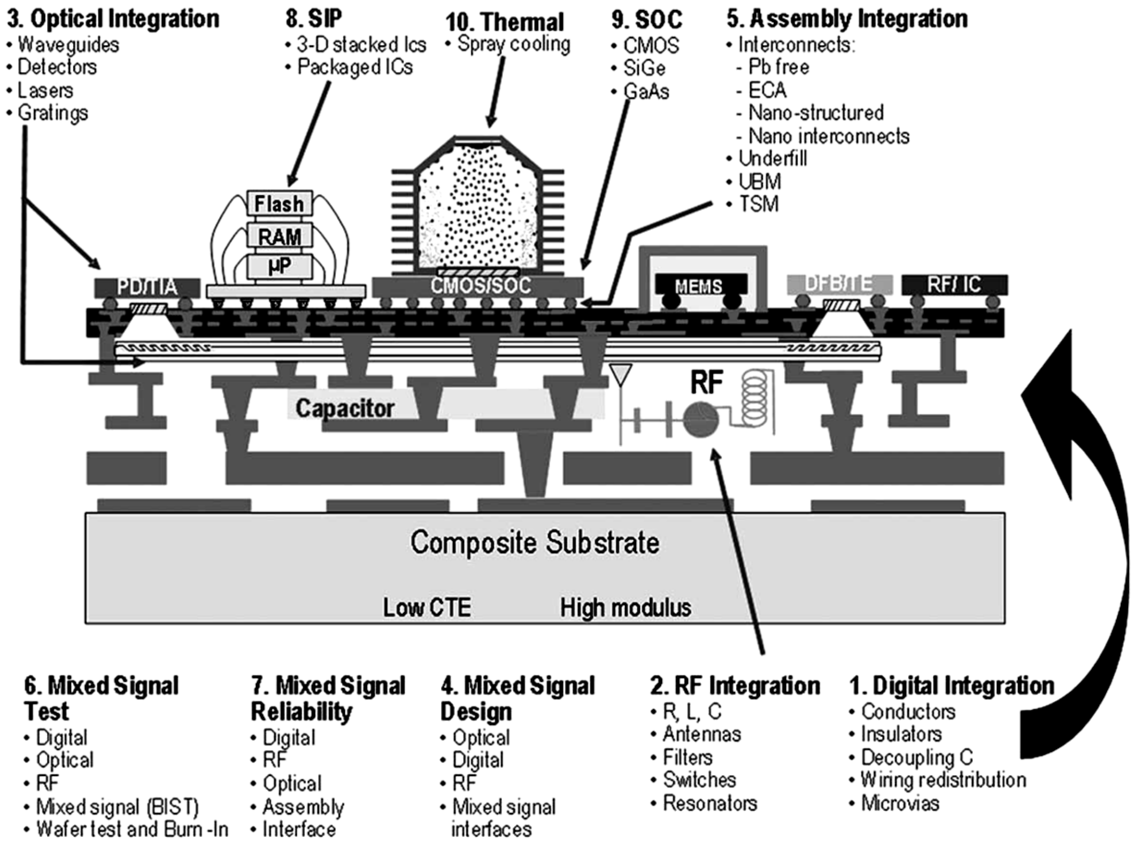

Figure 2.4 SOP Concept for System Integration of Thin film Components [22]

2.4 Filters in Ku-band Transceiver Systems

Filters play an important role in Ku-band transceiver applications. Various Ku-band filters are reported in the literature using different designs and manufacturing methods such as defected ground structure (DGS), inter-digital structure, coupled line filters, coupled stripline filters, coplanar waveguide

(CPW) and others, as in [12, 21, 27-31]. This section reviews the advantages and the drawbacks each of these filters.

The Ku-band tunable filter utilising a cavity resonator in [27] has shown excellent performance with insertion loss as low as -0.1 dB and return loss of -15 dB. However, the drawbacks of this filter are its large area size of up to 0.75x0.05 inch and complex manufacturing process thus miniaturisation is impossible and its manufacturing cost is high. A switched filter bank in [28] was designed by using two single-pole triple throw (SP3T) MEMS switches and three fixed three-pole end-coupled bandpass filters. The filters have centre frequencies of 14.9 GHz, 16.2 GHz and 17.8 GHz with fractional bandwidths of 7.7 ± 2.9%. These filters were fabricated in a microstrip with 2 μm gold line on a 250 μm alumina substrate to reduce the insertion loss that results in high manufacturing cost. The overall size of the switched filter bank is 15.4x6.7 mm^2. The size of this filter can be reduced if the fixed end-coupled bandpass filters are replaced with a filter that fabricates the use of MEMS technology. The study in [29] presented the seven-pole filter based on dielectric resonators operating at a centre frequency of 13 GHz. Even though it has an excellent return loss (-80 dB) and insertion loss of -2.0 dB, the size of this filter is 65x38 mm^2, which is relatively large. In [30], a bulk micromachined tunable dual-mode bandpass filter employing CPW and coplanar stripline (CPS) square-ring resonators was developed. This filter has shown a good insertion loss (-0.5 dB) and return loss (-15 dB) with size of 2x2 mm^2 and MEMS technology compatibility. However, the bandwidth is less than 1 GHz, which is not wide enough for Ku-band transceivers such as the one designed in [21].

The bandpass filter designed in [12] was implemented in a coupled stripline filter topology on a multi-layer LTCC substrate to suppress the LO signal at 13 GHz and image signal at 12 GHz as well as to suppress the harmonics and spurious signals. This filter has a size of 5.5x3.8 mm^2 including the CPW pads which is considered compact, according to the study. However, it is believed that if the filter is replaced by a MEMS filter, a smaller filter can be achieved. Research in [21] developed the DGS and interdigital filters on a multi-layer LTCC substrate. Two types of Ku-band filters were used which have centre frequency of 15.5 GHz and 14.7 GHz. The filter operates at the centre frequency of 15.5 GHz is used to select the frequency band implemented with the interdigital filter. The insertion loss reported is -1.5 dB from 14.9 GHz to 16.1 GHz, return loss of -15 dB in the passband and a bandwidth of 1.2 GHz. The filter operating at the centre frequency of 14.7 GHz is used for filtering the LO signal implemented with the DGS structure. The insertion loss reported is -2.0 dB and return loss of -20 dB from 14.9 GHz to 16.1 GHz. Even though these filters have shown reasonably good characteristics, a filter with a better integration method is needed to improve the integration so that it is compatible with standard IC manufacturing. The study in [31] showed the differential Ku-band filter working at 12 GHz. This filter was smaller in size compared to the other filters explained previously. However, a filter with better integration method is needed to improve the integration and reduce the manufacturing cost.

Table 2.4 shows a summary of the filters discussed along with their performance for comparison. These filters have been integrated using the LTCC technology and have shown reasonably good performance in terms of insertion loss, return loss and bandwidth. However, improvement in filter performance and better integration methods with microwave monolithic integrated circuits (MMIC) and standard complementary metal oxide semiconductor (CMOS) technology is needed. Furthermore, these filters are still large. Therefore, alternative technology such as radio frequency (RF) microelectromechanical systems (MEMS) technology is needed to improve integration and reduce power consumption and size. There are different types of RF MEMS components, which will be discussed in the next section.

Table 2.4 Various Types of Ku-band Filters

References	**Type of filter**	**Frequency (GHz)**	**Insertion Loss (dB)**	**Return Loss (dB)**	**Bandwidth (GHz)**	**Size (mm^2)**
[27]	Cavity	11.95 (f_c)	-0.10	-15.0	0.52	--
[31]	Differential	12.0 (f_c)	-4.0	-20.0	1.2	1.8x1.1
[29]	Dielectric	13.0 (f_c)	-2.0	-80.0	0.19	65x38
[12]	Coupled stripline	14.527 (f_c)	-3.27	-29.61	1.1	5.5x3.8
		14.329 (f_c)	-3.06	-27.82	1.1	5.5x3.8
		14.229 (f_c)	-3.14	-21.91	1.1	5.5x3.8
		14.130 (f_c)	-3.12	-18.97	1.1	5.5x3.8
		14.225 (f_c)	-3.01	-20.34	1.0	5.5x3.8
[28]	Fixed end-coupled	14.9 (f_c)	-1.0	-15.0	1.15	15.4x6.7
		16.2 (f_c)	-1.1	-15.0	1.25	
		17.8 (f_c)	-1.5	-20.0	1.37	
[21]	Interdigital	15.5 (f_c)	-1.5	-15.0	1.2	--
[30]	CPW	17.0 (f_c)	-0.5	-15.0	0.68	2.0x2.0

2.5 RF MEMS Components

Microelectromechanical systems (MEMS) is technology that can be defined as miniaturised mechanical and electro-mechanical elements such as devices and structures that are made using the techniques of microfabrication. The dimensions of MEMS components are in a range from hundreds of nanometres to hundreds of micrometres. The first MEMS device was the gold resonating metal-oxide-semiconductor (MOS) transistor invented by H.C Natahanson in 1967. Since then, MEMS have grown to incorporate the pressure microsensor in the 1970s; followed by the actuator, microlenses and accelerometers in the 1980s. RF devices, chemical sensors, micromirrors, antennas and gears were developed during the 1990s. Later in the following decade, the medical applications, the lab-on-chip (LoC), micro total analysis systems (μTAS), bio-MEMS and NEMS devices developed [32].

MEMS components have been implemented in RF and microwave applications because RF MEMS technology has been proven to be one of the most valuable technologies for low loss, low power consumption, higher linearity and higher *Q* factor [33]. The RF MEMS technology has the advantages of compatibility with CMOS technology and high voltage devices for a fully integrated system-on-chip (SOC) [34]. There are various types of RF MEMS components such as microswitches, tunable capacitors, micromachined inductors, micromachined antennas, microtransmission lines, micromachined resonators including micromechanical resonators, bulk acoustic wave (BAW) resonator and cavity resonators [35-36]. In this recent study, the focus is only on resonators, which is an important component that comprises the RF MEMS filter. RF MEMS filters and resonators are widely employed in mobile phones, consumer electronic and information technology (IT), and in WLAN and WPAN, while, cavity resonators are implemented in satellite communications. It is expected that the applications of BAW resonators will be extended to base stations, satellites and military radio, which operate at frequencies higher than 10 GHz [36].

The transduction methods in resonators are generally based on the electrothermal, magnetic, electrostatic and piezoelectric transductions. The most common transduction techniques used are piezoelectric and electrostatic due to their performance, manufacturability and power consumption. The clamped-clamped beam resonator, free-free beam resonator, wine-glass disk resonator, contour-mode disk resonator and hollow-disk ring resonator use the electrostatic transduction method. These resonators have shown very high *Q* factor ranges from 2000 to 156000 [37-39]. The drawback is the operating frequency is limited to around 1.2 GHz. Resonators using the piezoelectric transduction have shown better performance in terms of operating frequency. Surface acoustic wave (SAW) and BAW resonators are the most common resonator utilising the piezoelectric transduction. A previous study in [40] showed that the novel AlN piezoelectric NEMS resonator works from 5.2 GHz to 9.9 GHz and has a *Q* factor of 202 to 700. In the study, the resonance frequencies were obtained by piezoelectric excitation of nano-strips (500-1000 nm wide) of AlN in their contour-extensional mode of vibration. NEMS devices are not scaled-down MEMS devices, but a quite different technology approach, where new fabrication tools which using. New materials and structures are also being investigated and implemented in NEMS devices such as carbon nanotubes, nanowires and organic composites [41-44]. SAW and BAW resonators operating at frequencies from 1 GHz to 3 GHz were reported in [45-50]. Later in [51], BAW resonators working in 5 GHz to 20 GHz with a *Q* factor from 208 to 900 based on AlN were reported. The next section will discuss the types of acoustic resonators along with the advantages and drawbacks in detail.

2.6 Acoustic Wave Resonator

Acoustic microresonators are enabling the reduction in size and power consumption of mobile radio equipment and sensing systems [32]. These devices experience acoustic wave propagation and vibrate at resonance frequencies related to their dimension and mechanical configuration, when driven under the appropriate conditions. There are two types of acoustic devices, which are surface acoustic wave (SAW) and bulk acoustic wave (BAW). In SAW, the acoustic wave propagates parallel to the piezoelectric slab in the interdigital transducer (IDT) along the surface of the resonator [46, 52]. The drawbacks of SAW resonators are that the achievable operating frequency is limited to around 3 GHz due to the separation of each finger in the IDT. A second drawback is that SAW resonators are usually manufactured on a $LiTaO_3$ or $LiNbO_3$, which is not compatible with standard integrated circuit (IC) processes [53-54]. The comparison of the main characteristics of SAW and BAW resonators is presented in Table 2.5. Given the advantages of the BAW resonator, this work will focus on this type of resonator.

Table 2.5 Comparison of SAW and BAW Technology

Characteristics	SAW	BAW
Frequency range	up to 3 GHz	up to 30 GHz
Power handling	~31 dBm	~36 dBm
Temperature Coefficient of Frequency	-45 ppm/°C	-20 ppm/°C
Quality (*Q*) factor	~700 at 2 GHz	~2000 at 2 GHz
Compatibility with IC process	No	Yes

2.6.1 Types of BAW

The BAW resonator is the core element of BAW technology. The BAW resonators are categorised according to the mechanism that confines the acoustic wave in the resonator structure. There are two different types of BAW resonators: film bulk acoustic wave resonators (FBAR) and solidly mounted resonators (SMR). The operation and physical principles of both resonators are identical. The only difference is the fabrication technology used to confine the acoustic wave as shown in Figure 2.5. In FBAR, the confining is done by the air-gap cavity while for SMR, it is achieved through a Bragg reflector [55-56]. In this study, only FBAR will be discussed.

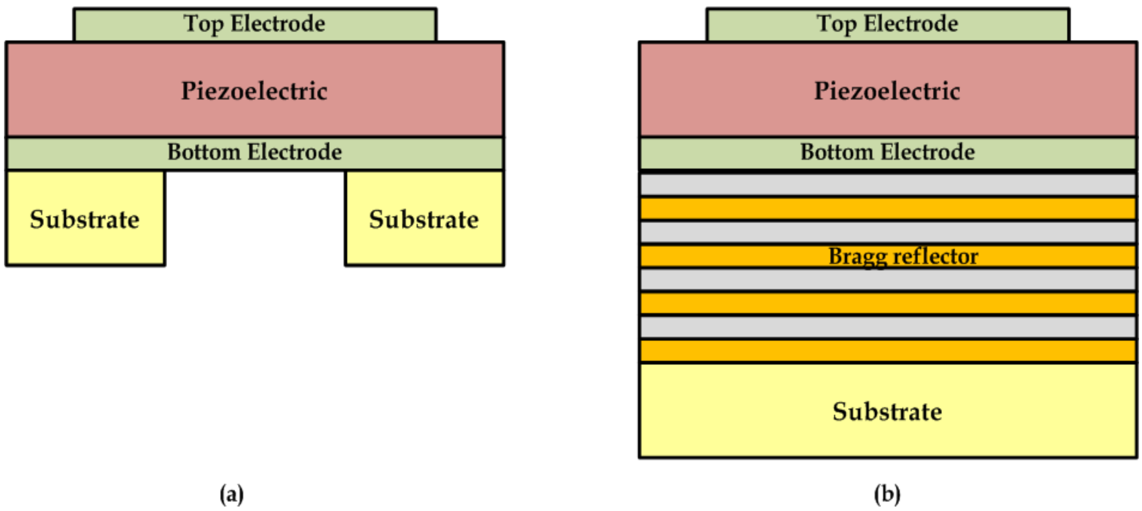

Figure 2.5 Layer Configurations for FBAR (a) and SMR (b)

In FBAR, the air/crystal interface on both faces of the resonator ensures the main mode of interest is appropriately trapped [57]. The resonators are surrounded by air by means of micromachining techniques. The most common techniques employed to form the air-gap of FBARs are shown in Figure 2.6. In the first technique, as shown in Figure 2.6 (a), the cavity is formed and filled with a thick sacrificial layer. Then the substrate is polished to obtain a smooth surface by using chemical mechanical polishing technology. Next, the bottom electrode, piezoelectric film and the top electrode are each stacked and patterned. Finally, the cavity is formed by etching the sacrificial layer.

The second technique is the vertical via-hole type as shown in Figure 2.6 (b). Using this technique, the FBAR is fabricated without any sacrificial layer. A vertical via-hole is fabricated by etching a silicon substrate from the backside using deep-reactive ion etching (RIE) technology [58]. In this structure, the whole resonator is suspended by itself in the air, achieving a *Q* factor of between three and five times that achieved when using a sacrificial layer [59].

The third technique is called the bridge type as shown in Figure 2.6 (c). Using this technique, the FBAR is formed on a flat substrate and does not need a cavity. A thick sacrificial layer is used to ensure that there is distance between the bottom electrode and the substrate. The drawback of this technique is the etching time. For a small device, the risk of damage is higher due to excessive etching time. The silicon dioxide (SiO_2) layer is used to cover the sacrificial layer during wafer processing and as a support layer of the laminated structure. In this recent study, the cavity type is chosen as the technique to fabricate the FBAR.

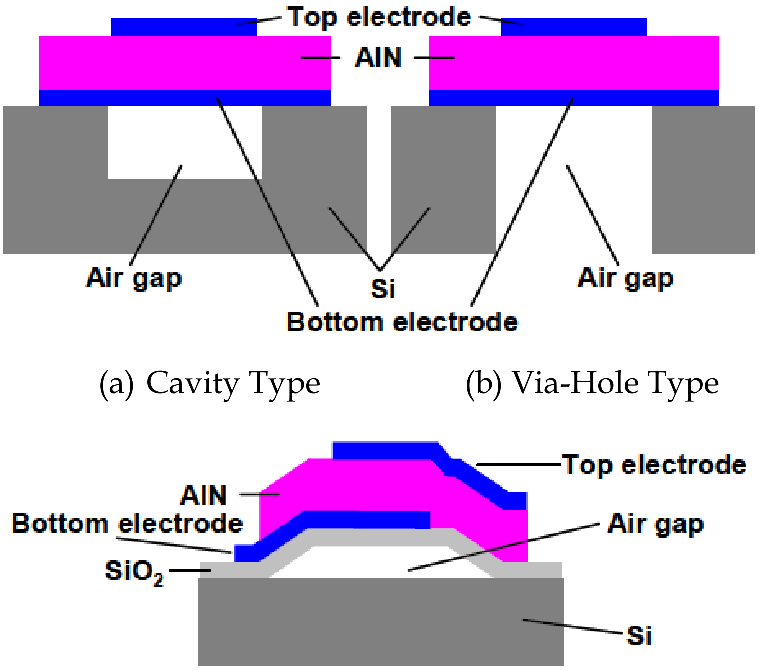

(a) Cavity Type (b) Via-Hole Type

(c) Bridge Type

Figure 2.6 Conventional FBAR Structures [55]

2.6.2 Piezoelectric Materials

The most common piezoelectric materials used for development of BAW are aluminium nitride (AlN) and zinc oxide (ZnO) [60-63]. FBARs based on lead zirconate titanate (PZT) and cadmium sulphide (CdS) [64-65] are also found in the literature. CdS has low acoustic impedance and an electromechanical coupling coefficient (~2.4%). PZT has good performance in terms of the electromechanical coupling coefficient (k^2_{eff}) values of 19.8%, but has high intrinsic losses at high frequencies [63]. Thus, PZT is mostly used for low-frequency BAW devices or applications that do not require a high *Q* factor [15]. For higher frequency applications, ZnO and AlN are the most suitable piezoelectric materials. The physical properties of these materials are shown in Table 2.6. These materials have the same hexagonal wurtzite structure. Although the coupling coefficient of ZnO is higher than AlN, AlN is superior to ZnO due to its moderate mechanical coupling factor, higher acoustic velocity and higher Q value. This makes AlN suitable to fabricate bulk acoustic wave (BAW) resonators/filters in several gigahertzes (GHz). Furthermore, AlN is compatible with CMOS technology and more easily manufactured compared to ZnO [15, 66].

Table 2.6 Physical Properties of Piezoelectric Materials [15, 67]

Properties	**AlN**	**ZnO**
Piezoelectric coupling coefficient, k^2_{eff} (%)	6.5	8.5
Dielectric constant, ε_r	9.5	9.2
Acoustic velocity, ν_L (m/s)	11050	6350
Piezoelectric coefficient, d_{33} (10^{-12}C/N)	5.6	12.4
Young Modulus (10^{11}N/m^2)	3.94	2.11
Thermal conductance (W/mK)	280	60
Thermal expansion (10^{-6}/K)	4.15	2.92
Density, ρ (kg/m^3)	3260	5680
Intrinsic material losses	Very low	Low
CMOS compatibility	Yes	No
Deposition rate	High	Medium

2.6.3 Electrode

Most FBAR applications require metal electrodes that have high acoustic stiffness, high acoustic impedance, low electrical resistance, compatibility with standard manufacturing techniques and a suitable surface to align the piezoelectric layer [15]. Conventionally, aluminium (Al), platinum (Pt), tungsten (W) and Titanium (Ti) are used as electrode materials [49, 68-69]. All have good electrical conductivity but poor acoustic characteristics because its acoustic impedance is low, which implies a low electromechanical coupling coefficient and thus limits the attainable bandwidth [15]. The disadvantage of using Pt and W in a high frequency FBAR filter is due to their high-mass density which lowers the series frequency value because of the mass loading effect [49]. Other material has been investigated such as gold (Au) [48-49] that has shown a good performance, however, this results in higher costs.

To overcome the issues of high cost and poor performance, molybdenum (Mo) and ruthenium (Ru) have recently been used due to their low resistivity, high acoustic impedance and low density [70-72]. Ru has a higher acoustic impedance of 86.3 MPa/m^2s than Mo, which has an acoustic impedance of 68.5 MPa/m^2s. This makes Ru the most suitable electrode material for FBARs in frequencies higher than 10 GHz.

2.6.4 FBARs in Different Frequency Ranges

FBARs operating at frequencies 1 GHz to 3 GHz have been widely employed in mobile phone transceiver systems [61, 70, 73-76]. FBARs working at 5 GHz also have been implemented in WLAN systems [58, 62, 77-78]. Further studies in [79-81] have shown FBARs operating at frequencies ranging from 10 GHz to 20 GHz. The FBARs in [58, 78] have similar resonance frequencies which are 5.17 GHz and 5.21 GHz. In both studies, AlN was employed as the piezoelectric material, however in [58], aluminium was used as the electrodes while in [78], Ru/Ta was used as the top electrode and molybdenum as the bottom electrode. k^2_{eff} of 7.0% achieved in [78] is higher than k^2_{eff} achieved in [58], which is 6.4%. It is also shown that the bandwidth of the study in [58] is lower than the bandwidth in [78], which are 0.14 GHz and 0.26 GHz, respectively. However, the Q factor obtained in [58] is around three times higher than in [78], which are 913 and 329, respectively. The relationship between k^2_{eff} and the Q factor has been presented in detail in [49, 82] that shows that improving one of these parameters can cause the decrease of the other. Therefore, the optimisation of both parameters by one figure of merit (FOM) is needed. The k^2_{eff} and Q factor of FBAR resonators determines the bandwidth and the efficiency of energy conversion from electrical to mechanical energy in an FBAR filter, respectively [49, 83]. It is also mentioned in [49] that a lower value of k^2_{eff} leads to a high insertion loss and a higher value of Q leads to lower insertion loss in filter applications.

k^2_{eff} has been shown to have achieved ranges from 6.0% to 6.4% at X-band to K-band using AlN and Ru [4, 72, 79, 81]. High k^2_{eff} can be achieved with the right choice of materials for piezoelectric and electrode layers. From Figure 2.7 (a), it is shown that there are various combinations of piezoelectric and electrode thicknesses to achieve the required resonance frequency. Figure 2.7 (b) shows the technique to enhance the k^2_{eff} of the FBARs using different electrode materials [79]. It is shown that a higher k^2_{eff} can be achieved when the thickness ratio of electrode to piezoelectric material is optimal.

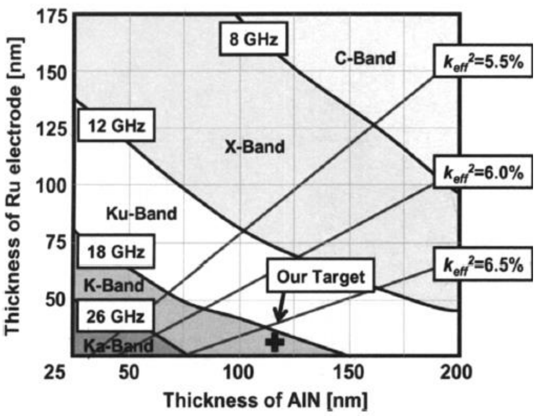

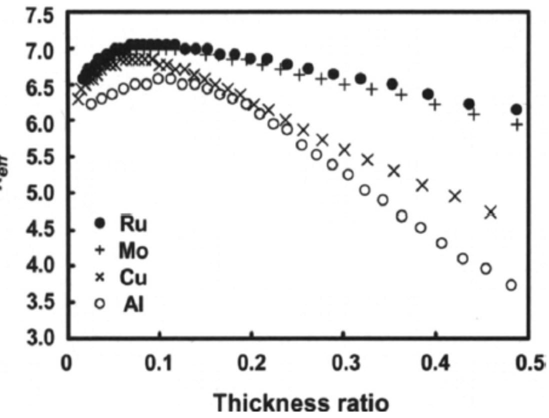

(a) (b)

Figure 2.7 Relationship Between the Frequency Bands, Piezoelectric Film Thickness, Electrode Thickness and k^2_{eff} of FBARs [79]

The literature also shows that the piezoelectric layer is thicker at lower frequency. Therefore, the *Q* factor is higher at lower frequency due to low acoustic loss. A high *Q* factor FBAR at frequencies higher than 10 GHz can be realised with the right choice of piezoelectric material as well as the electrode materials. Piezoelectric material with high acoustic velocity such as AlN and electrode material with high acoustic impedance such as Mo and Ru are excellent materials that can improve the characteristics of the FBAR.

There are few studies on different geometrical parameters and shape of the electrodes [64, 84-85] to improve the performance of the FBAR. In [53], piezoelectric material and electrodes with an ellipse shape were used to minimise stress to avoid cracking during fabrication due to the very thin (in hundreds nm) thickness of the layers. The study in [74] developed an FBAR with different top electrode shapes, square and circular. The circular shape electrode showed a higher k^2_{eff} and Q factor compared to an FBAR with a square shape. The study suggested that this was due to less energy loss in the edge of the top electrode with the circular shape. The relationship between both k^2_{eff} and the Q factor with the geometrical parameter of the FBAR was discussed in [75]. It shows that the ratio of the surface and perimeter (A/p) of the FBAR has a significant effect on these parameters. An FBAR with low A/p resulted in reduced k^2_{eff} and Q factor. The FBARs discussed are summarised in Table 2.7 along with their performance for comparison.

Table 2.7 Comparison of FBARs

Reference	**PZE**	**f_s (GHz)**	**f_p(GHz)**	**k^2_{eff} (%)**	**BW (GHz)**	**Q**
[79]	AlN	19.8	19.998	6.25	0.198	189
[81]	AlN	9.025	9.3	6.40	0.225	247
[80]	AlN	5.08	5.24	6.20	0.16	900
	AlN	9.30	9.60	6.30	0.30	330
	AlN	13.75	14.25	6.00	0.50	300
[78]	AlN	5.21	5.47	7.00	0.26	329
[58]	AlN	5.17	5.31	6.40	0.14	913
[62]	ZnO	5.10	5.25	4.70	0.15	700
	ZnO	4.80	4.95	6.70	0.15	1000
[70]	AlN	3.69	3.71	1.06	0.02	1557
[76]	ZnO	2.36	2.38	1.55	0.02	65
[61]	AlN	2.18	2.19	1.50	0.01	332
[74]	AlN	1.85	1.91	6.59	0.06	1911
[73]	ZnO	1.06	1.09	6.90	0.03	386
		1.10	1.13	7.84	0.03	159

The reviews suggest that FBARs based on AlN show better performance at frequencies higher than 5 GHz due to their higher acoustic velocity compared to ZnO. Another advantage of FBAR technology using AlN is its CMOS compatibility and its better temperature coefficient of frequency (TCF). FBARs based on AlN have gained wide-ranging popularity in filters but it can also be employed in other applications such as sensors [86-87], oscillators [88-89] and diplexers [90-91]. However, the FBARs designed are not in a suitable band, and have less k^2_{eff}, narrow bandwidth and a low Q factor. Hence, there is a need for this research in novel FBAR design that operates in 15 GHz to 16 GHz range with wide bandwidth, high k^2_{eff} and a suitable Q factor with the least size for a high level of integration in filter designs.

2.7 Filters based on FBAR

FBAR filters can be classified according to the main coupling categories [92]: electrically connected resonators, such as ladder and lattice topologies (see Figure 2.8 (a) and Figure 2.8 (b)) and acoustically connected resonators, such as the stacked crystal filter (SCF) and coupled resonator filter (CRF) as shown in Figure 2.9 (a) and Figure 2.9 (b). The overview of the characteristics of these filters will be discussed, along with their advantages and disadvantages.

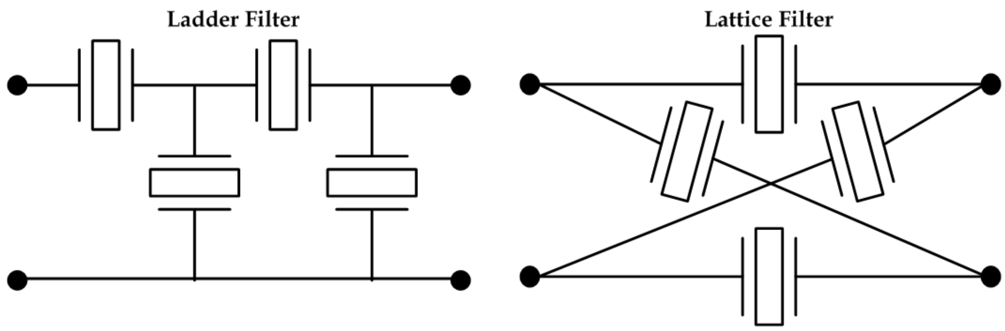

(a) (b)

Figure 2.8 Electrically Coupled FBAR Filter Configurations [93]

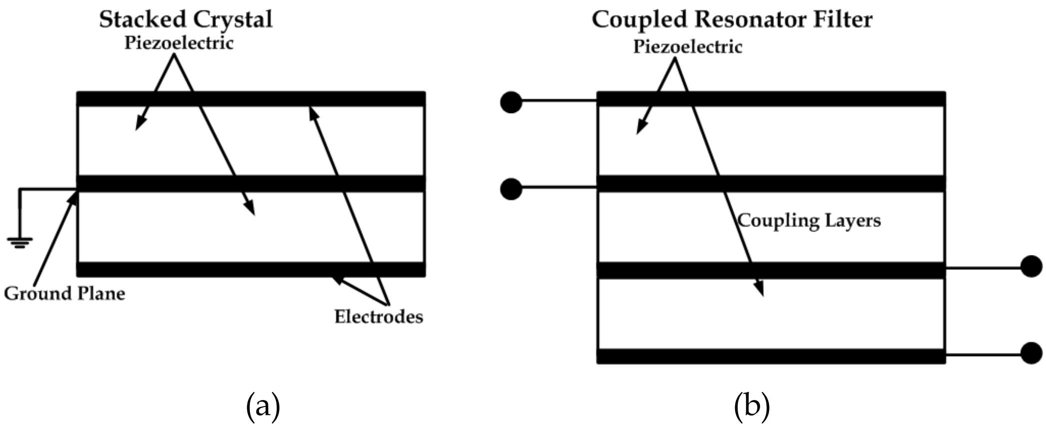

Figure 2.9 Acoustically Coupled FBAR Filter Configurations [93]

2.7.1 Ladder Filters

The ladder-type filter topology comprises series and shunt FBARs connected consecutively as shown in Figure 2.8 (a) [93]. This type of filter gives a steep roll-off and its high selectivity consumes fewer FBARs. The drawback, on the other hand, is that this filter has poor out-of-band (*OoB*) rejection due to the natural capacitor voltage divider [59]. Improvement of the *OoB* rejection requires increasing the order of the filter [28, 94], however, this requires a trade-off with respect to the in-band insertion loss (I_L) [95]. In [66], the achievable relative bandwidth is given as BW(%) $\simeq k^2_{eff}/2$ in terms of the effective electromechanical coupling coefficient. Reasonable bandwidth can be obtained by adjusting the resonance frequency of the shunt resonator to be slightly lower than the series resonator.

Various works on ladder-type FBAR filters based on zinc oxide (ZnO) and aluminium nitride (AlN) operating in the GHz frequency range can be found as early as in 1990s [16, 96-97]. For example, the work in [96] presented the 6th order ladder-type filter based on ZnO that achieved I_L around 4.0 dB, *OoB* rejection of 100 dB and centre frequency of 1.1 GHz. In [97], the ladder-type filter based on AlN is discussed. Various filter structures have been implemented such as a 3/2, which is composed with three series FBARs and two shunt FBARs, 4/3 (four series FBARs and three shunt FBARs) and 6/6 (six series FBARs and six shunt FBARs) for GPS applications. An I_L of 6.8 dB, *OoB* rejection higher than 40 dB and centre frequency at 1.48 GHz has been achieved by 6/6 structure. Later in [63], the relation between the order of the filter order (N), the I_L and the *OoB* rejection is shown with experimental results.

Ladder-type FBAR filters working at frequencies higher than 1 GHz can be found in [98-100]. In [101], the 5/3 ladder-type filter has I_L of 4 dB, *OoB* rejection of 24 dB at frequency 5.2 GHz. The work in [102] has been designed for WLAN applications from 5.15 GHz-5.35 GHz. The I_L achieved is 2 dB and *OoB* rejection of 48 dB. All the applications at frequencies of less than 6 GHz require bandwidths from 60 MHz to 200 MHz. FBAR filters operate in several ten gigahertz as has been reported in [4, 79, 81]. While much research has been done on FBAR filters in a frequency higher than 10 GHz, the applications of this filter at frequencies higher than 10 GHz are still scarce.

2.7.2 Lattice Filters

The basic configuration of a lattice filter is shown in Figure 2.8 (b). Lattice filters are characterised by the balanced input and output and the normal pole-zero response of a resonator is suppressed to give a more conventional multi-pole response. Unlike the ladder-type filters, lattice-type filters give a better *OoB* rejection due to the equal number of series and cross capacitors, which cancel the voltage across the two pairs of FBARs. However, this type of filter is not capable of performing the balanced to unbalanced conversion if these are required [103].

2.7.3 Stacked Crystal Filters

The configuration of stacked crystal filters (SCF) is presented in Figure 2.9 (a), which consists of two stacked FBARs with the central electrodes electrically grounded. With this type of filter, the FBARs are strongly coupled so that the structure acts as a single resonator. This topology presents a complex frequency response, for which different resonances occur at multiples of the frequency due to corresponding half wavelength across the whole structure [104]. The response of this filter is improved by using SMR on the limited bandwidth reflector array. However, this causes a narrowing of the obtainable bandwidths of the filter.

2.7.4 Coupled Resonator Filters

The limitation of SCF narrow bandwidth is overcome by reducing the coupling between the vertically disposed resonators. This results in a new filter topology, which is a couple resonator filter (CRF). The general configuration of CRF is depicted in Figure 2.9 (b) where the structure consists of a pair of FBARs that are acoustically coupled by means of a set of coupling layers. The filter bandwidth is controlled by the coupling layers. Unlike the SCF, the response of the CRF clearly shows two different poles. The CRF is designed so that the bandwidth is determined by the degree of coupling between the resonators and not by the inherent bandwidth of the coupling mechanism [104].

The FBAR filters discussed are summarised in Table 2.8 along with their performance for comparison. Although there are advantages and disadvantages of these filter types, the topologies of the filter depend on the applications. The ladder-type is chosen as the topology to design the FBAR filter in this current research due to its excellent performance and a lower number of resonators is required. Furthermore, the interconnect technique is straightforward and easy to implement. The reviews also suggest that FBAR filters discussed in Table 2.8 are smaller compared to the other types of filters discussed in Table 2.4. Therefore, FBAR filters are more suitable for integration to reduce cost and size of transceivers.

Table 2.8 Comparison of Ladder-Type FBAR Filter

References	Topology	Centre Frequency (GHz)	Insertion Loss (dB)	Out-of-Band (GHz)	Bandwidth (GHz)	Size (mm^2)
[4]	Ladder	29.2 23.8	-3.8 -3.8	-11 -13	0.99 0.80	--
[79]	Ladder	19.8	-4.1	-18	0.39	--
[81]	Ladder	9.08	-1.7	-21	0.27	--
[102]	Ladder	5.30	-2.8	-30	0.16	0.7x0.6
[101]	Ladder	5.2	-2.0	-24	0.17	--
[99]	Ladder	2.45 2.14	-2.4 -2.3	-40 -40	0.08 0.06	--
[104]	CRF	2.14	-0.42	-40	0.03	2.06×10^{-4}
[98]	Ladder	2.05	-2.75	-20.40	0.05	--
[79]	Ladder	2.15	-0.1	-15	0.06	--
[103]	SCF CRF	1.34 1.95	-4.5 -2.8	-- --	0.02 0.06	2.5x3.7 0.75x0.55
[16]	Ladder	1.50	-1.5	-40	--	--
[63]	Ladder	1.50 1.50	-4.0 -6.5	-20 -13.5	0.06 0.12	--
[97]	Ladder	1.48	-6.8	-40	0.05	--
[96]	Ladder	1.09	-0.6	-50		--

However, the FBAR filters reviewed are not in Ku-band and have very low bandwidth. Therefore, there is a need to undertake research to design an FBAR-based filter to achieve comparable performances in insertion loss and out-of-band rejection but with wider bandwidth and much reduced size to improve integration capability.

2.8 Ladder-Type FBAR Filter Design Methods

Most of the previous studies demonstrated the performance of the ladder-type FBAR filter, based on the fabrication measurement results. Therefore, the systematic design method for this type of filter was not specifically discussed. The novel work of Menendez in [94] presented the closed-form expression for the design of ladder-type filters that has shown very good agreement between the transmission response and the designed ladder type filter for the GPS applications [73]. The work in [63] developed the *ABCD* matrix method to calculate the S-parameters of the filter by using the chain parameters based on the input electrical impedance (Z_{in}) of the FBAR. These methods will be discussed in detail along with the equations in Chapter 3.

2.9 FBAR Design and Modelling

Modelling is a fundamental step in analysing the performance of an FBAR. Several one-dimensional (1-D) models have been proposed in order to characterise the electrical behaviour of the FBAR. The 1-D Mason model is mainly used to represent the electrical behaviour of BAW resonators and has been widely employed in work related to it [59, 95, 105-109]. The Krimholtz-Leedom-Matthaei (KLM) and Butterworth Van Dyke (BVD) model also provide a very good approach for characterising the electrical behaviour of the FBAR at fundamental modes and higher harmonics [92, 110-113]. However, the presence of spurious modes at the frequency of interest due to lateral waves cannot be predicted by 1-D modelling, therefore, the three-dimensional (3-D) simulation tool becomes important.

Commercial 3-D simulation tools for finite element modelling (FEM) analysis such as ANSYS, CoventorWare and COMSOL Multiphysics are widely employed [84, 114-116]. By using the 3-D simulation tools, more realistic behaviour of the FBAR can be modelled and studied in greater detail. Furthermore, the analytical formulation of a complex system can be reproduced in FEM analysis. There are various types of physical domain analyses available in most FEM tools, including electrostatic, magnetostatic, piezoelectric, thermal, optic, fluidic and electromagnetic [32]. For example, in FEM analysis, damping has been introduced to account for energy, which has dissipated from the systems, a feature that is not available in 1-D analysis. The next section will discuss the different types of material damping along with the estimation of each damping.

2.9.1 Material Damping

Damping is the dissipation of energy of a vibrating structure. Energy dissipation within the material is attributed to a variety of mechanisms such as thermoelasticity, grain boundary viscosity, or point-defect relaxation. Such effects are generally called material damping [117]. Rayleigh damping is one of the most popular damping forms implemented in FEM simulation tools. This form of damping is a linear combination of the mass and stiffness matrices via two negative scalar coefficients α and β as [118]:

$$[C] = \alpha[M] + \beta[K] \tag{2.1}$$

where $[C]$ is the damping matrix of the physical system, $[M]$ is the mass matrix of the physical system and $[K]$ is the stiffness of the physical system. Due to the orthogonality properties of the mass and stiffness matrices, the equation can be written as:

$$2\zeta_i \omega_i = \alpha + \beta \omega_i^2 \tag{2.2}$$

where ζ is the damping ratio in coupled mode, ω is the natural frequency of the system.

The equation can be further simplified as:

$$\zeta_i = \frac{\alpha}{2\omega_i} + \frac{\beta \omega_i}{2} \tag{2.3}$$

The relation between the Q factor and Rayleigh damping coefficients is given in the following expression which is valid at the resonance frequency [119]:

$$\frac{1}{Q} = \frac{\alpha}{\omega_s} + \beta\omega_s \qquad 2.4$$

The mass proportional damping coefficient (a) can be estimated by using a few approximations. As the system vibrates, the wave propagates through a solid; the energy of the wave scatters, diffracts, couples to electron motion, and attenuates. The attenuation in the material is categorised as follows [120]:

1) Thermoelastic attenuation
2) Akhieser attenuation (phonon-viscosity attenuation)
3) Electron-phonon interactions
4) Coupling of electrons in a piezoelectric semiconductor
5) Attenuation due to imperfections in single crystals

According to the study in [120], the first two mechanisms, the thermoelastic attenuation and Akhieser attenuation, are the most important in single crystals at room temperature and both mechanisms produce attenuations, which increase with the square of frequency since they are similar. The thermoelastic and Akhieser mechanisms occur from the return to thermal equilibrium of the crystal through interactions between ultrasonic phonons and the thermal phonons which is due to the anharmonic of lattice vibrations. The following sub-section presents a detailed explanation on both thermoelastic and Akhieser attenuation.

2.9.1.1 Thermoelastic Attenuation

Thermoelastic attenuation occurs because of the irreversible heat transmission from the compressed areas of a longitudinal wave to the expanded areas. The calculation of the thermoelastic attenuation due to thermoelastic heat flow in a medium is done with the assumption that Hooke's Law is valid. Longitudinal wave propagation distorts the vibrating lattice cyclically. The heat flows through conduction as the compression of the area results in increasing the temperature. As a result, the compression amplitude decreases and an attenuation of the wave occurs. At low frequencies, the effect is smaller than at higher frequency due to the shorter wavelength. The relaxation attenuation is found to go as ω^2 up to a frequency where $\omega\tau$~1, beyond which the attenuation is constant and valid at microwave frequency up to 100 GHz in solid state at room temperature [120]. Generally, the frequency dependence is given as:

$$\frac{\omega^2\tau^2}{1+\omega^2\tau^2} \qquad 2.5$$

where τ is the thermal relaxation time.

For $\omega^2\tau^2$<<1, the attenuation is given as:

$$\alpha = \frac{c_{11}^{ad} - c_{11}^{iso}}{c_{11}} \frac{\omega^2 K}{2pC\upsilon^3} \qquad 2.6$$

where c_{11} is the element of the stiffness tensor, K is the thermal conductivity, ρ is the mass density, C is the specific heat per unit volume and ν is the longitudinal acoustic velocity.

For an isotropic material, the attenuation is given as:

$$\alpha = \frac{8.68\omega^2\beta^2 KT^{'}\left(c_{11} + 2c_{12}\right)^2}{2p^2C^2c_{11}\upsilon^3} \qquad 2.7$$

where β is the thermal expansion coefficient, T' is the temperature and c_{12} is the stiffness. The attenuation is high in material with high thermal expansions and thermal conductivity. In the study, the attenuation of ZnO is calculated to be 0.59 dB/cm at 1 GHz.

2.9.1.2 Akhieser Attenuation

Akhieser is the most important attenuation mechanism involving phonon-phonon scattering. Landau and Rumer discussed the attenuation for $\omega\tau \geq 1$ and Akhieser explained the attenuation for $\omega\tau$<<1. Later, Woodruff and Ehrenreich modified Akhieser's theory by including phonon gas. The results from Woodruff and Ehrenreich for $\omega\tau$<<1 are given as:

$$\alpha = \frac{\omega^2 \gamma^2 K T'}{p \upsilon^5} \qquad 2.8$$

and for $\omega\tau$>1,

$$\alpha = \frac{\pi \omega \gamma^2 C T'}{4 p \upsilon^3} \qquad 2.9$$

where γ is the Gruneisen constant, K is the lattice thermal conductivity, T' is the absolute temperature, ρ is the mass density, C is the specific heat per unit volume and ν is the longitudinal acoustic velocity.

As seen from equation 2.8, the attenuation goes as ω^2 up and the lattice thermal conductivity and the Gruneisen constant are included. This equation also fits the experimental data fairly well, if all the quantities of the material are known with adequate precision. The Gruneisen numbers for the longitudinal wave is 1.2 and 0.6 for shear wave as presented in [121]. The attenuation of AlN given in [120] is 0.08 dB/cm at 1 GHz.

The value of the stiffness proportional damping coefficient (β) is estimated by using the 1-D viscoelastic wave equation as explained in [122] given as:

$$C_0^2\left(\delta^2 w/\delta z^2\right) + \mu / \rho\left(\delta^3 w/\delta t \delta z^2\right) = \left(\delta^2 w/\delta t^2\right) \qquad 2.10$$

where $C_0=\sqrt{(Y/p)}$ is the wave speed in the undamped material, Y is the material elastic stiffness (C_{33}), μ is the material viscosity in a Maxwell model for viscoeleastic response and w is the particle displacement in z-direction. This equation can be written in the form $w(z,t)=Ae^{\pm(\lambda_1+j\,\lambda_1)z+j\omega t}$ where A is a constant and results in

$$\lambda_{1,2} = \frac{\omega}{c_0\sqrt{2}} \frac{1}{\sqrt{1+(\mu\omega/Y)^2}} \sqrt{\sqrt{1+\left(\frac{\mu\omega}{Y}\right)^2} \mp 1} \qquad 2.11$$

where λ_1 is the real part that is referred to as the attenuation coefficient characterise the damping and a measure of the decrease in amplitude of the wave in distance while λ_2 is related to the velocity at which the wave propagates (ω/λ_2). At frequencies higher than 1 GHz, the coefficient λ_1 can be approximated as $\lambda_1 \approx (\omega^2\mu\sqrt{p})2Y^{3/2}$ yielding the approximate value of the damping coefficient β in terms of material constant as

$$\beta = \mu/Y \approx \left(2\lambda_1/\omega^2\right)\sqrt{(Y/\rho)} \qquad 2.12$$

2.10 Conclusion

This chapter provided a review of Ku-band transceivers. The major issues of Ku-band transceivers are their large size and heavy due to discrete components such as filters and other sub-modules located on the same or different printed circuit board (PCB). Various types of Ku-band filters that have been implemented in Ku-band transceivers were discussed, as well as the advantages and disadvantages of the current integration and implementation of these Ku-band filters. It can be seen there are various types of Ku-band filters that have been manufactured using a variety of manufacturing methods. These filters have shown reasonably good performance but are quite large in size. Filters based on FBARs with frequencies lower than 10 GHz have shown better performance, smaller size and widely used in current wireless communications applications compared to other filters. FBARs are comparatively smaller in size and are silicon, CMOS, silicon germanium (SiGe) technology compatible. In terms of integration, FBAR is also compatible with LTCC technology, which has been implemented in WiFi and WiMAX applications. Therefore, it is expected that filters based on FBARs will replace these current Ku-band filters with the same good performance. The FBARs designed in the studies reviewed are not in a suitable band, and have lower k^2_{eff}, a narrow bandwidth and a low Q factor. Hence, there is need for research in novel design to develop an FBAR, which operates in the 15 GHz to 16 GHz range with wide bandwidth, high k^2_{eff} and a suitable Q factor with the smallest size for a high level of integration. As mentioned in the literature, FBAR filters have been designed in X-band (10 GHz), K-band (20 GHz) and Ka-band (30 GHz). These FBAR filters are not in Ku-band and have bandwidths of less than 1 GHz. Thus, this present study seeks to address this gap by developing FBAR filters in Ku-Band to achieve comparable performances in insertion loss and out-of-band rejection but with wider bandwidth and a much reduced size to improve integration capability. The target specifications for Ku-band FBAR filters are based on the specifications in Table 2.3, where the operating frequencies are from 15 GHz to 16 GHz with centre frequency at 15.5 GHz.

CHAPTER 3 : FILM BULK ACOUSTIC WAVE RESONATOR (FBAR) FILTER

3.1 Introduction

This chapter presents a detailed discussion on the theory of film bulk acoustic wave resonators (FBAR). The review includes an overview of piezoelectric and acoustic propagation theory and contemplates the important characteristics of FBARs such as quality (Q) factor and electromechanical coupling coefficient (k^2_{eff}). The design methodology of FBARs and FBAR filters using 1-dimensional (1-D) and 3-dimensional (3-D) finite element methods (FEM) are also presented in this chapter. The theory and important characteristics of ladder-type FBAR filter such as insertion loss (I_L), out-of-band (OoB) rejection, and bandwidth (BW) are discussed along with losses from piezoelectric material such as thermoelastic damping and material.

3.2 Theory of Piezoelectric

Piezoelectricity means “pressing” electricity which is the link between electrical and mechanical phenomena [107]. The piezoelectric thin films convert electrical energy to mechanical energy and vice versa depending on the design and application. This thin film is sandwiched between two electrodes where the electric field is applied. The direct piezoelectric effect occurs when mechanical stress is applied to piezoelectric materials; the crystalline structure produces a voltage proportional to the stress. This phenomenon is shown in Figure 3.1. If an external stress (F) is applied in the piezoelectric material, a voltage appears between the electrodes due to deformation of the dipole. If the stress changes from compressive to tensile, the voltage on the electrodes changes to the opposite polarity.

A converse piezoelectric effect occurs when an electric field is applied to the material, an internal strain and deformation results if its boundaries are free to move, as shown in Figure 3.1. If a voltage with opposite polarity is applied to the electrodes, the piezoelectric material will contract but if the polarity of the applied voltage is the same as the voltage pole, the piezoelectric materials will expand and if alternating voltage is applied, the piezoelectric material will alternately contract and expand. Within the methodological framework underlying this thesis, the FBAR converts the electrical energy to acoustic energy by applying a voltage to create wave propagation in the piezoelectric material.

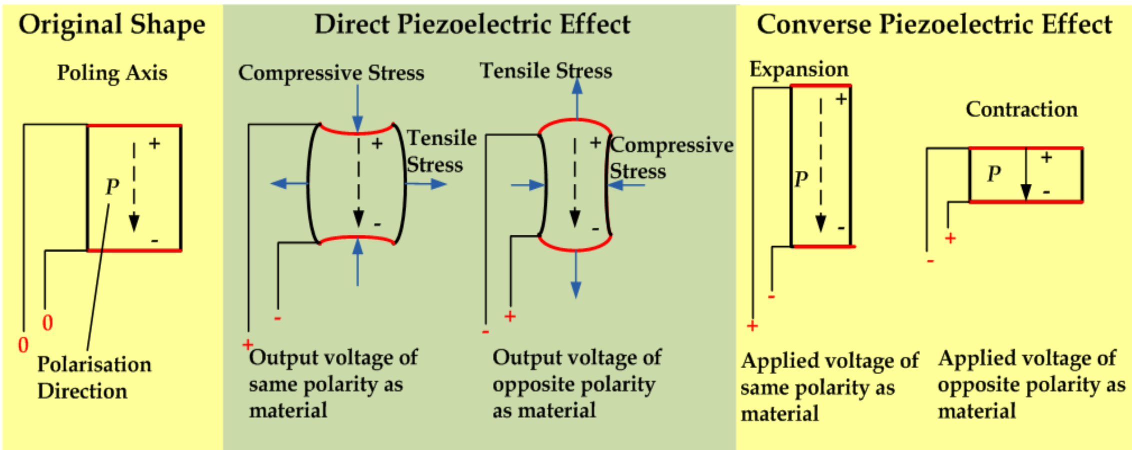

Figure 3.1 Piezoelectric Effect on Piezoelectric Materials [123]

3.2.1 Piezoelectric Constitutive Equations and Constants

The coupling between electrical polarisation and strain that occurs in piezoelectric material generates acoustic waves electrically. The Christoffel equation for piezoelectric classes developed in [107] shows the dependence of piezoelectricity on the crystal orientation. It describes how mechanical stress (T), strain (S), electric displacement (D) and electric fields (E) interact with each other. There are four pairs of constitutive equations describing piezoelectric materials which are given in the full tensor notation forms as below [107]:

(a) Piezoelectric stress matrix (e-form)

$$T_{ij} = c^{E}_{ijkl} S_{kl} - e_{ijk} E_k \qquad 3.1$$

$$D_i = e_{ijk} S_{jk} - \varepsilon^{S}_{ij} E_j$$

(b) Dielectric strain matrix (h-form)

$$T_{ij} = c^{D}_{ijkl} S_{kl} - h_{ijk} D_k \qquad 3.2$$

$$E_i = -h_{ijk} s_{jk} + \beta^{S}_{ij} D_j$$

(c) Piezoelectric strain matrix (d-form)

$$S_{ij} = s^{E}_{ijkl} T_{kl} + d_{ijk} E_k \qquad 3.3$$

$$D_i = d_{ijk} T_{jk} + \varepsilon^{T}_{ij} E_j$$

(d) Dielectric strain matrix (g-form)

$$S_{ij} = s^{D}_{ijkl} T_{kl} + g_{ijk} D_k \qquad 3.4$$

$$E_i = -g_{ijk} T_{jk} + \beta^{T}_{ij} D_j$$

where T_{ij} = stress (Nm^{-2}), S_{ij} = strain (dimensionless), D_i = electric displacement (Cm^{-2}) and E_i = electric field (Vm^{-1}). The terms s^{D}_{ijkl} and s^{E}_{ijkl} are the specific elastic compliance matrix (strain-to-stress ratio) for a constant electric charge density and constant electric field, respectively. ε^{T}_{ij} and ε^{S}_{ij} are the dielectric or permittivity constants matrix (Fm^{-1}) at constant stress and strain, respectively. The terms c^{D}_{ijkl} and c^{E}_{ijkl} are the elastic stiffness (stress-to-strain ratio). h_{ijk} and

e_{ijk} are the piezoelectric stress constant matrix. s_{jk} and c_{ijkl} present the quantity kept constant under boundary conditions. For example, ε_{ij}^{T} is the permittivity under constant stress. β_{ij}^{S} is the permittivity constant matrix.

3.2.2 Description of Excitation and Vibration Mode

Acoustic resonances are high-order modes often denoted by the nomenclature of the excitation-actuation axes, instead of designating them in the mode sequence manner of fundamental and first modes of electromechanical resonators [32]. The excitation axis is defined by the crystal poling and the poling axis, P, determines the wave propagation. There are four main configurations of vibration modes of acoustic resonators as shown in Figure 3.2: (a) longitudinal ("33" mode); (b) extensional ("31"mode); (c) thickness-transversal ("31"shear mode); and (d) lateral-shear ("15"mode).

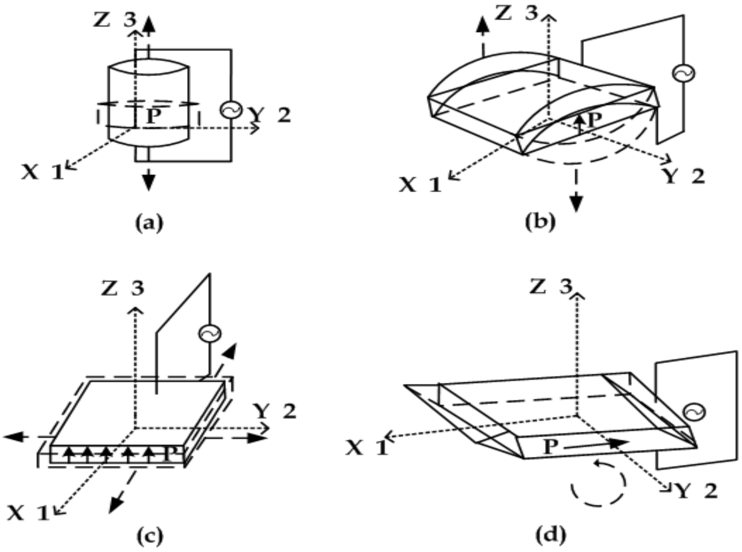

Figure 3.2 Vibration Modes of Acoustic Resonators [32]

The longitudinal and shear modes are typically excited in BAW resonators, while the transversal and lateral modes usually occur in SAW resonators. The boundary conditions of this resonator configuration simplify the equations 3.1 to 3.4 and thus simplify the implementation of models and calculations. In this study, only the thickness excitation of the thickness vibration or longitudinal mode ("33") is considered. The electric field E_3 and mechanical stress T_3 applied in the three-axis generate electrical displacement D_3 and mechanical strain S_3. Using these conditions, equation 3.3 can be simplified as below:

$$\begin{bmatrix} S_1 \\ S_2 \\ S_3 \\ S_4 \\ S_5 \\ S_6 \end{bmatrix} = \begin{bmatrix} s_{11}^E & \cdot & \cdot & \cdot & \cdot & \cdot \\ \cdot & s_{22}^E & \cdot & \cdot & \cdot & \cdot \\ \cdot & \cdot & s_{33}^E & \cdot & \cdot & \cdot \\ \cdot & \cdot & \cdot & s_{44}^E & \cdot & \cdot \\ \cdot & \cdot & \cdot & \cdot & s_{55}^E & \cdot \\ \cdot & \cdot & \cdot & \cdot & \cdot & s_{66}^E \end{bmatrix} \cdot \begin{bmatrix} 0 \\ 0 \\ T_3 \\ 0 \\ 0 \\ 0 \end{bmatrix} + \begin{bmatrix} d_{11} & \cdot & \cdot \\ d_{21} & d_{22} & \cdot \\ d_{31} & d_{32} & d_{33} \\ \vdots & \vdots & \vdots \\ \cdot & \cdot & \cdot \end{bmatrix} \cdot \begin{bmatrix} 0 \\ 0 \\ E_3 \end{bmatrix}$$

3.5

$$\begin{bmatrix} D_1 \\ D_2 \\ D_3 \end{bmatrix} = \begin{bmatrix} d_{11} & \cdot & \cdot \\ d_{21} & d_{22} & \cdot \\ d_{31} & d_{32} & d_{33} \\ \vdots & \vdots & \vdots \\ d_{61} & \cdot & \cdot \end{bmatrix} \cdot \begin{bmatrix} \cdot \\ \cdot \\ T_3 \\ \cdot \\ \cdot \\ \cdot \end{bmatrix} + \begin{bmatrix} \varepsilon_{11}^T & \cdot & \cdot \\ \cdot & \varepsilon_{22}^T & \cdot \\ \cdot & \cdot & \varepsilon_{33}^T \end{bmatrix} \cdot \begin{bmatrix} 0 \\ 0 \\ E_3 \end{bmatrix}$$

Equation 3.5 can be further simplified as:

$$S_3 = s_{33}^E \cdot T_3 + d_{33} \cdot E_3 \qquad 3.6$$

$$D_3 = d_{31} \cdot T_1 + \varepsilon_{33}^T \cdot E_3$$

3.3 The FBAR Concept

FBAR is one of the technologies for fabricating BAW devices, the first FBAR device being released by Lakin and Wang in 1981 [124]. Figure 3.3 shows the acoustic wave propagation in FBAR through its active layer structure, which is usually a piezoelectric material. The acoustic wave causes the deformation of the piezoelectric material. Therefore, the actuation and detection mechanisms involved in FBAR operation are due to the piezoelectric and inverse piezoelectric effects. By using these principles, a voltage applied to the resonator's electrodes induces strain of the acoustic layer, and vice versa, and following a mechanical strain of the acoustic layer a voltage can be read out of the electrodes [32].

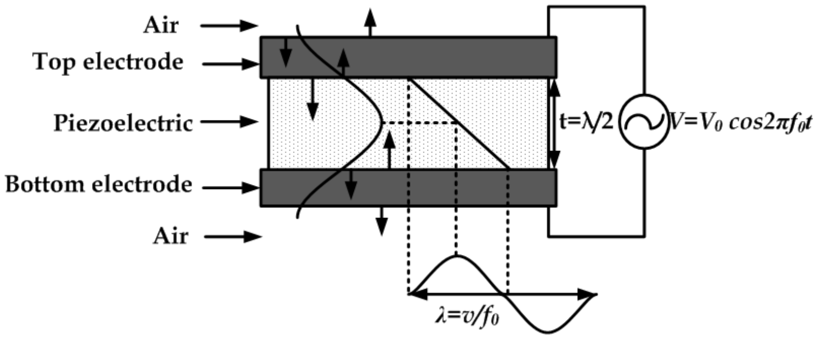

Figure 3.3 Bulk Acoustic Wave Propagation in FBAR [32]

According to [124], the resonance frequency of an FBAR operating in fundamental, longitudinal mode is determined mainly by the thickness (t) of the piezoelectric layer given as:

$$\theta = \frac{2\pi f_0 t}{\upsilon^D} \tag{3.7}$$

where θ is the phase, υ^D is acoustic velocity, f is the frequency of acoustic wave propagating through the bulk acoustic layer and t is the thickness of the piezoelectric film. The acoustic velocity can be calculated using the approximation given in [106]:

$$\upsilon^D = \sqrt{\frac{c_{33}^D}{\rho}} \tag{3.8}$$

where $c^D{}_{33}$ is the elastic stiffness at constant electric displacement and ρ is the density of the piezoelectric material.

At resonance (f=f_0), the acoustic phase of the film is θ=π, under these conditions, the f_0 can be calculated as in [32]:

$$f_0 = \frac{\upsilon_l}{2t} \quad 3.9$$

From equation 3.9, it follows that resonance occurs when the film thickness is equal to half the wavelength of the acoustic wave. As shown in Figure 3.3, the acoustic wave is confined by the reflecting electrode surfaces at the thin film interface where t must be half the acoustic wavelength, ignoring the electrode loading effects. According to [111], the contribution of the electrode to equation 3.9 must be taken into account since it reduces resonant frequency.

3.3.1 Characteristic of Input Electrical Impedance

The input electrical impedance (Z_{in}) of an FBAR is characterised by two resonant frequencies, f_s where the magnitude of electrical impedance is minimum, and f_p where the magnitude of electrical impedance is maximum. The input electrical impedance of an FBAR is shown in Figure 3.4. The figure also shows that the phase between resonant frequencies is 90° behaving as an inductor, while outside these frequencies it is -90° with a pure capacitive behaviour.

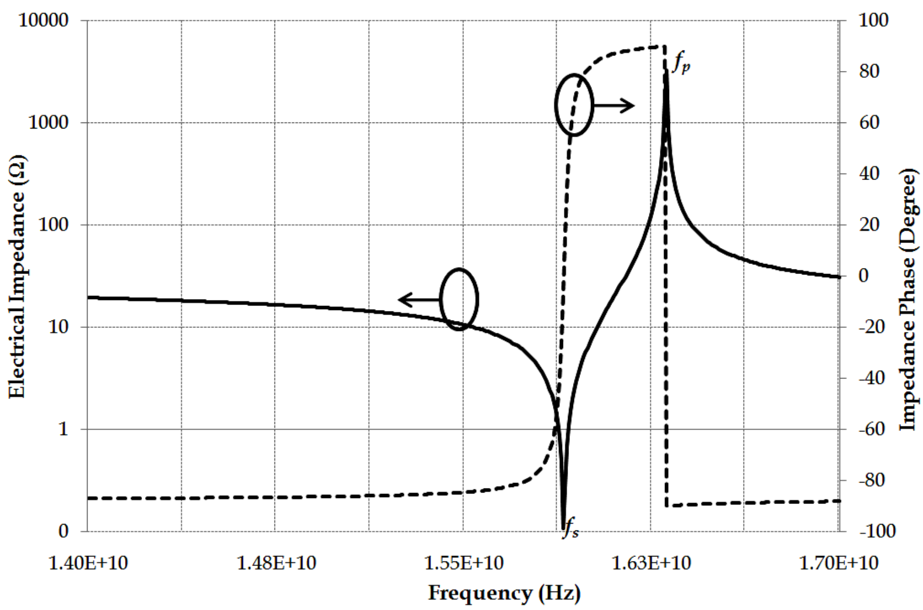

Figure 3.4 Input Electrical Impedance of an FBAR

3.3.2 Electromechanical Coupling Coefficient

The electromechanical coupling coefficient ($k^2{}_t$) is the most important parameter in designing an FBAR because the bandwidth of an FBAR filter is directly proportional to the coupling coefficient of the FBAR. Therefore, $k_t{}^2$ is one of the biggest challenges in FBAR. From [106], $k^2{}_t$ is dependent on the piezoelectric material properties given as:

$$k_t^2 = \frac{e_{33}^2}{c_{33}^D \varepsilon_{33}^S} \tag{3.10}$$

where $e^2{}_{33}$ is the piezoelectric constant and $\varepsilon^S{}_{33}$ is the dielectric permittivity. For a lossless resonator with a single piezoelectric layer and ignored electrodes, the $k_t{}^2$ for the thickness extensional mode is given by [107]:

$$k_t^2 = \left(\frac{\pi}{2}\right) \cdot \frac{f_s}{f_p} \cdot \tan\frac{\pi}{2}\left(\frac{f_p - f_s}{f_p}\right) \tag{3.11}$$

When $k_t{}^2$ is small, the equation 3.11 is approximated to

$$k_t^2 = \frac{\pi^2}{4} \cdot \frac{f_s}{f_p} \cdot \frac{f_p - f_s}{f_p} \tag{3.12}$$

According to [125] the relative difference in frequencies f_s and f_p depends on both the material coupling factor and the resonator geometry. For this reason, the effective coupling factor ($k^2{}_{eff}$) has been used in filter design literature as a convenient measure of the difference. From the input electrical impedance of a resonator, $k^2{}_{eff}$ is defined as:

$$k_{eff}^2 = \left(\frac{\pi^2}{4}\right)\left(\frac{f_p - f_s}{f_p}\right) \tag{3.13}$$

3.3.3 Quality (*Q*) factor

Quality (*Q*) factor is a measure of the loss of a resonant circuit and is defined as the ratio of the stored energy divided by the power dissipated in that network over one cycle [126]. Some of the causes of losses in FBARs are electrical resistivity of the electrodes, acoustic leaks, substrate conductivity and acoustic propagation losses [15, 127]. Eddy current losses are also mentioned in the literature [128]. In [129], *Q* is defined as a function of the frequency, and in this way, the *Q* factor in an FBAR is defined both at the series resonance frequency (Q_s) and at the parallel resonance frequency (Q_p).

Several methods can be found in the literature to calculate the *Q* factor, for example, calculations based on the Butterworth Van Dyke (BVD) model [130] or evaluation from the phase angle (imaginary part) of the electrical impedance [131] given as:

$$Q_{s/p} = \frac{f_{s/p}}{2}\left[\frac{d\angle Z_{in}}{df}\right]_{f_s/f_p} \tag{3.14}$$

The study in [57] shows that in filter applications, the figure of merit (FOM) is useful in determining the insertion loss of the filter and it is inversely proportional to the filter insertion loss. The FOM is defined as:

$$FOM = k_{eff}^2 \cdot Q_{s/p} \tag{3.15}$$

3.3.4 1-D Modelling

3.3.4.1 1-D Mason Model

The Mason model has been widely used in deriving solutions for the wave propagation through the acoustic layer by using the network theory approach. Figure 3.5 shows the thickness excitation of the piezoelectric layer, ignoring the electrodes.

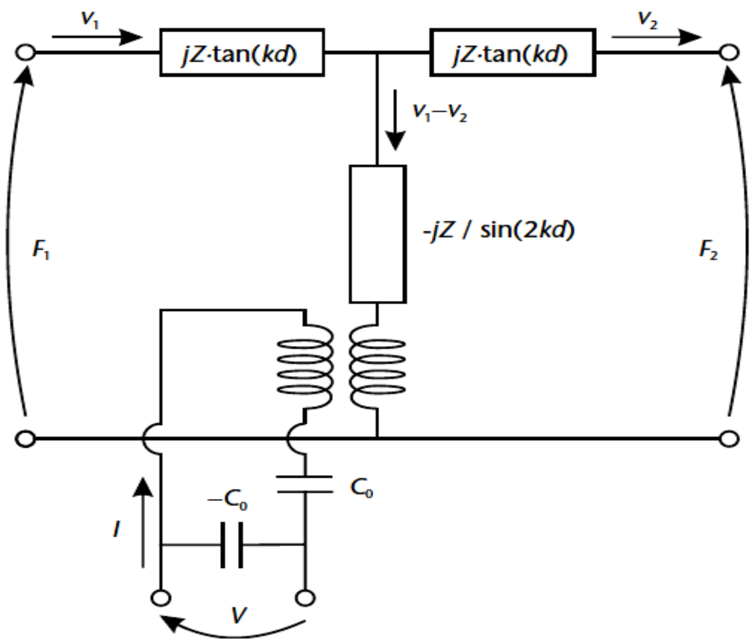

Figure 3.5 Three-Port Mason's Model Equivalent Circuit [15]

The piezoelectric layer can be seen as a three-port component. Two ports are the mechanical ports presented by the forces (F) and the displacement velocity (v). The other port is the electrical port given by voltage (V) and current (I). The electrical input impedance of a single piezoelectric layer is given as in [107]:

$$Z_{in} = \frac{1}{j\omega C_0}\left(1 - k_t^2 \frac{\tan(kd/2)}{kd/2}\right) \qquad 3.16$$

where d is the thickness of the piezoelectric layer. F_1 and F_2 are the forces on the top and bottom surface of the resonator, respectively. v_1 and v_2 represent the acoustic velocities of the top and bottom surface plane of the resonator, respectively. V is the external electric voltage and I is the current. C_0 is the static capacitance, $\omega=2\pi f$ is the angular frequency, $k=\omega/v_L$ where v_L is the longitudinal acoustic wave velocity and $h=e/\varepsilon^s$ where e is piezoelectric coefficient and ε^s is the permittivity of the piezoelectric layer. k_t^2 can be computed using equation 3.10; while C_0 is given as:

$$C_0 = \frac{\varepsilon^S A}{d} \qquad 3.17$$

where A is the area.

However, FBARs comprise more than one layer. The mass loading effects are related to the deposition of metal electrodes on the piezoelectric layer. These effects can be associated with resonant frequency shifting, which are also known as inertial effects, with the concept of energy trapping, and with the stress in the structure [54, 132-133]. For this reason, when electrodes are included in the structure, the intrinsic k^2_t will be recalled as k^2_{eff}. The electrical input impedance (Zin) of the piezoelectric layer between two parallel electrodes as shown in Figure 3.6 is given as [134]:

$$Z_{in} = \frac{1}{j\omega C_0} \times \left(1 - k_{eff}^2 \frac{\tan\theta}{\theta} \frac{(z_T + z_B)\cos^2\theta + j\sin 2\theta}{(z_T + z_B)\cos 2\theta + j(z_T + z_B + 1)\sin 2\theta}\right) \qquad 3.18$$

where Z_T and Z_B are normalised acoustic impedance at the piezoelectric layer boundaries and θ is the half phase across the piezoelectric plate given as $\theta=k \times t$ where $k=\omega/v_L$.

The boundary impedances Z_T and Z_B at the interface between the piezoelectric layer and the electrodes are determined by the acoustic impedance matching between both mediums. The values of Z_T and Z_B can be computed as given in [135]:

$$Z_{T/B} = Z_0^{T/B} \times \left(\frac{Z_{load} \cos\theta_{T/B} + jZ_0^{T/B} \sin\theta_{T/B}}{Z_0^{T/B} \cos\theta_{T/B} + jZ_{load} \sin\theta_{T/B}} \right) \quad 3.19$$

where $Z_0^{T/B}$ is the characteristic acoustic impedance of either top (T) or bottom (B) electrode layers, where Z_0 is given as:

$$Z_0 = A\rho\upsilon_L \quad 3.20$$

where A is the area, ρ is the density and ν_L is the longitudinal acoustic wave velocity. Z_{load} is the input load impedance seen by either the top or the bottom electrode layers and $\theta_{T/B}$ is the acoustic-wave phase across either the top or the bottom electrode layers. Simulation tools such as MATLAB can be used to model the acoustic impedance using this equation.

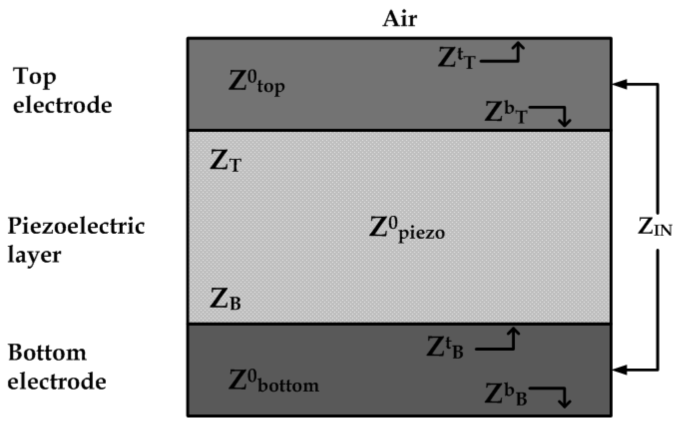

Figure 3.6 Cross-Section View of the FBAR with Equivalent Impedance Values and Input and Output Ports [32]

3.3.4.2 The Butterworth Van Dyke (BVD) Model

The Mason model may be simplified to the six-lumped element model [98] under the assumption that FBARs have very thin electrodes. The Butterworth-Van Dyke (BVD) model is a common lumped element equivalent circuit model used by the crystal filter to simplify the transcendental functions that totally characterise the resonators used as filter elements [136]. This BVD model, as shown in Figure 3.7 (a), comprises of a series motional inductor (L_m), motional capacitor (C_m) and motional resistor (R_m) resonator in parallel with static capacitance (C_o). The C_o is the electrical capacitance between the two electrodes through which the electric fields are applied. The motional components (C_m, L_m and R_m) represent the electromechanical response of a piezoelectric material.

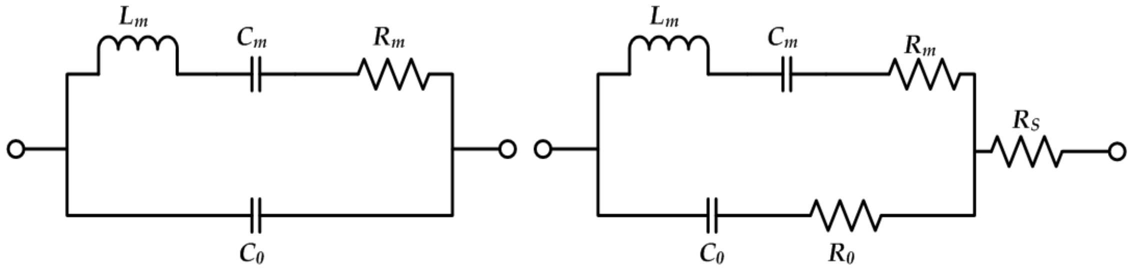

(a) BVD equivalent circuit (b) MBVD equivalent circuit

Figure 3.7 Equivalent Circuit for Acoustic Resonator

BVD model is the most convenient model to use but if the loss from the electrodes is to be considered then the modified Butterworth Van Dyke Circuit (MBVD) as shown in Figure 3.7 (b) is adopted instead. The MBVD includes the dielectric loss (R_o) of the piezoelectric material and electrical losses (R_s) of the electrodes [130]. This model provides a better method, both simple and accurate, for characterising FBARs and designing bandpass filters. The derived equations for equivalent circuit elements of FBAR are as follows [137]:

$$C_m = \frac{\left(8k_{eff}^2\right)}{N^2\pi^2}C_0 \qquad 3.21$$

$$L_m = \frac{\pi^3 \upsilon_a}{8\varepsilon_r\varepsilon_0 A\omega_S^3 k_{eff}^2} \qquad 3.22$$

$$R_m = \frac{\pi\eta\varepsilon_r\varepsilon_0}{8k_{eff}^2\rho A\omega_s\upsilon_a} \quad 3.23$$

$$\omega_s^2 = \frac{1}{L_m C_m} \quad 3.24$$

$$Q_s = \frac{\omega_s L_m}{R_m} \quad 3.25$$

$$Q_p = Q_s\sqrt{1+\frac{C_m}{C_0}} \quad 3.26$$

$$Z(\omega) = \frac{j(\omega L_m - 1/\omega C_m)}{1-\omega^2 C_0 L_m + C_0/C_1} \quad 3.27$$

where ε_r is relative permittivity of the piezoelectric material, ε_o is permittivity of free space, ρ is density, ν^D is acoustic velocity, A is resonator size, d is the thickness of piezoelectric film, $k^2{}_{eff}$ is piezoelectric coupling coefficient, ω_s is the series resonant frequency and η is acoustic viscosity related to the imaginary part of the wave vector $\kappa = \widetilde{k_r} + j \cdot \widetilde{k_i}$ by:

$$\tilde{k}_i = \frac{\eta\omega}{2\rho\upsilon^{D^2}} \times \left(\frac{\omega}{\upsilon^D}\right) \quad 3.28$$

3.3.5 3-D Finite-Element Modelling (FEM)

The 1-D Mason model and the BVD equivalent circuit described previously are a suitable approach to characterise the electrical behaviour of the FBAR for its fundamental mode and higher harmonics operation. However, the FBAR is composed of different layers, which is the piezoelectric film and electrodes with finite lateral dimensions. The 1-D models do not take into account the effects due to lateral waves. Therefore, computer-aided three-dimensional (3-D) finite-element modelling (FEM) becomes important. FEM is a powerful numerical-analysis tool that allows accurate prediction of the static and dynamic responses of a multiple-domain physical system [32]. By using the 3-D FEM, the electrical behaviour of the FBAR can be completely characterised, and the boundary conditions required, as well as the origin of lateral standing waves can then be stated [54]. The FEM stores the computation nodes required by the Analyzer to compute a 3-D mechanical solution using numerical techniques [138]. There are many FEM simulation tools available in the market such as ANSYS, CoventorWare and COMSOL. In this work, CoventorWare ® 2010 is used as the simulation tool. Figure 3.8 shows the process design flow of the CoventorWare comprising Architect, Designer, Analyzer and Integrator modules that can be used individually to complement an existing design flow or in combination to provide a complete MEMS design flow.

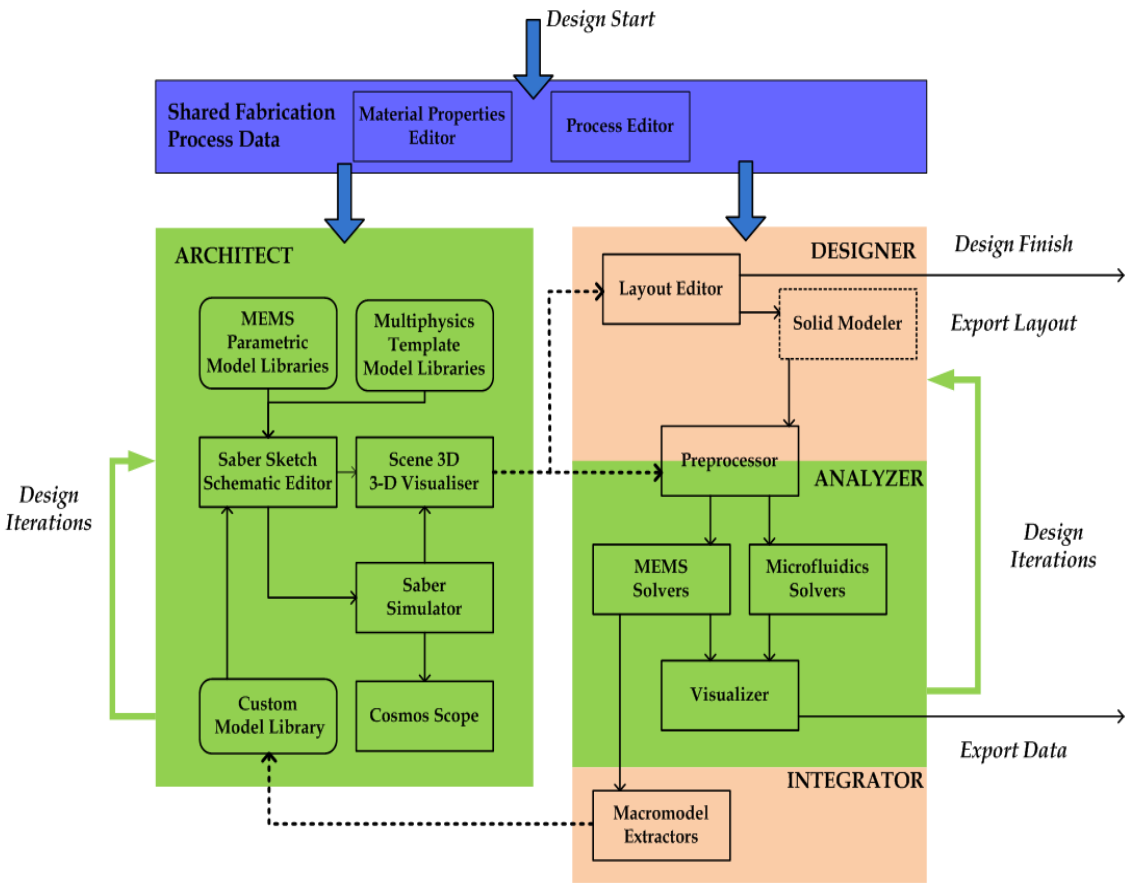

Figure 3.8 Process Design Flow [138]

The functions of each module are explained as in [138]:

1) Architect - Assembles a schematic of the MEM device using specific libraries of parameterised, MEMS-specific behavioural models and simulates them together with surrounding electronics within a schematic-based system-level modelling environment.

2) Designer - Provides the environment for the fabrication process, MEMS-specific layout editor for layout creation and automatically generates and visualises 3D solid models for input into the field solver.

3) Analyzer - Analyses and verifies the physical behaviour of any MEMS or microfluidic design using the 3D field solvers with optimisation for MEMS-specific coupled physics.

4) Integrator - Extracts linear and non-linear reduced-order MEMS behavioural models that are compatible with Architect.

3.3.5.1 Building the model

In this study, piezoelectric analysis is chosen to design and simulate the FBAR. The steps of designing and analysing the FBAR were based on [119]. Firstly, the Material Properties Database is checked and validated before a process file is created to verify the material exists and has correct values. Then, using the Process Editor, the process file is created to model the fabrication steps. At the Process Library, users can choose from the top-down menu the folders that contain the process required. In Modelling Actions, it contains generic solid modelling actions such as Stack Material, Straight Cut, Partition and many others. In User-Defined Steps, users can choose the predefined process steps such as Reactive Ion Etch (RIE), Generic Wet Etch and others. In the Foundry

Process, users have a variety of choices of recognised foundry processes such as PolyMUMPS, SoiMUMPS, INTEGRAMplus Metal Nitride (MPK) and many others. Each of the steps is explained in the comments box.

Once the process file had been created, the 2-D mask layout was drawn in the Layout Editor. Then, using the mask, the process steps and material properties defined in the previous steps, the 3-D model is built. Each of the surfaces and the layer of the model are named. Lastly, the 3-D model is meshed in order to undertake the FEM analysis. Several meshers can be selected such as Manhattan Brick and Extruded Brick, depending on the model created. In this present study, only the piezoelectric layer, top electrodes and bottom electrodes are considered in the mesh, as these layers principally contribute the characteristics of FBARs.

3.3.5.2 Structural, Modal and Harmonic Analysis

The steps for the analysis of the FBAR are as follows:

1) Direct Current (DC) Analysis:

The DC analysis was run on the piezoelectric stack using MemMech solver with a nominal value of 1V applied on the top electrode. From this simulation, the FBAR electrical parameters such as potential, displacement and stress, as well as the static capacitance (C_0) can be observed. C_0 can be calculated by using the following equation:

$$C_0 = Q/V \tag{3.29}$$

where Q is the piezoelectric charge response and V is the voltage applied to the piezoelectric layer.

2) Frequency Analysis (Modal Analysis):

Modal analysis is carried out to estimate the f_s and f_p of the FBAR. First, closed-circuit resonance analysis is performed to extract the series resonant frequency of the FBAR. Then, open-circuit analysis is done to determine the parallel resonance frequency of the FBAR. From the values of f_s and f_p obtained through the simulation, C_m and L_m are calculated using the equations as given in [139]:

$$C_m = C_0\left[\left(\frac{\omega_s}{\omega_p}\right)^2 - 1\right] = C_m\left[\left(\frac{f_s}{f_p}\right)^2 - 1\right] \qquad 3.30$$

$$L_m = \frac{1}{\omega_s^2 C_m} = \frac{1}{(2\pi f_s)^2 C_m} \qquad 3.31$$

3) Frequency Response Analysis (Harmonic Analysis):

Frequency response analysis was done to obtain the Q factor and electrical input impedance (Z_{in}) of the FBAR. In this analysis, the electrical impedance magnitude can be computed from the result of piezoelectric patch charge using the equations given in [119]:

$$Omega = 2 * PI * Frequency \qquad 3.32$$

$$Q\_\mathrm{Re} = pztop\_Q\_Mag * \cos\left((pztop\_Q\_Phase) * \frac{PI}{180}\right) \qquad 3.33$$

$$Q\_\mathrm{Im} = pztop\_Q\_Mag * \sin\left((pztop\_Q\_Phase) * \frac{PI}{180}\right) \qquad 3.34$$

$$Z\_\mathrm{Re} = -1e12(Omega) * (Q\_\mathrm{Im}) / ((Q\_\mathrm{Re}) ** 2 + (Q\_\mathrm{Im}) ** 2) \qquad 3.35$$

$$Z\_\mathrm{Im} = -1e12(Omega)*(Q\_\mathrm{Re})/((Q\_\mathrm{Re})**2 + (Q\_\mathrm{Im})**2) \qquad 3.36$$

$$(Z\_Mag) = sqrt((Z\_\mathrm{Re})** + (Z\_\mathrm{Im})**2) \qquad 3.37$$

$$(Z\_Phase) = \frac{180}{PI} * a\tan 2((Z\_\mathrm{Im}),(Z\_\mathrm{Re})) \qquad 3.38$$

where *Q_Re*, *Q_Im*, *Z_Re*, *Z_Im*, *Z_Mag*, and *Z_Phase* are the real charge, imaginary charge, impedance real, impedance phase, impedance magnitude and impedance phase respectively. *pztop_Q_Mag* and *pztop_Q_phase* are the magnitude and phase of the patch charge on the electrode top and are computed directly by the simulation tool.

3.3.5.3 Losses in FBARs

Many factors contribute to the losses in FBAR and these can be measured by its *Q* factor. In 1-D modelling, the piezoelectric material is assumed free from damping. However, in 3-D FEM, damping should be considered in order to present an FBAR with behaviour that is more realistic. The damping needs to be calculated before including it in the simulation. There are different types of losses that contribute to the *Q* factor such as material damping, thermoelastic damping, acoustic radiation losses through anchors, gas and other less important damping.

The system *Q* factor is given in equation 2.4 by Rayleigh damping coefficients (a and β) where a is mass proportional damping and β is stiffness proportional damping. a is used to damp out the lowest frequency response and β is used to damp out the highest frequency. The β coefficient is characteristic of the acoustic wave propagation which, in a piezoelectric material, requires the knowledge of the material stiffness, piezoelectric and dielectric constants and attenuation data [122]. In the study, attenuation of AlN is approximated with the assumption that it is comparable to silicon and the calculated value of β is $2.82e^{-14}$ where a = 6.5 dB/cm. In [140] , the value of a used is 8 dB/cm at 1 GHz.

A more accurate value of the material damping coefficient needs to be estimated to obtain more precise results. In [122] , the MEMS trampoline resonators were designed, in which the AlN is directly deposited on the Si substrate. However, in this present work, the AlN is deposited on the electrode layer on the Si substrate. Therefore, it is believed that the assumption made in [122] is not applicable to this current research. The next sub-section will discuss in detail the method for obtaining the value of material damping coefficients.

3.3.5.4 Estimation of Material Damping Coefficients

As mentioned in Chapter 2, a few approximations can be applied in order to estimate the attenuation, a in piezoelectric material. Thermoelastic attenuation and Akhieser attenuation are the most important as both produce attenuation, which increases with the square of frequency [120]. Therefore, in this study, only thermoelastic attenuation and Akhieser attenuation are considered. As explained in Chapter 2, thermoelastic attenuation is related to the irreversible heat conduction from the contracted area of a longitudinal wave to the extended area. Meanwhile, Akhieser attenuation is a result of a change in the phonon group velocities through the anharmonic of the lattice due to a strain wave (either longitudinal or transverse) which propagates through a crystal. The thermoelastic damping (TED) contributes only around 5% of the overall losses [120]. This is because TED becomes less relevant when the thickness of the piezoelectric layer is reduced [32].

As the TED can be computed directly in the simulation, only Akhieser attenuation is used to calculate the a. The approximation of a by using this method is as given in the equation 2.4 where γ is the Gruneisen constant (γ

=1.2), K is the lattice thermal conductivity (1.6 cal/cm °C sec) , T' is the absolute temperature (300 K), ρ is the mass density (3.26 gm/cm^3) and υ is the velocity of longitudinal sound (10400 m/s). The previous sub-section explained the definition of β. In [122], the one-dimensional viscoelastic wave equation was used to yield the value of β. The β can be computed using equation 2.12 where λ_1 is the value of attenuation in Nepers/m where 1 N=8.686 dB, Y (C_{33}) is the elastic stiffness (395 GPa) and ρ is the density (3260 kg/m^3).

3.4 Theory of FBAR Filter

3.4.1 Working Principle of Ladder-Type FBAR Filter

The ladder-type FBAR filter is modelled by the nth order interconnection of series- and shunt-connected FBARs, as depicted in Figure 3.9. The total number of resonators matches the order (N) of the filter. The working principle of a one-stage (N=2) ladder-type filter can be explained by examining one of its L-section. An L-section is composed of two resonators, one connected in series and the other connected in shunt. The resonator has two resonant frequencies, which are series resonant frequency (f_s) and parallel resonant frequency (f_p). At f_s, the electrical impedance is minimum (Z_{min}) and at f_p, the electrical impedance is maximum (Z_{max}). The electrical impedance has the characteristics of static capacitance (C_o) at frequencies far from f_s or f_p.

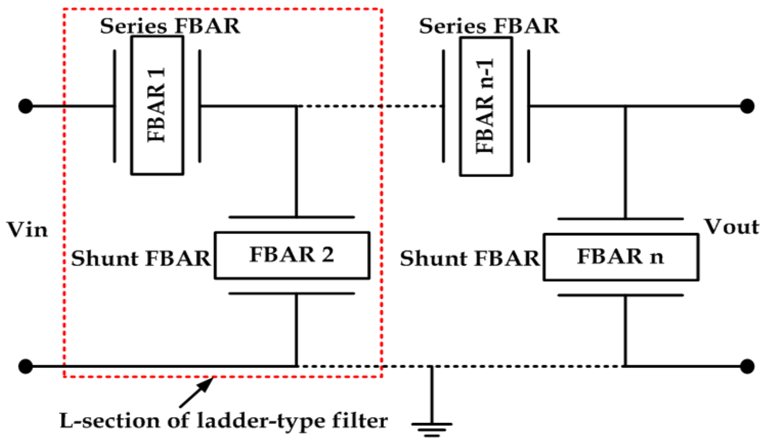

Figure 3.9 n^{th} Order of Ladder-Type FBAR Filter

The series resonant of the shunt resonator (f_s^p) is tuned to be lower than the resonant of the series resonator (f_s^s), as shown in Figure 3.10. The continuous line represents the typical transmission response of ladder filters, while the dashed and dotted line characterise the electrical impedance of the series (Z_s) and parallel (Z_p) resonators, respectively. A passband is formed at frequencies near the f_s^s and f_p^p where there is a low impedance between the input and output terminals of the L-section and high impedance between the output terminal and ground. At f_s^p, any current flowing into the L-section is shortened to ground by the low impedance of the shunt resonator, thus a zero occurs in the transmission response below the passband. At f_p^s, the high impedance between the input and output of the L-section coincide with another zero in the transmission response above the passband. At frequencies far from the resonant and anti-resonant frequencies, the L-section acts as a two-capacitor network with broadband transmission characteristics [141]. The ladder-type filter gives a steep roll-off but a poor out-of-band (*OoB*) rejection characteristic. A better *OoB* can be achieved by cascading more L-section of the filter as shown in Figure 3.9; however, this will need to trade-off with the insertion loss (I_L).

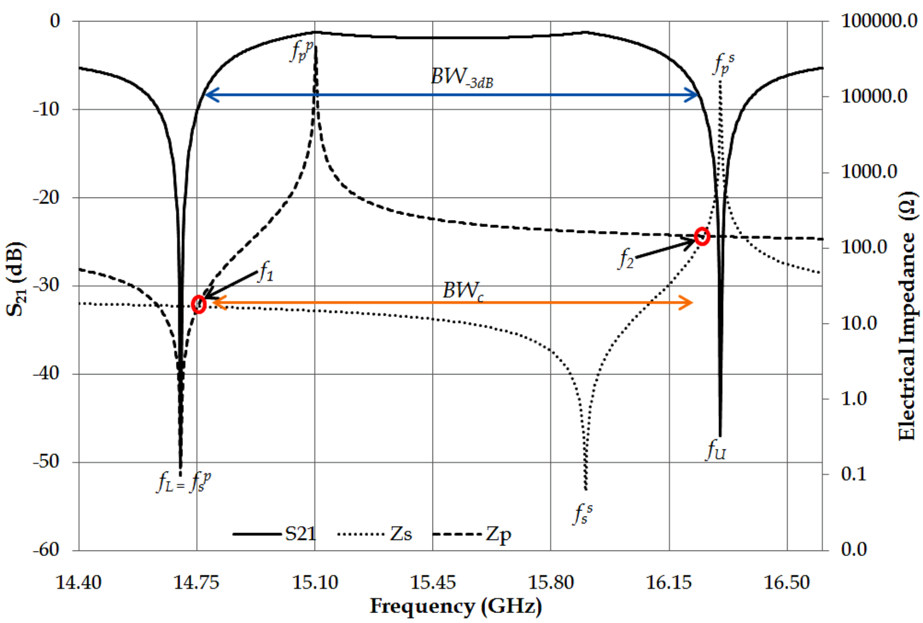

Figure 3.10 Working Principle and Design Parameters of a Ladder-Type FBAR Filter

3.4.2 Design Methodology

A collection of closed-form expressions for the systematic design procedure of ladder-type FBAR filters as given in [94] are used in this research. Then, the transmission *ABCD* matrix [126] is applied to calculate the S-parameters.

3.4.2.1 Closed-form expression

The design of a ladder-type FBAR filters consists of determining the order of the filter, which is equal to the number of resonators (N) and characterising the f_s and f_p from the filter specifications. A series FBAR is characterised by f_p^s, electromechanical coefficient (k_t^s) and C_o^s whereas a parallel FBAR is characterised by f_p^s, k_t^p and C_o^p. Since both k_t^s and k_t^p essentially depend on the piezoelectric material used, they will not be considered as a design parameter and it will be assumed that

$$k_t = k_t^s = k_t^p \qquad 3.39$$

In this case, the filter will be characterised by the bandwidth, the *OoB* rejection and the frequency allocation of the upper transmission zeros (f_U) and lower transmission zeros (f_L), as shown in Figure 3.10. It is important to point out that it is not necessary to specify the centre frequency (f_c) since equation 3.32 and the design procedure guarantee that $f_c^2 = f_U\, f_L$. The filter bandwidth is defined as $BW_c = f_2 - f_1$, where f_1 and f_2 are the frequencies where $|Z_s(f_i)| = |Z_p(f_i)|$ (i=1, 2). This definition makes BW_c slightly smaller than the bandwidth at -3dB (BW_{-3dB}), but now BW_c is independent of the number of resonators, simplifying significantly the design equations. Figure 3.11 shows the flowchart of the design procedure, followed by a detailed explanation of each step of the design procedure.

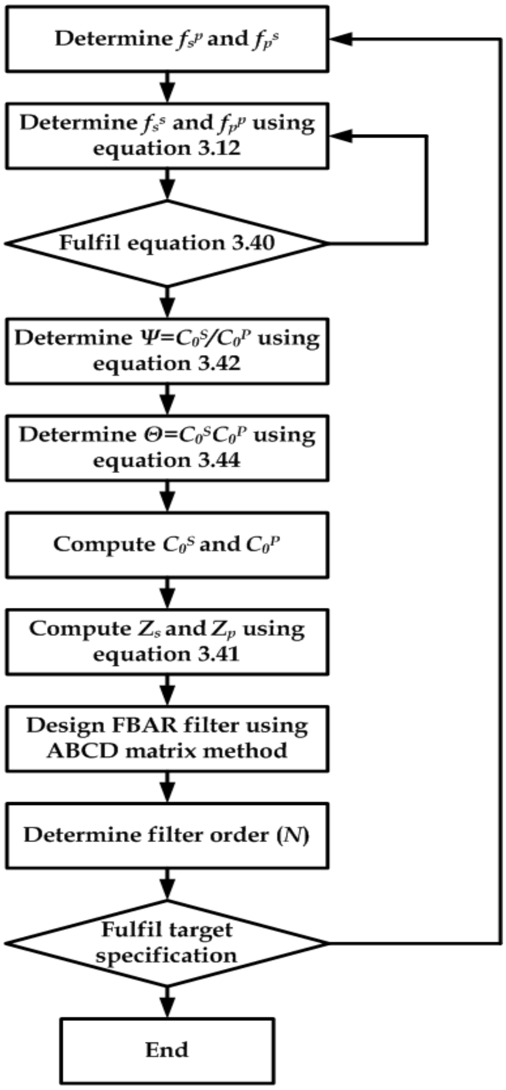

Figure 3.11 Flowchart of the Design Procedure

1) Determine f_s^p and f_p^s.

As shown in Figure 3.10, in this design, f_0^U will be matched to f_p^s, and f_0^U will be matched to f_s^p.

2) Determine f_p^p and f_s^s.

For a given k^2_t using equation 3.12, practical bandwidths are only obtained if $f_s^s \geq f_p^p$. Hence, the design is restricted to those filters whose upper and lower transmission zeroes fulfil

$$f_U \geq \left(\frac{\pi^2}{4k_t^2}\right)\left(\frac{\pi - \sqrt{\pi^2 - 16k_t^2}}{\pi + \sqrt{\pi^2 - 16k_t^2}}\right) f_L \qquad 3.40$$

3) Determine $\Psi = C_o^s / C_o^p$.

By using the definition of BW_c previously described together with equation 3.23, it can be shown that BW_c depends on f_s^p, f_p^p, f_s^s, f_p^s and Ψ. Since all the resonance frequencies have been already determined, then Ψ is chosen to achieve the specified BW_c. By using equation 3.16, it is a complex task to obtain a closed-form expression of Ψ as a function of BW_c. In order to overcome this difficulty, instead of using equation 3.16, the next approximation of electrical impedance for the frequencies close to the resonance is used as in equation 3.41.

$$Z(f) = \frac{1}{j2\pi f C_0}\left(\frac{f^2 - f_s^2}{f^2 - f_p^2}\right) \qquad 3.41$$

resulting in

$$\psi = \frac{-f_i^4 + f_i^2 f_p^{p^2} + f_i^2 f_s^{s^2} - f_s^{s^2} f_p^{p^2}}{f_i^4 - f_i^2 f_p^{s^2} - f_i^2 f_s^{p^2} + f_p^{s^2} f_s^{p^2}} \qquad 3.42$$

where f_i can be either f_1 or f_2. In order to obtain a closed-form expression of ψ as a function of BW_c, an approximation that f_1 and f_2 are symmetrically spaced around the f_c, and therefore $f_1 = f_c - BW_c/2$ and $f_2 = f_c + BW_c/2$. By using the approximation in equation 3.42, it can be seen that Ψ increases with BW_c. This fact will have a negative effect on *OoB* rejection, as will be seen further on. It is important to point out that some BW_c can imply $\Psi<0$, which is not physically possible. For this reason, the specified BWc must fulfil

$$f_c - f_p^p < \frac{BW_c}{2} < f_c - f_s^p \qquad 3.43$$

4) Determine $\Theta = C_o^s C_o^p$.

Parameter Θ is related to the image impedance matching condition of the input and output ports of one stage, and can be given by [126]

$$\Theta = \frac{1}{(2\pi f_c R)^2} \qquad 3.44$$

where R = 50 Ω is the impedance of the source and the load.

5) Compute C_o^s and C_o^p.

C_o^s and C_o^p can be calculated by solving equations 3.42 and 3.44 for C_o^s and C_o^p.

6) Determine *N*.

The ladder-type filter behaves as an *OoB* ladder of capacitances. *OoB* rejection is defined as the maximum value of the transmission spectrum outside the passband minus the insertion loss. In this band, the rejection decreases slowly as the frequency moves away from f_c as it can be seen in Figure 3.10. The lowest level of attenuation achievable only depends on N and Ψ as shown in Figure 3.12 [94]. This rejection represents the lowest level of attenuation achievable out-of-band. Since Ψ has been already determined, the order N of the filter will be chosen to achieve the specified *OoB* rejection. It can be observed that for a given Ψ, an increase in N entails an *OoB* rejection improvement, as mentioned previously. On the other hand, for a given N, an increase in BW_c, which also entails an increase in Ψ, degrades the *OoB* rejection.

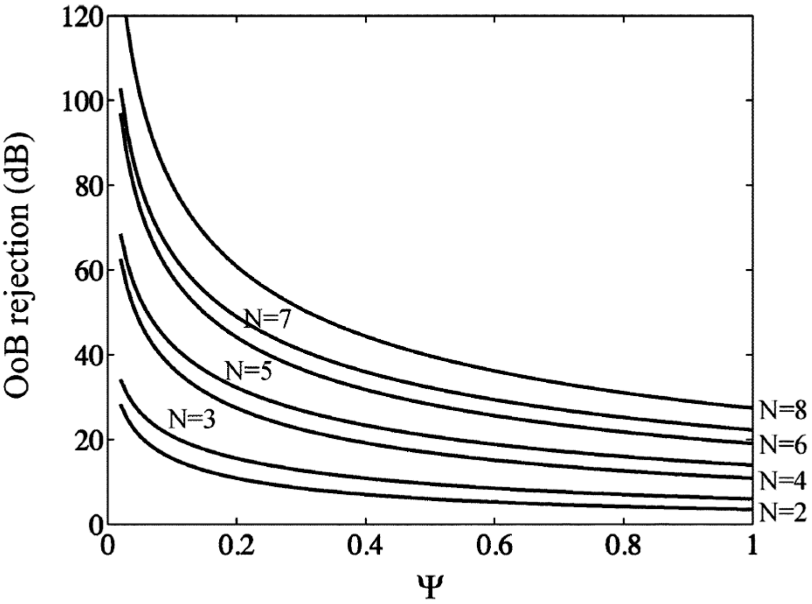

Figure 3.12 Out-of-band (*OoB*) Rejection as A Function of *Ψ* for Different *N* [94]

3.4.2.2 The Transmission (*A B C D*) Matrix

A ladder-type FBAR filter can be described by 2x2 transmission or transmission *ABCD* matrix for each two-port network within the filter. The *ABCD* matrix of a two-port single resonator is given by [63, 126]:

$$M = \begin{bmatrix} A & B \\ C & D \end{bmatrix} \tag{3.45}$$

The chain matrix:

$$M_s = \begin{bmatrix} 1 & Z_1 \\ 0 & 1 \end{bmatrix} \quad \text{and} \quad M_p = \begin{bmatrix} 1 & 0 \\ Y_2 & 1 \end{bmatrix} \tag{3.46}$$

where M_s and M_p are *ABCD* matrices of the series and shunt FBAR, respectively. Z_1 is the electrical impedance of the series FBAR and Y_2 is the admittance of the shunt FBAR, where Y_2 is the inverse of the impedance $Y_2=1/Z_2$. The *ABCD* matrix of the cascade connection of two or more two-port networks can be easily obtained by multiplying the *ABCD* matrices of the individual two-port network as shown below:

$$M = \begin{bmatrix} A & B \\ C & D \end{bmatrix} = M_s \cdot M_p \cdot M_s \cdots \qquad 3.47$$

From the concept of the image parameter method [142], as shown in Figure 3.13, by using the network synthesis, the discrete impedance elements Z_1, Z_2 and Z_3 can be used to obtain the transfer function of a network.

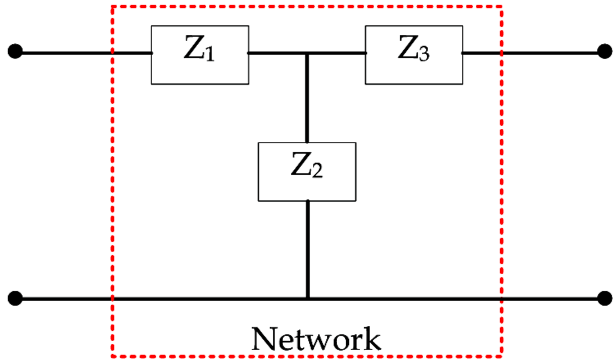

Figure 3.13 The Discrete Impedance Element Z_1, Z_2 and Z_3

The ladder-type filters consisting of discrete impedance elements in the series and shunt can be expressed in terms of the *ABCD* matrix parameters of the network. Then, the matrix parameters for various orders of filters can be obtained as given in the equations:

2nd order:

$$\begin{bmatrix} 1 + Z_1/Z_2 & Z_1 \\ 1/Z_1 & 1 \end{bmatrix} \qquad 3.48$$

3rd order:

$$\begin{bmatrix} 1+Z_1/Z_2 & 2Z_1+Z_1^2/Z_2 \\ 1/Z_1 & Z_1/Z_2+1 \end{bmatrix} \tag{3.49}$$

4th order:

$$\begin{bmatrix} 1+3(Z_1/Z_2)+(Z_1/Z_2)^2 & 2Z_1+Z_1^2/Z_2 \\ 2/Z_2+Z_1/Z_2^2 & Z_1/Z_2+1 \end{bmatrix} \tag{3.50}$$

5th order:

$$\begin{bmatrix} 1+3(Z_1/Z_2)+(Z_1/Z_2)^2 & 3Z_1+4(Z_1/Z_2)^2+Z_1^3/Z_2^2 \\ 2/Z_2+Z_1/Z_2^2 & 1+3(Z_1/Z_2)+(Z_1/Z_2)^2 \end{bmatrix} \tag{3.51}$$

6th order:

$$\begin{bmatrix} 1+6(Z_1/Z_2)+5(Z_1/Z_2)^2 & 3Z_1+4(Z_1/Z_2)^2+Z_1^3/Z_2^2 \\ 3/Z_2+4Z_1/Z_2^2+Z_1^2/Z_2^3 & 1+3(Z_1/Z_2)+(Z_1/Z_2)^2 \end{bmatrix} \tag{3.52}$$

7th order:

$$\begin{bmatrix} 1+6(Z_1/Z_2)+5(Z_1/Z_2)^2+Z_1^3/Z_2^3 & 4Z_1+10(Z_1^2/Z_2)+6(Z_1/Z_2)^2+(Z_1/Z_2)^3 \\ 3/Z_2+4Z_1/Z_2^2+Z_1^2/Z_2^3 & 1+5(Z_1/Z_2)+3(Z_1/Z_2)^2+(Z_1/Z_2)^3 \end{bmatrix} \tag{3.53}$$

8th order:

$$\begin{bmatrix} 1+6(Z_1/Z_2)+5(Z_1/Z_2)^2+Z_1^3/Z_2^3 & 4Z_1+10(Z_1^2/Z_2)+6(Z_1/Z_2)^2+(Z_1/Z_2)^3 \\ 4/Z_2+7Z_1/Z_2^2+2(Z_1^2/Z_2^3) & 1+5(Z_1/Z_2)+3(Z_1/Z_2)^2+(Z_1/Z_2)^3 \end{bmatrix} \tag{3.54}$$

The S-parameters of the circuit can be extracted from the *ABCD* matrix given as:

$$S_{11}=\frac{A+B/Z_0-CZ_0-D}{A+B/Z_0+CZ_0+D} \tag{3.55}$$

$$S_{12} = \frac{2(AD - BC)}{A + B/Z_0 + CZ_0 + D} \qquad 3.56$$

$$S_{21} = \frac{2}{A + B/Z_0 + CZ_0 + D} \qquad 3.57$$

$$S_{22} = \frac{-A + B/Z_0 - CZ_0 + D}{A + B/Z_0 + CZ_0 + D} \qquad 3.58$$

where Z_0 is the source impedance, 50 Ω.

The S-parameters can be transferred to Z-parameters given as:

$$Z_{11} = \frac{(1 + S_{11})(1 - S_{22}) + S_{12}S_{21}}{(1 - S_{11})(1 - S_{22}) - S_{12}S_{21}} \qquad 3.59$$

$$Z_{12} = \frac{2S_{12}}{(1 - S_{11})(1 - S_{22}) - S_{12}S_{21}} \qquad 3.60$$

$$Z_{21} = Z_0 \frac{2S_{12}}{(1 - S_{11})(1 - S_{22}) - S_{12}S_{21}} \qquad 3.61$$

$$Z_{11} = Z_0 \frac{(1 - S_{11})(1 - S_{22}) + S_{12}S_{21}}{(1 - S_{11})(1 - S_{22}) - S_{12}S_{21}} \qquad 3.62$$

From the S-parameters, various electrical loss parameters are calculated using the equations given in [119]:

Insertion loss:

$$I_L = -10 \log_{10} \frac{|S_{21}|^2}{1 - |S_{11}|^2} dB \qquad 3.63$$

Input return loss:

$$RL_{in} = |20 \log_{10} |S_{11}|| dB \qquad 3.64$$

Reverse isolation:

$$I_{rev} = \left|20\log_{10}\left|S_{12}\right|\right| dB \qquad 3.65$$

Output return loss:

$$RL_{out} = \left|20\log_{10}\left|S_{22}\right|\right| dB \qquad 3.66$$

3.5 Conclusion

This chapter presented the theory of FBARs, such as the piezoelectric and acoustic propagation theory and the important characteristics such as the Q factor and k^2_{eff}. A detailed discussion on the design methodology of FBARs and FBAR filters using 1-D and 3-D FEM was presented. This chapter also presented the theory of ladder-type film bulk acoustic wave resonator (FBAR) filters. The theory and important characteristics of the filter, such as insertion loss, out-of-band rejection, and bandwidth were discussed for further use in FBAR filter design that will be explained in the next chapter. The detailed discussions on the major losses from piezoelectric material such as thermoelastic damping and material damping discussed in this chapter will be used to characterise the FBAR filters designed in the next chapter.

CHAPTER 4 : DESIGN AND ANALYSIS OF KU-BAND FBAR FILTERS

4.1 Introduction

Chapter 3 presents the modelling and design procedures of designing a film bulk acoustic wave resonator (FBAR), and a ladder-type filter based on FBARs. This chapter describes the design and analysis of Ku-band FBAR filters using the closed-form expressions as illustrated in Chapter 3. A detailed discussion on the effects of various FBAR design parameters is also presented in this chapter and the effects of filter order (*N*) on the out-of-band (*OoB*) rejection, and the filter characteristics are discussed. Finally, the characteristics of the designed FBAR are determined using the Butterworth Van Dyke (BVD) model.

4.2 Design of the Ku-band FBAR Filter

The target specifications for the Ku-band FBAR filter used in this work are based on the specifications set out in Table 2.3. Together with other FBAR filter characteristics obtained from the literature [4, 79, 81], the target specifications of the Ku-band FBAR filter are defined and presented in Table 4.1.

Table 4.1 Target Specification of Ku-band FBAR Filter

Specification	Value
Insertion loss	~ -3.0 dB
OoB rejection	~ -12.0 dB
Centre Frequency	~15.5 GHz
Bandwidth	~1.0 GHz

4.2.1 Design Procedure for FBAR Filter

An FBAR filter consists of with at least two FBARs [93]. Based on the specifications in Table 4.1, two FBARs, the series FBAR and shunt FBAR are designed to achieve the target. The passband at BW_{-3dB} is targeted to be 1 GHz from 15 GHz to 16 GHz. The following design steps are followed to design an FBAR filter.

Step 1: Determine f_1 and f_2.

f_1 and f_2 are calculated using the approximation given in Chapter 3 where $f_1 = f_c - BW_c/2$ and $f_2 = f_c + BW_c/2$. As the f_c is chosen to be 15.5 GHz, thus, f_1 and f_2 are calculated to be 15.0 GHz and 16.0 GHz respectively.

Step 2: Determine f_L and f_U.

As shown in Figure 3.10, $f_L = f_s^p$ and $f_U = f_p^s$. f_L is selected to be 300 MHz less than f_1 and f_U is chosen to be 300 MHz higher than f_2. Therefore, f_L is set to 14.7 GHz while f_U is set to 16.3 GHz. The design of the filter is limited by the condition in equation 4.1.

$$f_U \geq \left(\frac{\pi^2}{4k_{eff}^2}\right)\left(\frac{\pi - \sqrt{\pi^2 - 16k_{eff}^2}}{\pi + \sqrt{\pi^2 - 16k_{eff}^2}}\right) f_L \qquad 4.1$$

300 MHz is a chosen offset value of this design example. Further optimisation will be needed to fine-tune this offset value and will be required to achieve the target filter specifications.

Step 3: Determine f_p^p and f_s^s.

Another consideration is that the value of k^2_{eff} must be lower than the maximum achievable value with the used materials. As stated in the literature, k^2_{eff} of AlN ranges from 6.0% to 7.0% [72]. This is important when setting up the values of f_s^s, f_s^p, f_p^s and f_p^p to ensure a valid k^2_{eff} is achieved. Instead of calculating f_p^p and f_s^s using equation 4.2, f_p^p and f_s^s are set first, and then these values are verified using the equation to verify whether they fulfil the requirement. f_p^p is set 15.1

GHz and f_s^s is set to 15.9 GHz as these values have been verified and they fulfil the required condition. The k^2_{eff} is calculated to be 6.05% and k^2_{eff} is 6.54% using the following equation:

$$k_{eff}^2 = \left(\frac{\pi^2}{4}\right)\left(\frac{f_p - f_s}{f_p}\right) \qquad 4.2$$

Step 4: Determine $\Psi = C_o^s/C_o^p$.

When specifying the BW_c in step 1, it is important to fulfil the requirement in equation 4.3. This is to make sure a reasonable value of Ψ will be achieved as some BW_c can entail Ψ<0.

$$f_c - f_p^p < \frac{BW_c}{2} < f_c - f_s^p \qquad 4.3$$

$$\psi = \frac{-f_i^4 + f_i^2 f_p^{p^2} + f_i^2 f_s^{s^2} - f_s^{s^2} f_p^{p^2}}{f_i^4 - f_i^2 f_p^{s^2} - f_i^2 f_s^{p^2} + f_p^{s^2} f_s^{p^2}} \qquad 4.4$$

The value of Ψ is calculated using equation 4.4 and is equal to 0.23.

Step 5: Determine $\Theta = C_o^s\, C_o^p$.

The parameter Θ is related to the impedance matching condition and calculated using equation 3.44. For f_c=15.5 GHz and R=50 Ω, the value of Θ is computed to be 4.2173e^{-26}.

Step 6: Determine C_o^s and C_o^p.

The values of C_o^s and C_o^p are calculated directly from step 3 and 4. The values of C_o^s and C_o^p obtained are 0.0987 pF and 0.4274 pF respectively.

Step 7: Determine Z_s and Z_p.

Using the C_o^s and C_o^p obtained, the electrical impedance for the series FBAR (Z_s) and the shunt FBAR (Z_p) are computed as in equation 4.5 using MATLAB scripts (see Appendix A).

$$Z(f) = \frac{1}{j2\pi f C_0}\left(\frac{f^2 - f_s^2}{f^2 - f_p^2}\right) \qquad 4.5$$

As mentioned in Chapter 3, from the electrical impedance graphs, the approximation given is f_1 and f_2 are the frequencies where $|Z_s(f_i)|$ is equal to $|Z_p(f_i)|$ where (i=1, 2) as shown in Figure 4.1. The f_1 and f_2 obtained from step 1 are compared with f_1 and f_2 obtained from this approximation. From the graph, the values of f_1 and f_2 are 14.99 GHz and 15.98 GHz respectively. These values are close to the values used in step 1.

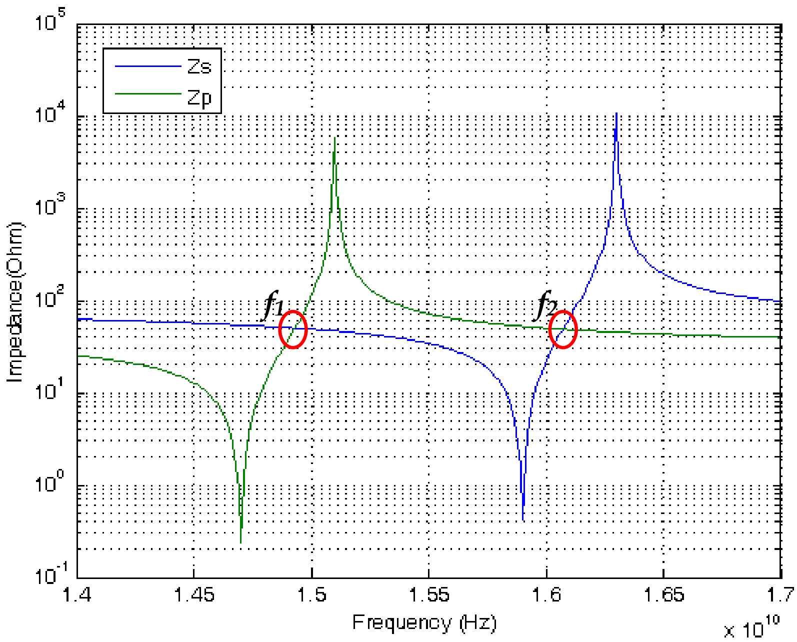

Figure 4.1 Electrical Impedance of Series and Shunt FBARs

Step 8: Determine *N*.

By using the Z_s and Z_p obtained, the transmission *ABCD* matrix method is used to design the second-order FBAR filter using equation 3.48. Then, the S-parameters (S_{11}, S_{12}, S_{21} and S_{22}) of the FBAR filter are determined using equations 3.55 to 3.58. Then, the I_L is computed using equation 3.63. Other filter characteristics such as *OoB* and BW_{-3dB} were also analysed. *OoB* was defined as the maximum value of the transmission response minus the insertion loss [66].

Table 4.2 shows the characteristics of the FBAR filter at second, third and fourth order. The results show that the calculated values of I_L are too high and the BW_{-3dB} is only between 10 MHz to 30 MHz, which is too narrow. However, the *OoB* obtained is within the target specifications. The data further show that the filter order has a significant effect on the I_L, *OoB* and BW_{-3dB}. Even though the *OoB* improved with the increasing of filter order, this degraded the I_L and BW_{-3dB}. The results displayed in Figure 4.2 show the presence of the 'mid-band dip'. This is mainly due to the wide gap between the f_p^p and f_s^s of the FBARs. Further analysis of the design parameters that affect the performance of the filter will be discussed in the next section.

Table 4.2 Characteristics of FBAR Filter

Filter A	***N*=2**	***N*=3**	***N*=4**
BW_{-3dB} (GHz)	0.03	0.02	0.01
I_L (dB)	-5.04	-5.29	-8.76
OoB (dB)	-12.23	-19.74	-27.40

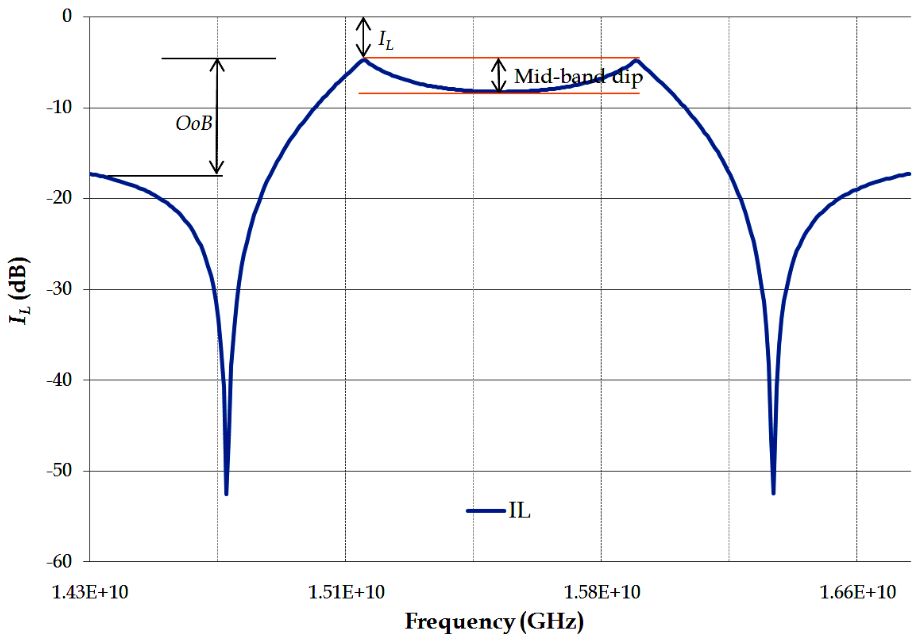

Figure 4.2 Transmission Response of the 2nd Order FBAR Filter.

4.3 Analysis of Design Parameters

In order to achieve the required specification of the FBAR filter, various investigations of parameters that affect the characteristics of the filters were carried out. Detailed investigations on the effects of various FBAR design parameters including the f_s^s, f_s^p, f_p^s, f_p^p, f_1 and f_2 and the effects of filter order (N) on the out-of-band (OoB) rejection, and the filter characteristics are described in the following sub-sections. The design procedures presented in section 4.2 is repeated for each of the FBAR filters designed for analysis purposes.

4.3.1 Effect of Varying f_s^s, f_s^p, f_p^s and f_p^p

Five different filters are designed to investigate the effect of varying f_s^s while other parameters are constant. The obtained results are presented as a dashed line in Figure 4.3. Firstly, the value of f_p^p is kept constant to 15.2 GHz; while f_s^s is varied from 15.5 GHz to 15.9 GHz in 100 MHz steps. The results indicate that as $f_s^s - f_p^p$ decreases, the second order BW_{-3dB} also decreases. However, it is observed that I_L and OoB are inversely proportional to $f_s^s - f_p^p$.

Secondly, the value of f_s^s is kept constant at 15.2 GHz; while f_p^p varies from 15.5 GHz to 15.9 GHz in 100 MHz steps. The results achieved are depicted as a dotted line in Figure 4.3. It can be seen that as f_s^s – f_p^p decreases, BW_{-3dB} decreases. It is also observed that *OoB* improves, while I_L degrades as BW_{-3dB} decreases.

Then, the effect of varying both f_s^s and f_p^p while other parameters are constant is shown as a continuous line in Figure 4.3. It shows that as f_s^s – f_p^p decreases, BW_{-3dB} also decreases. I_L improves significantly as BW_{-3dB} decreases. On the other hand, *OoB* degrades as BW_{-3dB} decreases.

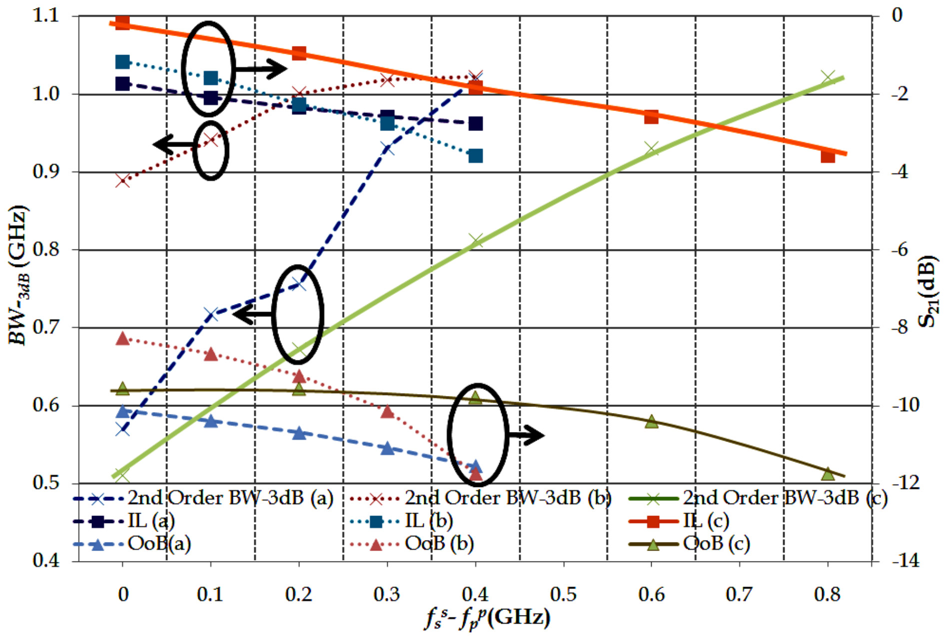

Figure 4.3 Effect of Varying f_s^s f_s^p, f_p^s and f_p^p

Based on the analysis described in this section, varying the values of f_s^s, f_s^p, f_p^s and f_p^p will directly affect the filter characteristics. From Figure 4.3, it was observed that BW_{-3dB} and *OoB* gradually decrease as the difference between f_s^s and f_p^p decreases. On the other hand, I_L improves as f_s^s and f_p^p decrease.

4.3.2 Effect of f_1 and f_2

The effect of f_1 and f_2 on filter characteristics is shown in Figure 4.4. Five different filters are designed to investigate the effect. The bandwidth of each FBAR is set to 500 MHz and the difference between f_s^s and f_p^p is set to 600 MHz. Second order filter characteristics are used for comparison purposes. From Figure 4.4, it is observed that as BW_c increases, BW_{-3dB} increases too. It was also observed that insertion loss (I_L) has no significant change, whereas OoB rejection decreases significantly after BW_c reaches 1.0 GHz and then remains constant. From this observation, we can conclude that to obtain wider BW_{-3dB}, $f_2 - f_1$ (BW_c) should be increased to the required value that is higher than 1 GHz.

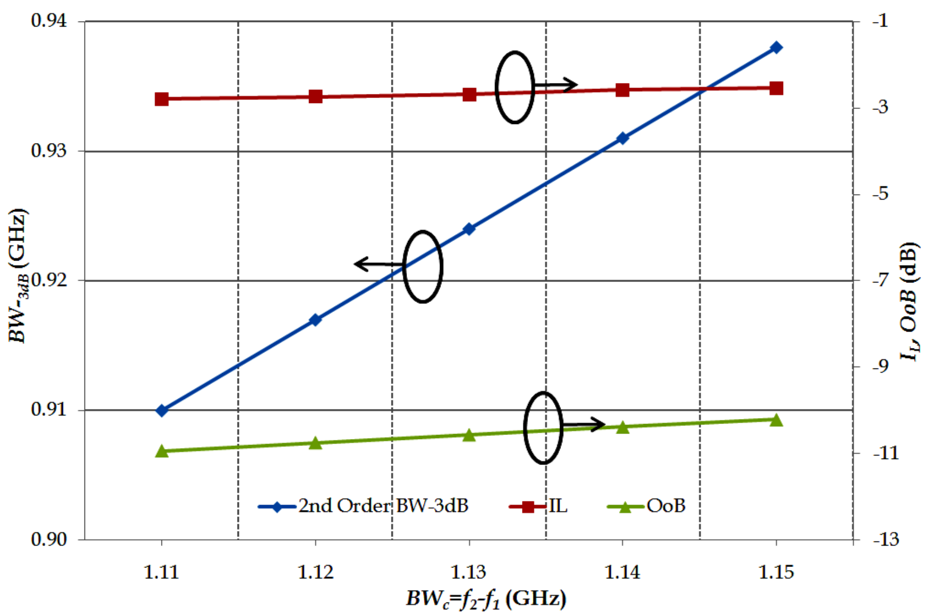

Figure 4.4 Effect of Varying f_1 and f_2

Figure 4.5 shows another important parameter, Ψ that has a major effect on the variation of f_1 and f_2 values. It is observed that as Ψ increases, BW_{-3dB} increases while OoB degrades.

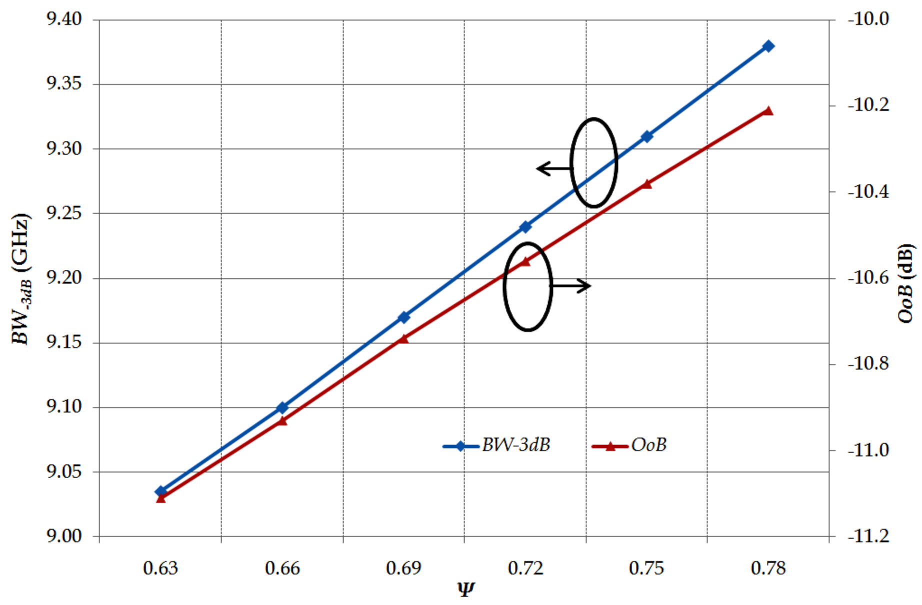

Figure 4.5 Effect of Ψ on BW_{-3dB} and OoB

As mentioned previously, the occurrence of the 'mid-band dip' at the centre is due to the increasing gap between f_s^s and f_p^p of the FBARs. One of the purposes of this analysis is to investigate and find ways to minimise the 'mid-band dip'. Based on Figure 4.5, the value of Ψ is set to more than 1, in order to achieve BW_{-3dB} of at least 1 GHz. Therefore, for the purpose of this analysis, eleven different filters are designed with Ψ ranging from 1.2 to 11.2. Figure 4.6 presents the comparison of the transmission response (S_{21}) of some of the filters designed for this analysis. The filters have the same values of f_s^s, f_s^p, f_p^s and f_p^p but different values of f_1 and f_2. Filter 1 has $BW_c = f_2 - f_1$ of 1.30 GHz with Ψ=1.2, Filter 2 has $BW_c = f_2 - f_1$ of 1.50 GHz with Ψ=5.2 and Filter 3 has BW_c of 1.55 GHz with Ψ=11.2. It is observed that the 'mid-band dip' presents in Filter 1. Meanwhile, it can be seen that for Filter 2 and Filter 3, the 'mid-band dip' is less than -3 dB and the achieved BW_{-3dB} for the filters are 1.02 GHz and 1.10 GHz, respectively. It also can be observed that the value of Ψ has a significant effect on the 'mid-band dip'. The 'mid-band dip' reduces as Ψ increases. In light of this analysis, the FBAR filter design parameters listed in Table 4.3 have been chosen.

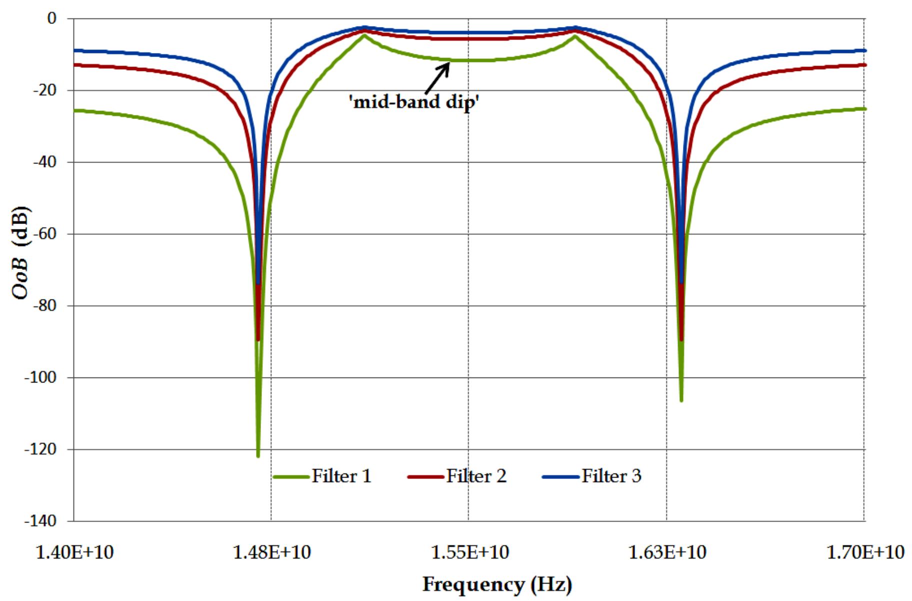

Figure 4.6 Comparison of Transmission Response (S_{21}) of 6th Order of Filter 1, Filter 2 and Filter 3

Table 4.3 Design Parameters of FBAR Filters

Parameter	f_1**(GHz)**	f_2**(GHz)**	f_s^s**(GHz)**	f_p^s**(GHz)**	f_s^p**(GHz)**	f_p^p**(GHz)**	Ψ
Filter A	14.725	16.275	15.90	16.30	14.70	15.10	11.2
Filter B	14.75	16.25	15.90	16.30	14.70	15.10	5.2

4.3.3 The effect of *N*

The *OoB* of the FBAR filter is only dependent on Ψ and *N*. The relationship between *OoB*, Ψ and *N* is shown in Figure 4.7. It can be observed that an increase in Ψ will degrade *OoB*. As Ψ is already determined a priori, *N* is then chosen to achieve the required BW_{-3dB}. The effect of *N* on the filter characteristics of Filter A and B is presented in Figure 4.8. BW_{-3dB} and I_L decrease gradually as *N* increases. At the same time, *OoB* steadily improves as *N* increases. From this analysis, it is noticeable that even though increasing the filter order will improve *OoB*, it will however degrade I_L and BW_{-3dB} of the filter. The higher filter order requires more resonators, which will result in increased size and cost. Hence, the optimum value of filter order is selected to be 8th and

6th for Filter A and Filter B, respectively. Both filters fulfil the target specifications where the 8th order Filter A has a bandwidth of 1.05 GHz, I_L of –3.23 dB and *OoB* rejection of -11.83 dB. Meanwhile, the 6th order Filter B has a bandwidth of 1.03 GHz, I_L of –3.52 dB and *OoB* rejection of -12.88 dB.

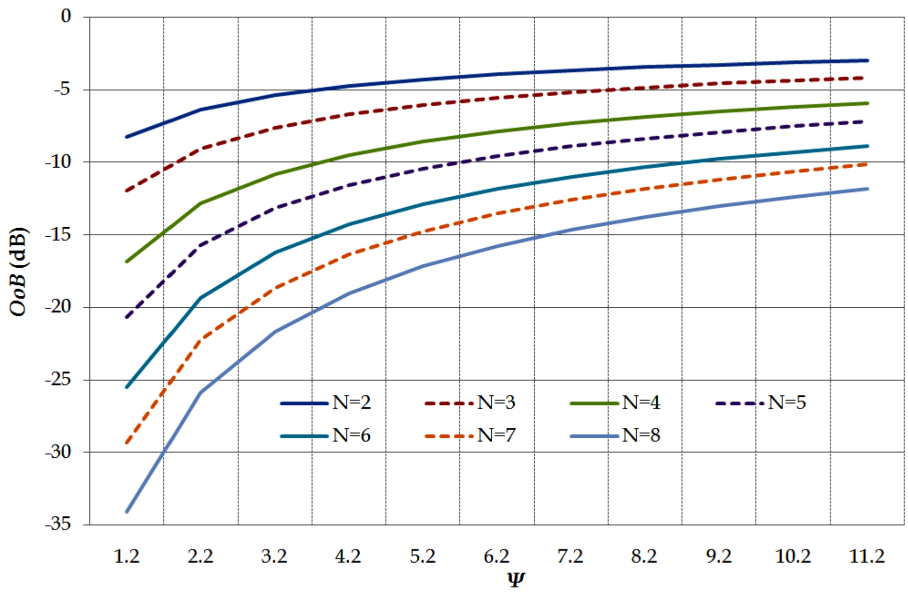

Figure 4.7 *OoB* as A Function of ψ and N

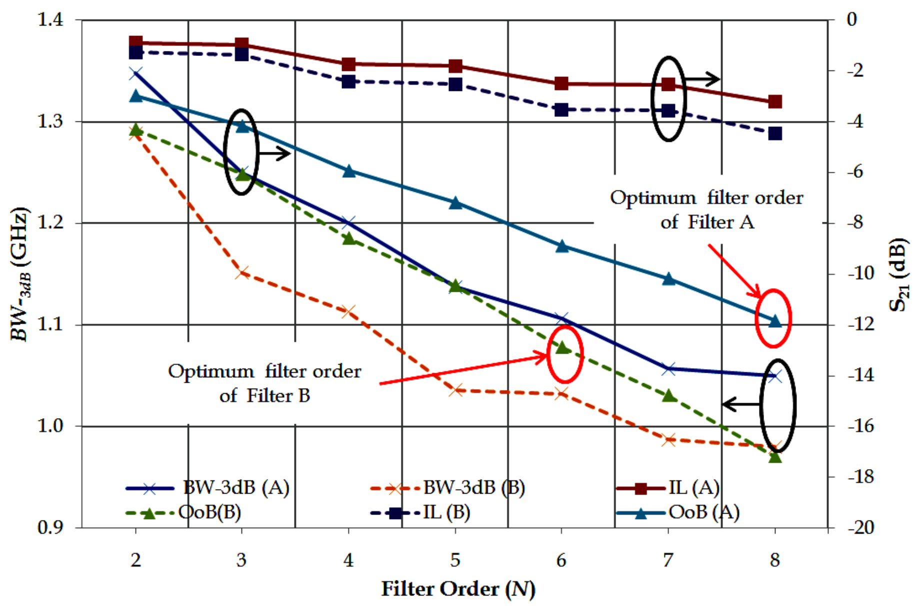

Figure 4.8 Effect of Filter Order (N)

4.4 Results and Discussion

The analysis presented in this chapter outlines the design of FBAR filters with 1.0 GHz bandwidth operating at 15.5 GHz. The parameters used in designing the filter are presented in Table 4.3. The characteristics of each filter are summarised and compared in Table 4.4. It is observed that Filter A has the advantage of wider bandwidth and better insertion loss compared to Filter B. However, Filter A has slightly higher *OoB* rejection than Filter B. The analyses suggest that the FBAR filter with wider bandwidth will degrade the *OoB* rejection of the filter, even though insertion loss is improved.

Table 4.4 Characteristics of Ku-band FBAR Filters

Filter A	***N*=2**	***N*=3**	***N*=4**	***N*=5**	***N*=6**	***N*=7**	***N*=8**
BW_{-3dB} (GHz)	1.35	1.25	1.20	1.14	1.11	1.06	1.05
I_L (dB)	-0.90	-0.96	-1.73	-1.80	-2.50	-2.54	-3.23
OoB (dB)	-2.97	-4.17	-5.93	-7.18	-8.88	-10.16	-11.83
Filter B	***N*=2**	***N*=3**	***N*=4**	***N*=5**	***N*=6**	***N*=7**	***N*=8**
BW_{-3dB} (GHz)	1.29	1.15	1.11	1.04	1.03	0.99	0.98
I_L (dB)	-1.27	-1.36	-2.41	-2.52	-3.52	-3.57	-4.46
OoB (dB)	-4.29	-6.07	-8.58	-10.44	-12.88	-14.77	-17.18

Table 4.5 shows a comparison of FBAR filters operating in X-band to Ka band. All the filters were designed in a 4-stage ladder filter that is equal to an 8th order filter. The 8th order FBAR Filter A and the 6th order FBAR Filter B are chosen as the best filter characteristics from this work for comparison. The present data show that FBAR filters have better performance than reported in [79] where the insertion loss is too high and the bandwidth is only 0.28 GHz. To the best of the author's knowledge, this is the first FBAR filter operating in Ku-band frequency range ever reported.

The next step in the design process is to extract the FBAR design parameters required for designing the optimised filters and design the FBARs using 1-D and 3-D FEM modelling. The next section presents the process of extraction of FBAR parameters for selected filter designs.

Table 4.5 Comparison of FBAR Filter Characteristics

References	Centre Frequency (GHz)	Insertion Loss (dB)	Out-of-Band (GHz)	Bandwidth (GHz)
[4]	29.2 23.8	-3.80 -3.80	-11 -13	0.99 0.81
[79]	19.8	-4.10	-18	0.39
[81]	9.08	-1.70	-21	0.28
Filter A Filter B	15.5 15.5	-3.2 -3.5	-12 -13	1.05 1.03

4.5 Extraction of FBAR Parameters

Based on the characteristics of FBAR filters obtained, the characteristics of FBARs are determined using the BVD model as described in the Chapter 3. For filters A and B, C_o, k^2_{eff}, f_s and f_p are already known from the design process. Equations 3.21 and 3.22 are used to calculate the values of C_m and L_m. Using equation 3.14, the Q_s and Q_p of both FBARs are calculated. The characterised parameters of the FBARs are summarised in Table 4.6.

Table 4.6 FBAR Parameters Extracted Using BVD

Parameter	Filter A		Filter B	
FBAR Type	FBAR 1 (series)	FBAR 2 (shunt)	FBAR 1 (series)	FBAR 2 (shunt)
C_o (pF)	0.6872	0.0614	0.4681	0.0901
C_m (pF)	0.0350	0.0379	0.0239	0.0258
L_m (nH)	2.8613	34.616	4.2	23.582
k^2_{eff} (%)	6.1	6.5	6.1	6.5
f_s (GHz)	15.90	14.70	15.90	14.70
f_p(GHz)	16.30	15.10	16.30	15.10
Q_s	16344.88	110523.72	23770.56	90808.98
Q_p	195430.99	181200.08	195638	181107.09

Using the 1-D Mason's model as described in Chapter 3, the electrical impedance of each FBAR is computed by applying MATLAB script (see Appendix B) as in equation 3.16:

$$Z_{in} = \frac{1}{j\omega C_0}\left(1 - k_t^2 \frac{\tan(kd/2)}{kd/2}\right)$$

where k_t^2 is replaced with k^2_{eff}. Since the values of C_o and k^2_{eff} are known, the thickness of the piezoelectric film, d is estimated using equation 3.9. The thickness obtained for both series FBAR A and FBAR B is 327 nm and 353 nm for both shunt FBAR A and FBAR B. It is observed that the thickness of the piezoelectric film calculated using equation 3.9 does not achieve the required resonant frequencies when applied in equation 3.16. This is because in equation 3.9, the resonance frequency is calculated using its acoustic velocity and the thickness of the piezoelectric film. Meanwhile in equation 3.16, the resonance frequency is not only influenced by the thickness of the piezoelectric film, it is also influenced by C_o, k^2_{eff} and k. Therefore, the thickness obtained for both series FBAR A and FBAR B is 319 nm and 344 nm for both shunt FBAR A and FBAR B. The results obtained from Mason's model are summarised in Table 4.7. It is observed that the extracted f_s^s, f_s^p, f_p^s and f_p^p from Mason's model are very close to the values in Table 4.6.

Table 4.7 FBAR Parameters Extracted Using Mason's Model

Parameter	**Filter A**		**Filter B**	
FBAR Type	**FBAR 1 (series)**	**FBAR 2 (shunt)**	**FBAR 1 (series)**	**FBAR 2 (shunt)**
C_o (pF)	0.6872	0.0614	0.4681	0.0901
C_m (pF)	0.0350	0.0379	0.0239	0.0258
L_m (nH)	2.8613	34.616	4.2	23.582
k^2_{eff} (%)	6.24	6.62	6.13	6.62
f_s (GHz)	15.89	14.71	15.89	14.69
f_p(GHz)	16.30	15.11	16.31	15.10
Q_s	15551.4	110143.1	21917.3	75496.02
Q_p	195522.4	181290.2	195638.6	181197.1

Figure 4.9 shows good agreement between the electrical impedance of FBARs calculated using the closed-forms and 1-D Mason model. The results also show that FBARs with bandwidths of around 500 MHz are required for wideband FBAR filters in Ku-band. However, it is challenging to design such FBARs due to limitations of the electromechanical coupling coefficient of the piezoelectric material used, as described in section 4.2.

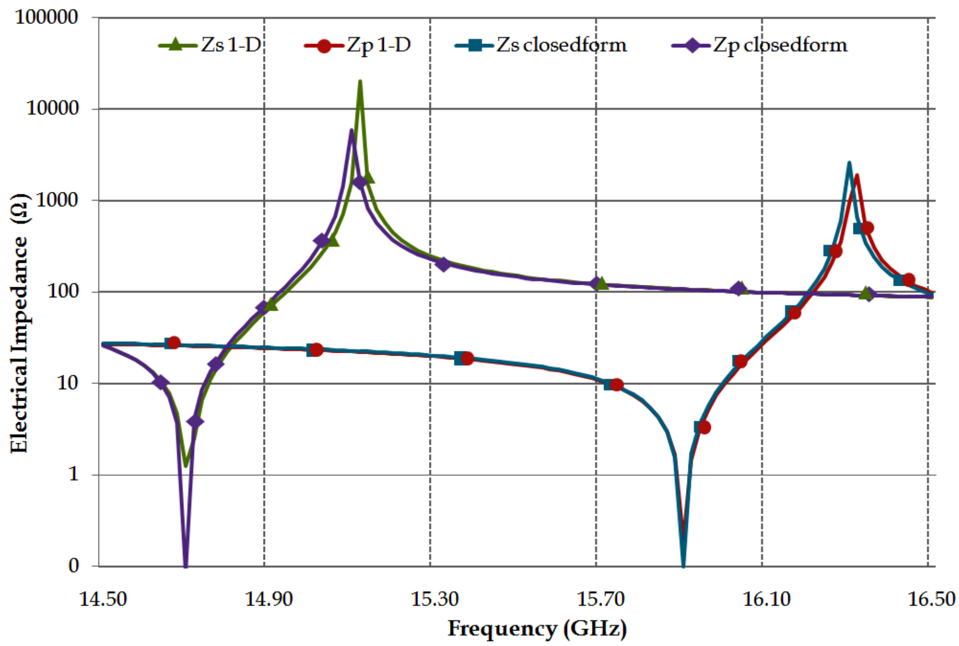

Figure 4.9 Comparison of FBAR Electrical Impedance

4.6 Conclusion

This chapter presented the design of Ku-band FBAR filters using a set of closed-form expressions. The effect of design parameters such as f_s^s, f_s^p, f_p^s, f_p^p, f_1 and f_2 were analysed and discussed. From the analysis, we concluded that increasing the order of the FBAR filter will improve out-of-band rejection; however, insertion loss and the 3 dB bandwidth will degrade. The Ku-band FBAR filter with insertion loss of -3.5 dB, 3 dB bandwidth of 1.05 GHz was achieved. The FBAR characteristics required for these filters were presented. To further analyse and optimise the FBAR designs evaluated using 1-D modelling, the 3-D Finite Element Method (FEM) will be presented in the next chapter.

CHAPTER 5 : IMPLEMENTATION AND OPTIMISATION OF KU-BAND FBAR

5.1 Introduction

This chapter focuses on the design and analysis of the film bulk acoustic wave resonator (FBAR) using three-dimensional (3-D) finite element modelling (FEM) including the layout design, fabrication process and FBAR modelling. The characteristics of the proposed FBAR are based on the characteristics of FBARs obtained using the Butterworth Van Dyke (BVD) model in Chapter 4. The influence of various geometrical parameters and material losses on FBAR performance is analysed and discussed in detail to find suitable solutions for designing a wide bandwidth and high quality (*Q*) factor Ku -band FBAR.

5.2 Design and Modelling of FBAR

The literature suggests that AlN is the most suitable piezoelectric material to design an FBAR, which operates at frequencies higher than 10 GHz due to its high acoustic velocity compared to ZnO and PZT. The air-gap type FBAR is chosen as it is simpler to manufacture compared to other types of FBARs. Based on the results obtained (see Table 4.6), four different FBARs have to be designed in order to construct Filter A and Filter B. In this section, the optimisation of the geometrical parameters of the FBAR is outlined to achieve a higher k^2_{eff} with a high *Q* factor in Ku-band. As mentioned previously, a higher k^2_{eff} will result in wider bandwidth while a higher *Q* factor will result in an FBAR with better performance. The following sub-section will explain the layout design, fabrication process and the model of the FBAR.

5.2.1 Layout Design and Fabrication Steps of FBAR

In this work, the air-gap FBAR as shown in Figure 5.1 (a) is adopted (the cross-section view of the FBAR depicted in Figure 5.1 (b)). The FBAR is designed using AlN as the piezoelectric material, ruthenium (Ru) as the top and bottom electrodes and silicon nitride (Si_3N_4) as the membrane on silicon (Si) substrate.

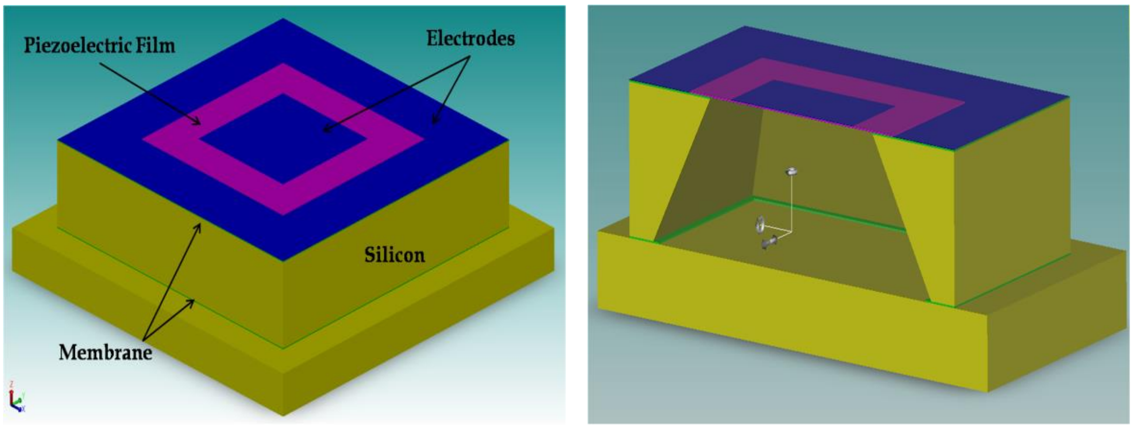

(a) (b)

Figure 5.1 (a) 3-D Model of FBAR (b) Cross-section of FBAR

Before beginning the process steps, it is important to make sure the material properties of the AlN and Ru are in the correct units. All the material properties are converted according to the units given in the simulation tool. The material properties of AlN are given in CoventorWare ® 2010. However, the material properties of Ru are added manually. Table 5.1 shows the material properties of the AlN and Ru used. The properties of each material are important as they contribute to the characteristics of the FBAR.

Table 5.1 Material Properties of AlN

Parameters	**AlN**
Density (kg/µm^3)	3.26e^{-15}
Thermal Expansion Coefficient (1/K)	4.50e^{-6}
Thermal Conductivity (pW/µmK)	1.60e^{-8}
Specific Heat (pJ/kgK)	7.40e^{14}
Electric Conductivity (pS/µm)	1.00e^{-5}
Elastic Constants: AnIsotropic (10^{4}µN/µm^2)	
D1111 ($c^E{}_{11}$)	3.45e^5
D1122 ($c^E{}_{12}$)	1.25e^5
D2222 ($c^E{}_{11}$)	3.45e^5
D1133 ($c^E{}_{13}$)	1.20e^5
D2233 ($c^E{}_{13}$)	1.20e^5
D3333 ($c^E{}_{33}$)	3.95e^5
D1212 ($c^E{}_{66}$)	1.10e^5
D1313 ($c^E{}_{44}$)	1.18e^5
D2323 ($c^E{}_{44}$)	1.18e^5
Strain Coefficients (10e^{-6} pC/µN)	
e_{31}	-2.65
e_{33}	5.53
e_{15}	-4.07
Dielectric (10e^{-12} pF/µm)	
ε^{11}	9.03
ε^{33}	10.73

Table 5.2 Material Properties of Ru, Si and Si_3N_4

Parameters	**Ru**	**Si (100)**	**Si_3N_4**
Density (kg/µm^3)	1.25e^{-14}	2.331e^{-15}	2.70e^{-15}
Thermal Expansion Coefficient (1/K)	6.40e^{-6}	2.49e^{-6}	1.60e^{-6}
Thermal Conductivity (pW/µmK)	1.17e^8	1.57e^8	2.50e^7
Specific Heat (pJ/kgK)	2.38e^{14}	7.03e^{14}	1.70e^{14}
Modulus Young, E (MPa)	4.47e^5	1.302e^5	2.22e^5
Poisson	0.3	0.278	0.27

The width (W), length (L) and thickness (t) of each piezoelectric and electrode layer as shown in Figure 5.2 are varied to analyse the performance of the FBAR under different conditions. The 3-D FEM solver CoventorWare ® 2010 is used for optimizing the physical design parameters of the FBAR.

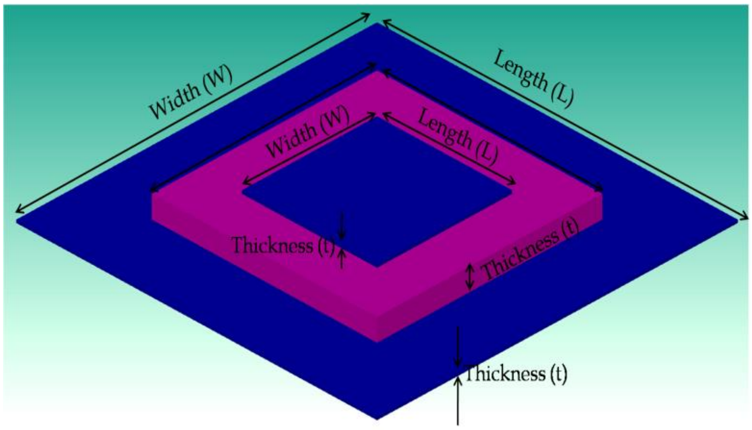

Figure 5.2 Geometrical Design Parameters

The optimisation of the FBAR involved repeating the same fabrication steps by varying the geometrical parameter values. The fabrication steps are as follows and are illustrated in Figure 5.3 [15, 61]:

1) Deposition of low-stress Si_3N_4:
   The two layers of Si_3N_4 act as a support membrane layer for the FBAR cantilever and as an etching mask, respectively.

2) Backside etching of Si:
   The wet etching of the backside of the Si is done to create the air-gap.

3) Deposition of Ru:
   The Ru is stacked over the membrane layer and etched to form the bottom electrode.

4) Deposition of AlN:

   The AlN is stacked on the bottom electrode and etched to form the piezoelectric layer.

5) Deposition of Ru:

   The Ru is stacked above the piezoelectric layer and etched to form the top electrode.

6) Si layer etch:

   The residue of Si is completely etched to leave an edge-supported piezoelectric layer.

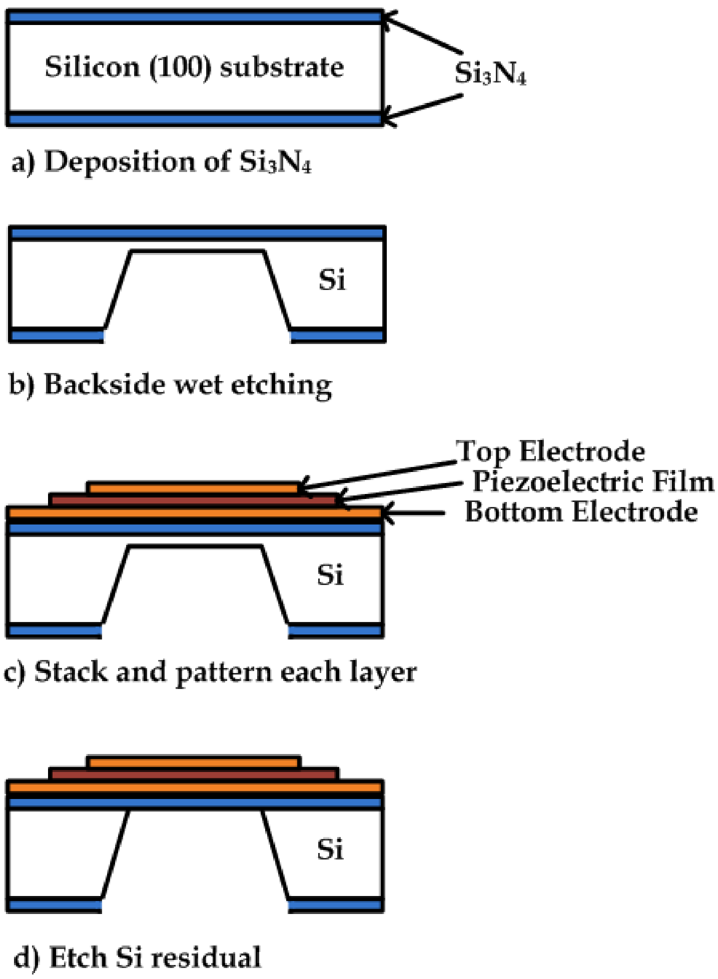

Figure 5.3 Fabrication Process Steps of an Air-gap FBAR

After completing the design of the FBAR, the 3-D model of the FBAR is built and meshed. Meshing is used to divide the model into small elements for FEM analysis. The solid model of the FBAR is shown in Figure 5.4. In this work, the electrode layers are meshed together with the piezoelectric layer to include the effects of electrode layers in the simulation results.

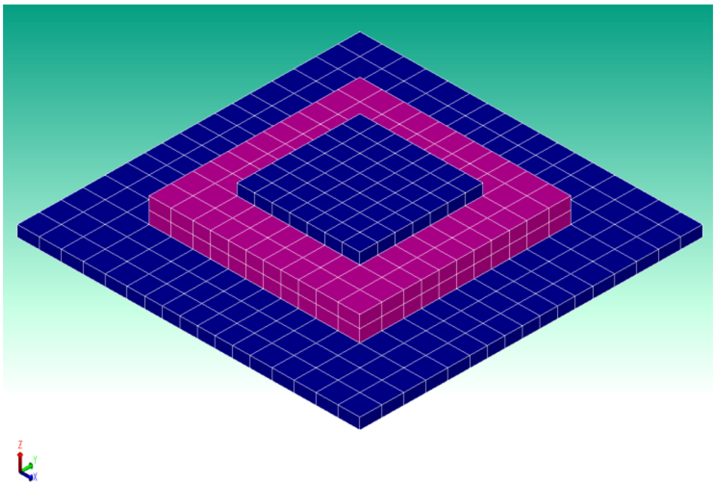

Figure 5.4 Meshed Model of FBAR

The analysis of the FBAR was done according to the steps explained in sub-section 3.3.6.2. From the DC analysis, C_0 is calculated by using equation 3.29. C_0 is an important parameter in defining the impedance matching when designing a filter as discussed in Chapter 4.

In modal analysis, the resonance frequency of the FBAR is determined by the thickness of the piezoelectric film and electrodes. Series resonance frequency (f_s) and parallel resonance frequency (f_p) are identified as the frequencies of interest at which the breathing mode shape has the opposite normal displacement of the top piezoelectric surface compared to the bottom piezoelectric surface as shown in Figure 5.5. From the values of f_s and f_p obtained from the simulation, the C_m and L_m are calculated using equations 3.30 and 3.31.

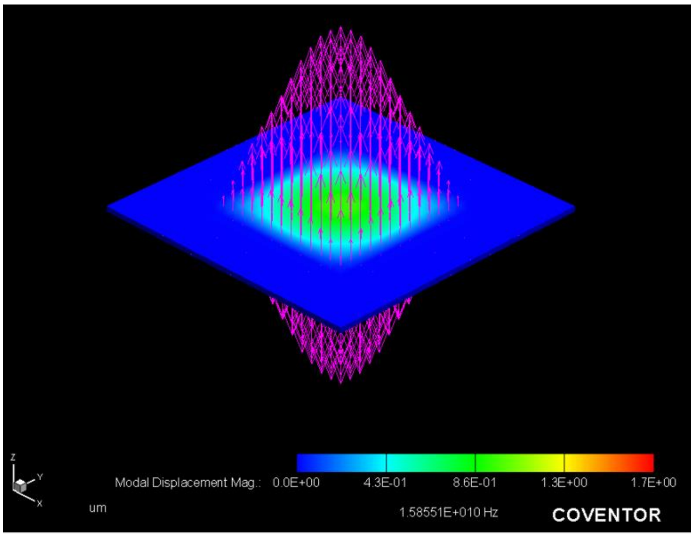

Figure 5.5 Fundamental Breathing Mode Resonance in Modal Analysis

Finally, in the harmonic analysis, the electrical impedance and Q factor are obtained. The electrical impedance magnitude and phase are computed from the result of piezoelectric patch charge using equations 3.32 to 3.38. It is observed that there are slight differences in f_s and f_p in the modal analysis and harmonic analysis. This is because in harmonic analysis, the effect of piezoelectric coefficients is taken into account as well as the mechanical properties. In modal analysis, only geometrical and mechanical properties such as density and elastic stiffness are considered. Therefore, k^2_{eff} from the modal analysis is a little higher than the harmonic analysis. Thus, throughout this study, modal analysis was done as the preliminary analysis to estimate the thickness of AlN and Ru to obtain f_s and f_p. The more accurate f_s and f_p obtained from the harmonic analysis are then considered.

As explained in Chapter 3, damping should be considered in the 3-D FEM in order to present FBAR with behaviour that is more realistic. Akhieser attenuation approximation was used to compute α by using equation 2.4. Then, by using equation 2.12, the value of β is calculated. The α and β are calculated at 1 GHz and 15 GHz. The value of α obtained at 1 GHz is 68.8 m^{-1} and 15483 m^{-1} at

15 GHz. From the *a* obtained, *β* is found to have the same value at 1 GHz and 15 GHz, which is 3.84^{e-14} s. In [122], the value of *a* and *β* obtained at 1 GHz is 74.8 m^{-1} and 2.82e^{-14} s, respectively and these values are calculated by using the material properties of silicon. To further verify the results, *a* and *β* are then calculated at 5 GHz, 10 GHz and 20 GHz. The value of *β* is found to be constant at different frequencies while *a* varied. Finally, the value of the *Q* factor was calculated using equation 2.4. The values of *a*, *β* and the *Q* factor obtained in this work are summarised in Table 5.3. As expected, it is observed that as the frequency increases, the *Q* factor decreases.

Table 5.3 Material Damping Coefficients and *Q* Factor

Frequency / Parameters	**1 GHz**	**5 GHz**	**10 GHz**	**15 GHz**	**20 GHz**
a (1/s)	6.88×10^1	1.72×10^3	6.88×10^3	1.55×10^4	2.75×10^4
B (s)	3.84×10^{-14}	3.84×10^{-14}	3.84×10^{-14}	3.84×10^{-14}	3.84×10^{-14}
Q factor	4150	829	564	277	207

5.3 Analysis of the Effects of Design Parameters

5.3.1 Influence of Piezoelectric Film Thickness

The properties and thickness of the AlN have a significant influence on the performance of the FBAR in terms of resonance frequency, bandwidth and insertion loss, as shown by equations 3.9 and 3.16 in Chapter 3. Figure 5.6 shows the relationship between resonance frequency and AlN thickness. In 1-D modelling, the effect of electrodes on f_s and f_p is ignored. Therefore, the thickness of AlN is different in 1-D compared to 3-D FEM where electrodes are taken into account. By referring to the estimation given in [81] for the purpose of this analysis, the bottom and top electrodes, Ru is set to 30 nm and AlN varies from 125 nm to 205 nm. The simulation result indicates that as the thickness of the AlN increases, the series resonance frequency decreases. This suggests that a thicker piezoelectric film reduces the influence of the electrode thickness upon the resonance frequency. This occurrence is supported by the notion that the acoustic path is proportional to the piezoelectric film thickness as modelled in equation 3.9. The piezoelectric film thickness is directly proportional to the acoustic path and inversely proportional to the resonance frequency.

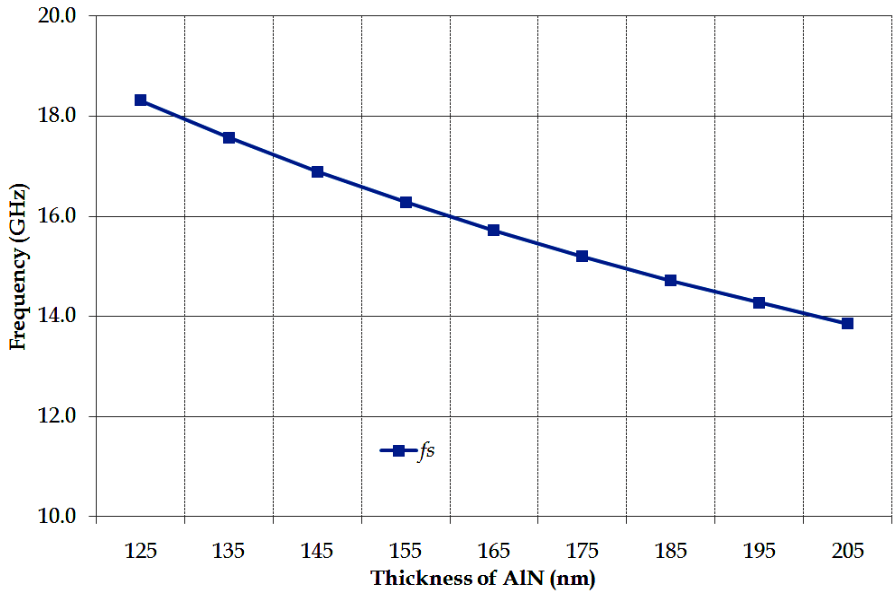

Figure 5.6 Influence of Piezoelectric Film Thickness on f_s

As mentioned in Chapter 2, the resonance frequency of the FBAR is also influenced by the electrodes. The next sub-section discusses the effects of different electrode materials on FBAR characteristics.

5.3.2 Influence of Electrode Materials

Previous studies have shown that the resonance frequency of an FBAR is determined by the thickness of the piezoelectric film and electrodes. In this study, Mo and Ru are used as the electrode materials for comparison due to their excellent material properties. The thickness of Mo and Ru are varied from 5 nm to 100 nm while the thickness of AlN stays constant at 205 nm. Figure 5.7

demonstrates the simulation results for series resonance frequency with the different materials. It can be seen that Mo shows a higher series resonance frequency compared to Ru. This is due to the lower mass density of Mo and its lessened mass loading effect when compared to Ru. The mass density of Mo is 10300 kg/m^3; it is 12500 kg/m^3 for Ru. From Figure 5.7 too, it can be observed that the series resonance frequency for both electrode materials increases when the electrode thickness is reduced. It can also be concluded that even though Ru has a higher acoustic velocity (6931 m/s) than Mo (6213 m/s), the mass loading effect is only influenced by the mass density of the material.

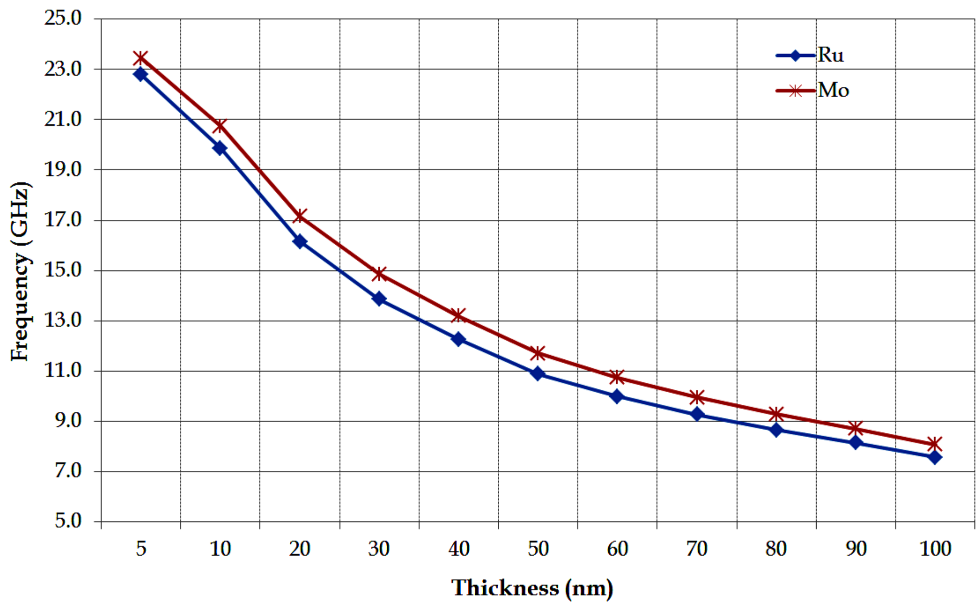

Figure 5.7 Influence of Electrode Material and Thickness

5.3.3 Influence of Varying Either the Bottom or Top Electrode

In this simulation, the thickness of the AlN was set to 185 nm, the top electrode is set constant at 25 nm and the bottom electrode varied from 25 nm to 45 nm. Figure 5.8 demonstrates the relationship between resonance frequency, the electromechanical coupling coefficient and the thickness of the bottom electrode. Similarly, Figure 5.9 plots the relationship between resonance frequency, the electromechanical coupling coefficient and the thickness of the top electrode. The bottom electrode is constant at 25 nm while the top electrode varies from 25 nm to 45 nm. In both analyses, it is observed that the resonance frequency increases as the thickness of the variable thickness electrode decreases. Both analyses showed the same resonance frequency of the equivalent electrode thickness. Hence, the mass loading can be done either on the top or on the bottom electrode to achieve the desired resonance frequency. It is also observed that k^2_{eff} decreases as the thickness of the electrode increases. This is due to an increase in the thickness ratio of electrodes to piezoelectric material. A detailed discussion on the thickness ratio will be presented in the following sub-section.

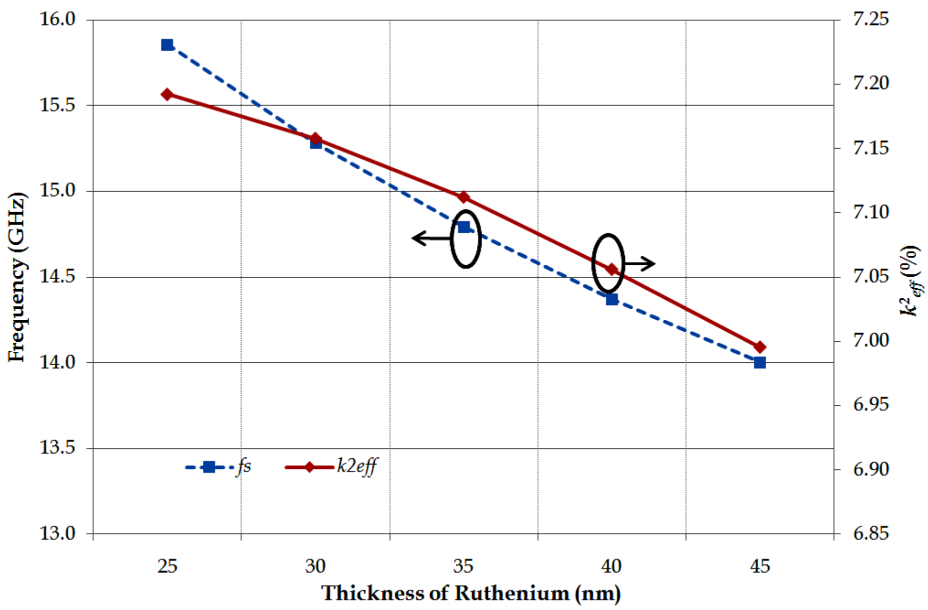

Figure 5.8 Influence of Varying the Thickness of the Bottom Electrode

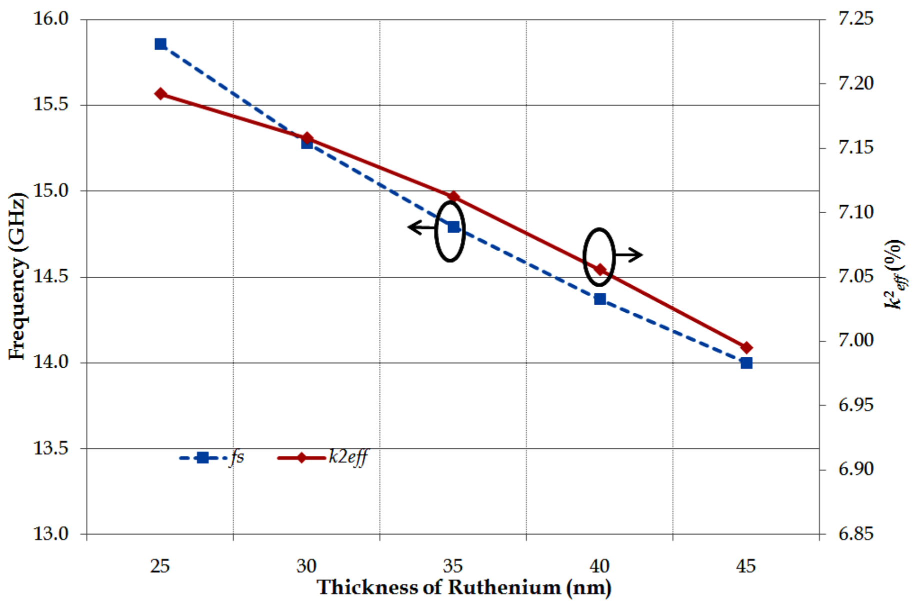

Figure 5.9 Influence of Varying the Thickness of the Top Electrode

The enhancement of k^2_{eff} of the FBAR is possible by controlling the thickness ratio of electrodes to piezoelectric materials [72]. The next sub-section discusses the effects of the thickness ratio of electrode to piezoelectric material on FBAR performance.

5.3.4 Influence of Thickness Ratio of Electrodes to Piezoelectric Materials

As mentioned previously, k^2_{eff} is a measure of the relative frequency spacing between f_s and f_p, and determines the bandwidth of a filter. According to [143] and [144], the use of a high-acoustic impedance electrode material of an FBAR is effective to achieve wideband filter and provides excellent enhancement. For this analysis, Ru and Mo are used for comparison purposes. It is demonstrated in the analysis that the maximum k^2_{eff} achieved is 7.24% and 7.17% when the t_m/t_p is 0.1 for Ru and Mo, respectively. k^2_{eff} decreases gradually after the ratio is more than 0.1 for both materials. Figure 5.10 presents the results of the analysis and shows that Ru has higher k^2_{eff} than Mo. The acoustic impedance of Ru and Mo are 86.3 MPa/m²s and 68.5 MPa/m²s, respectively. Table 5.4 shows the relationship between k^2_{eff} and bandwidth for both Ru and Mo done. As the data show, Ru affords wider bandwidth compared to Mo, thus Ru is chosen as the electrode material throughout this research. Material damping is one of the features that influence the performance of FBARs. The next sub-section discusses the effects of material damping on FBAR performance.

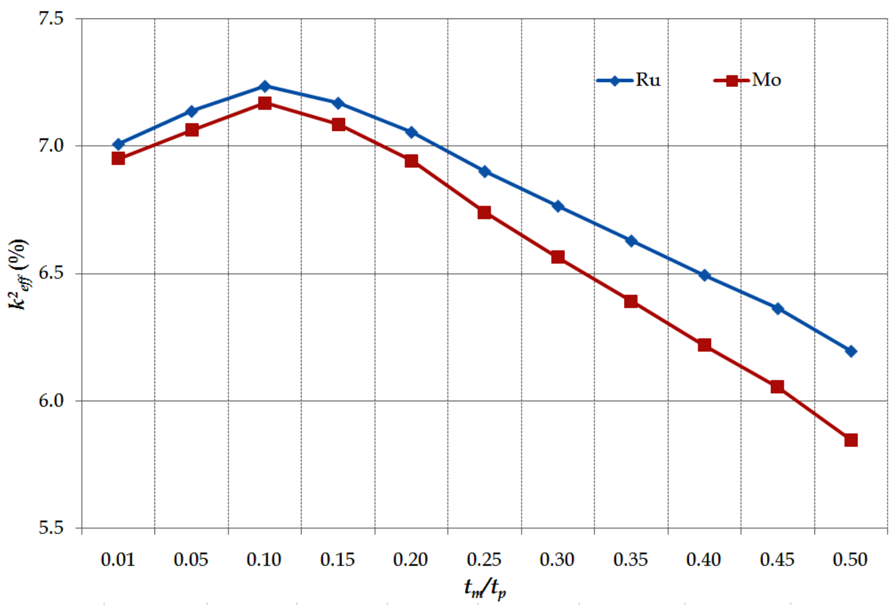

Figure 5.10 Relationship between Thickness Ratios with k^2_{eff}

Table 5.4 Relationship between k^2_{eff} and the Bandwidth of FBAR

t_m/t_p	k^2_{eff} (%)		Bandwidth (GHz)	
	Ru	**Mo**	**Ru**	**Mo**
0.005	6.38	6.27	0.71	0.69
0.01	7.01	6.95	0.68	0.70
0.05	7.14	7.06	0.61	0.59
0.10	7.24	7.17	0.51	0.49
0.15	7.17	7.09	0.44	0.41
0.20	7.06	6.94	0.38	0.36
0.25	6.90	6.74	0.33	0.31
0.30	6.77	6.57	0.29	0.28
0.35	6.63	6.39	0.26	0.26
0.40	6.49	6.22	0.24	0.23
0.45	6.36	6.05	0.22	0.22
0.50	6.20	5.85	0.19	0.19

5.3.5 Influence of Material Damping

As mentioned previously, 1-D modelling does not take into account the influence of electrodes and other losses such as thermoelastic damping (TED) and material damping. Therefore, the *Q* factor obtained in the analysis described in Chapter 4 is too high. For the purpose of analysis, an FBAR with an AlN thickness of 185 nm and Ru thickness of 25 nm is selected and the effect of different types of losses on the FBAR is investigated. Firstly, the loss from only TED is considered and its effect on the electrical impedance and the *Q* factor of the FBAR is analysed. Then, the material damping coefficients (α and β) are introduced along with the TED. The values of α and β used are $6.88e^{1}$/s and $2.82e^{-14}$ s, respectively. The comparison between the two different losses is presented in Figure 5.11 and Figure 5.12. As shown in Figure 5.11, spurious modes still occur in the electrical impedance response when only TED is included. However, when the material damping is included, it is observed that the spurious modes are suppressed. This is because material damping has damped out the harmonics [122].

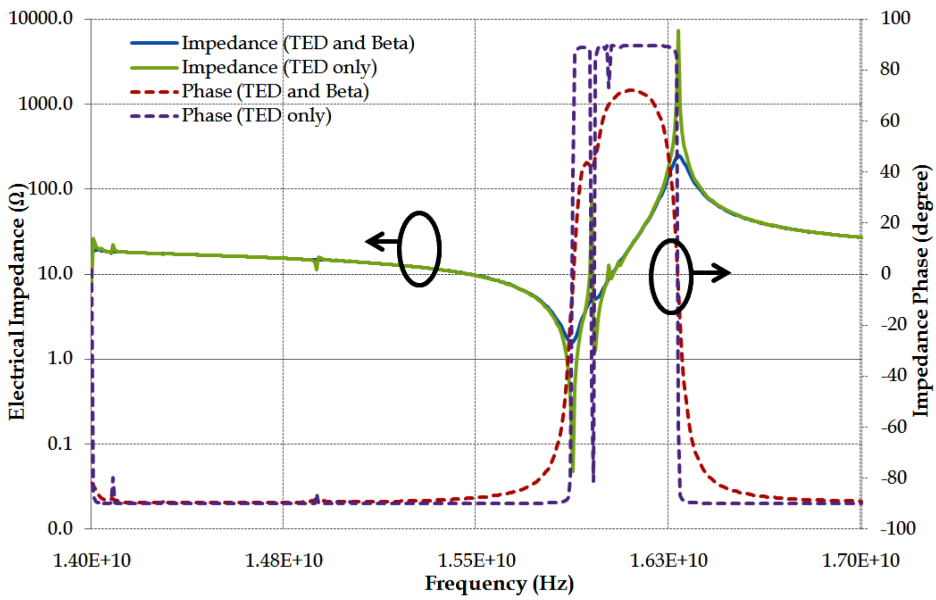

Figure 5.11 Effect of Different Losses on Electrical Impedance

Figure 5.12 shows the influence of the different losses on the Q factor of the FBAR. It was observed that the Q factor is as high as 25000 when only TED is considered in the simulation. Conversely, when material damping is taken into account, the highest Q factor obtained is 305.70, which is more realistic.

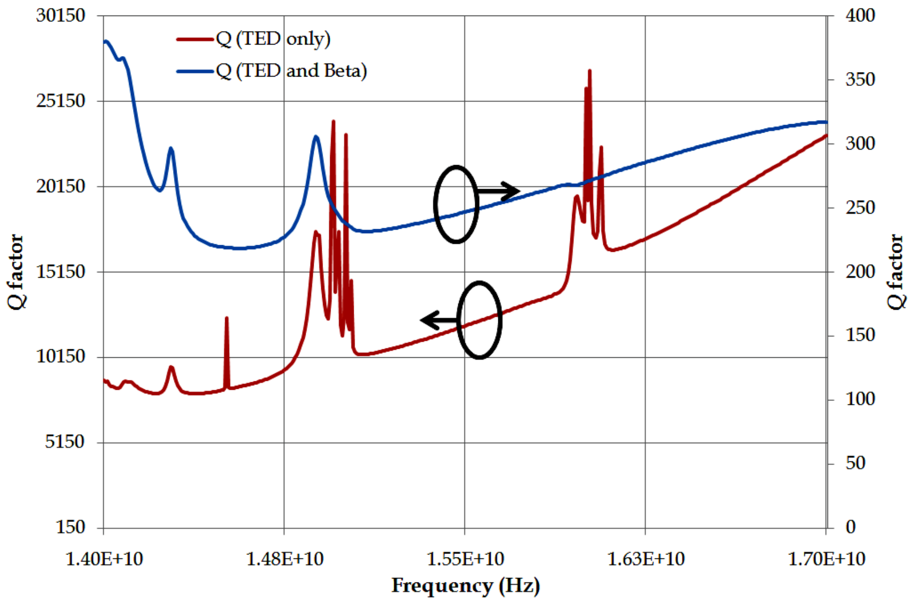

Figure 5.12 Effect of Different Losses on Q Factor

This confirmed that the major loss is from the material damping, while TED only contributes a small percentage of the overall losses. It is further observed that the damping causes a negligible change to the series and parallel frequency and k^2_{eff} is almost constant for both FBARs as summarised in Table 5.5.

Table 5.5 Effect of Different Losses on FBAR Characteristics

FBAR	f_s **(GHz)**	f_p **(GHz)**	k^2_{eff} **(%)**
TED only	15.87	16.28	6.25
TED and β	15.87	16.28	6.25

Figure 5.13 demonstrates the Q factor calculated using the Z_s and Z_p obtained from the 3-D simulation using equation 3.14 and the Q factor directly obtained from the simulation. The values of Q_s and Q_p obtained using the equation are

229.27 and 267.42, respectively, while Q_s and Q_p obtained directly from the simulation are 265.96 and 287.92 respectively. Equation 3.14 estimates Q_s and Q_p independently, but in the 3-D simulation the Q factor is computed using equation 2.4. Therefore, the highest Q factor obtained from the simulation is 305.70 at 14.9 GHz.

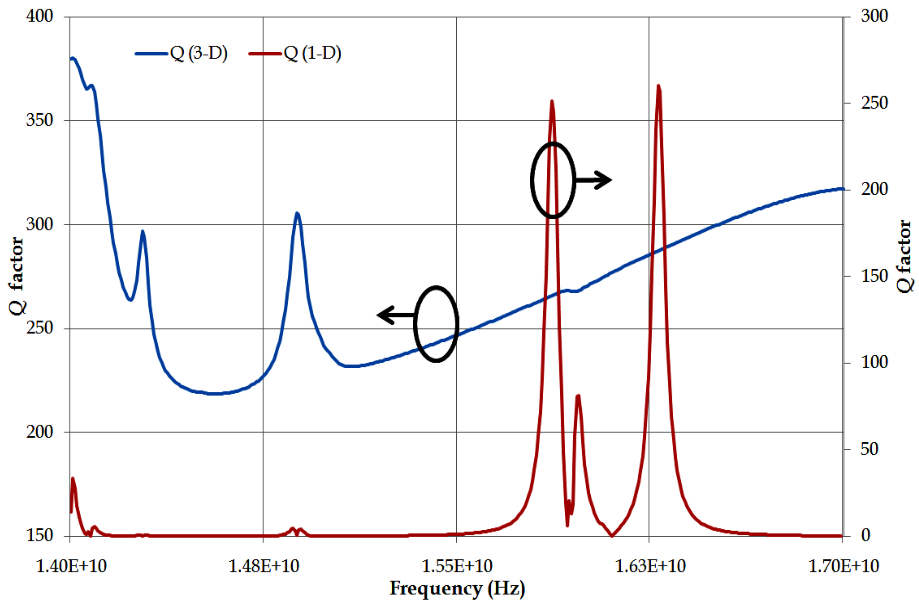

Figure 5.13 Comparison of Method of Obtaining Q Factor

Regardless of which frequency is the highest Q factor, this study only focused on Q_s and Q_p. It has been verified that the values for Q_s and Q_p obtained through both methods are close to each other. Hence, the Q_s and Q_p from the 3-D simulation are employed throughout this study.

Figure 5.14 shows the comparison of different values of material damping coefficients on electrical impedance frequency response. The values of β used are 2.82e^{-14} s and 3.84e^{-14} s. FBARs with AlN thickness of 185 nm and Ru thickness of 25 nm with area size of 30 µm x 30 µm are used for this analysis. It is observed that the higher value of β causes f_p peak to become flatter, which means the electrical impedance is lower. The Z_s and Z_p obtained are 1.58 Ω and

247.43 Ω respectively when β is set to 3.84e^{-14} s. When β is set to 2.82e^{-14} s, on the other hand, the Z_s and Z_p obtained are 0.79 Ω and 248.49 Ω respectively. However, it was noticed that there is no effect on f_s and f_p. Thus, the k^2_{eff} of the FBAR is not influenced by the damping values.

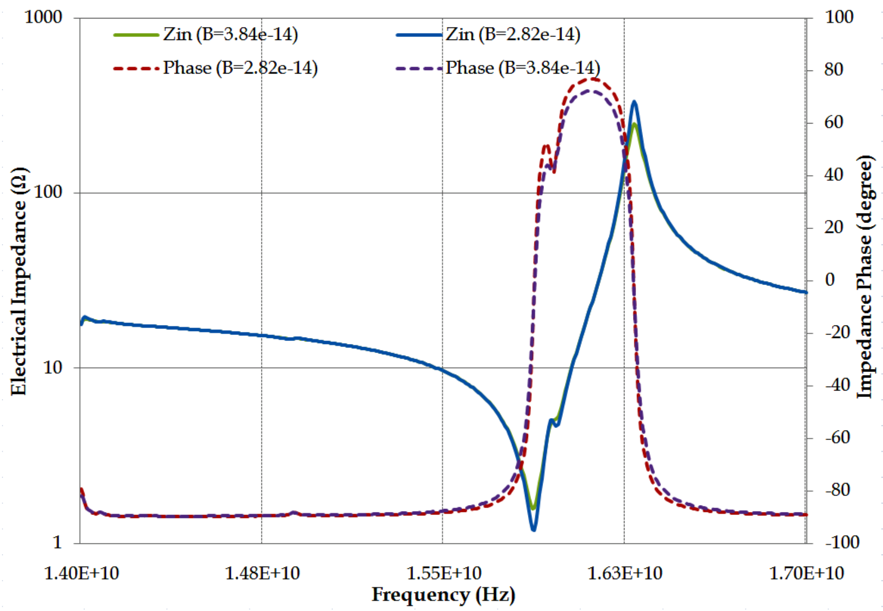

Figure 5.14 Effect of Material Damping on Electrical Impedance of FBAR

Figure 5.15 shows the effect of different values of material damping coefficients on the Q factor. From this analysis, the values of Q_s and Q_p obtained when β is set to 3.84e^{-14} s are 265.96 and 287.92, correspondingly. Meanwhile, Q_s and Q_p obtained when β is set to 2.82e^{-14} s are 360.24 and 389.73, respectively. In this analysis, the highest Q factors obtained from the simulations are 305.70 at 14.9 GHz when β is 3.84e^{-14} s and 431.09 at 14.9 GHz when β is 2.82e^{-14} s. It is thus verified that the Q factor decreases when β increases.

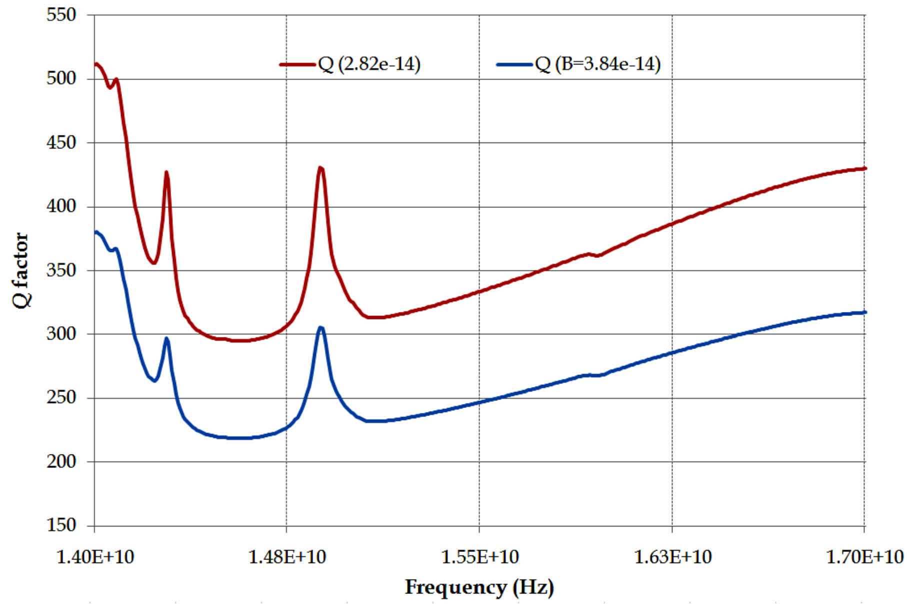

Figure 5.15 Effect of Material Damping on *Q* Factor of FBAR

The resonance area (WxL) also acts as an important parameter on characterising the FBAR. The effects of resonance area on FBAR performance will be discussed in the next sub-section.

5.3.6 Influence of Resonance Area (WxL)

Figure 5.16 shows the influence of the resonance area on the electrical impedance of the FBAR. The area is set from 28x28 μm² to 36x36 μm². For an FBAR with an area of 36x36 μm², the minimum impedance (Z_s) achieved is 1.06 Ω and maximum impedance (Z_p) achieved is 180.53 Ω. Meanwhile for an FBAR with an area of 28x28 μm², Z_s achieved is 1.82 Ω and Z_p achieved is 281.07 Ω. Therefore, it is predicted that the *Q* factor will be lower in a smaller area. It is observed that as the resonance area increases, there is no change in the resonance frequency but the impedance of the FBAR decreases. Therefore, by designing an appropriate resonance area, impedance matching of the FBAR can be achieved.

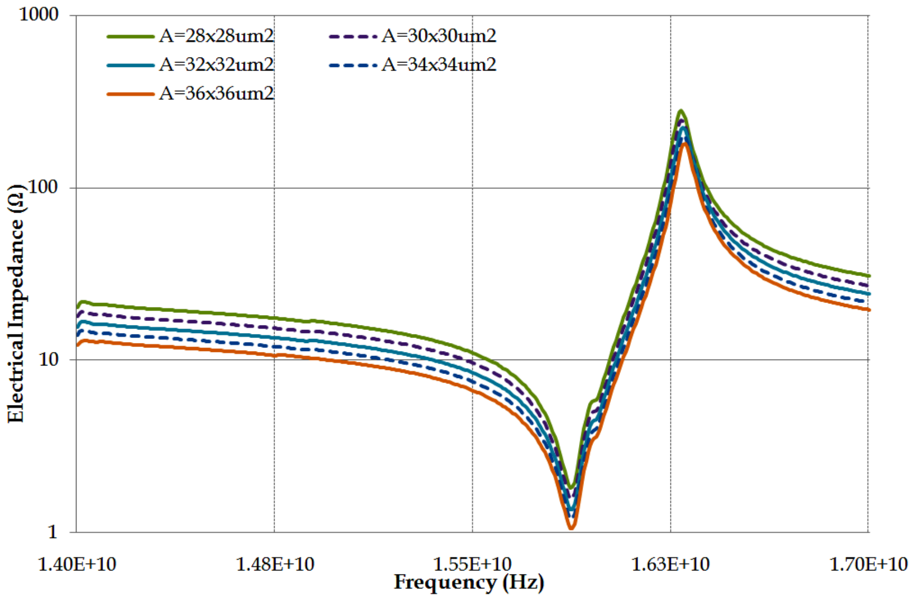

Figure 5.16 Influence of Resonance Area on Electrical Impedance of FBAR

Furthermore, it is shown that as the area increases, the static capacitance also increases gradually, as depicted in Figure 5.17. This is verified by using equation 3.17 as given in Chapter 3. It is further shown that area size does not have a significant effect on the Q factor values. Figure 5.18 shows the influence of the size of the area on the Q factor. It is observed that for an FBAR with an area size of 28x28 μm^2 to 36x36 μm^2, Q_s and Q_p are almost constant. For area size of 28x28 μm^2 to 34x34 μm^2, the highest Q factor obtained is 306.15 at 14.9 GHz. Meanwhile, for an FBAR with an area size of 36 x 36 μm^2, the highest Q factor obtained is 311.32 at 14.8 GHz. All the parameters obtained from this analysis are listed in Table 5.6.

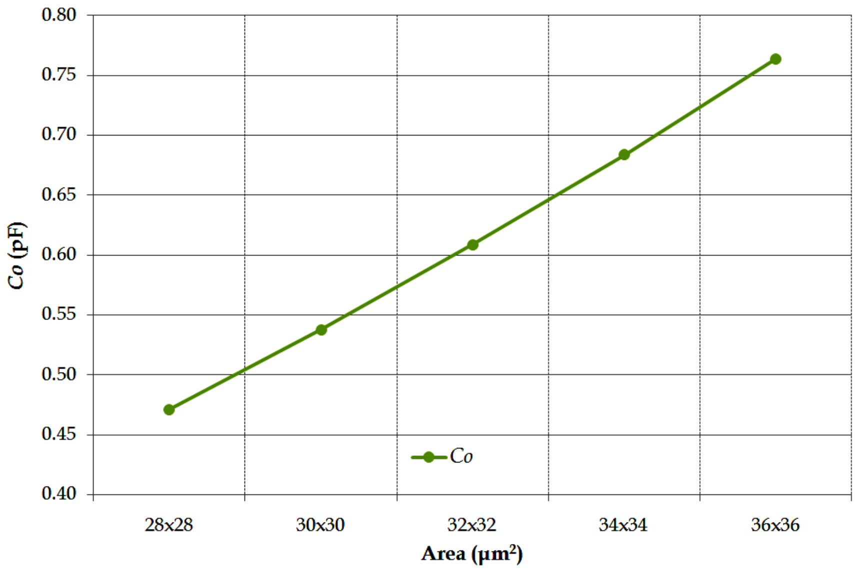

Figure 5.17 Influence of Resonance Area on the Static Capacitance (C_0)

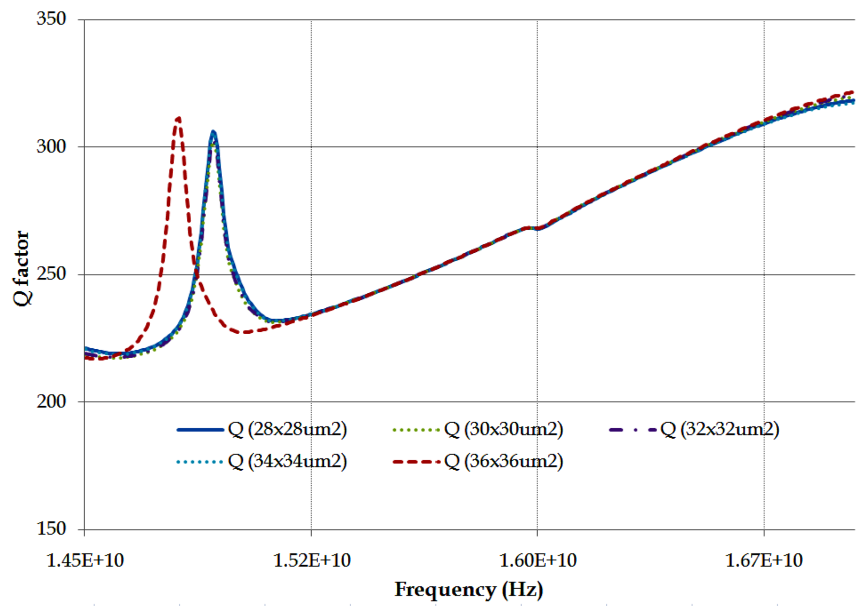

Figure 5.18 Influence of Resonance Area on *Q* Factor

Table 5.6 Summary of Influence of Resonance Area

Resonance Area (μm²)	f_s **(GHz)**	f_p **(GHz)**	**Impedance (ohm)**		**Q factor**		k^2_{eff} **(%)**	C_0 **(pF)**
			Z_s	Z_p	Q_s	Q_p		
28x28	15.88	16.29	1.82	281.07	265.98	287.91	6.36	0.47
30x30	15.87	16.29	1.58	247.42	265.96	287.92	6.36	0.54
32x32	15.88	16.30	1.37	223.47	266.36	288.56	6.36	0.61
34x34	15.88	16.30	1.21	199.63	266.35	288.57	6.36	0.68
36x36	15.88	16.30	1.06	180.53	266.36	289.12	6.47	0.76

The next section will summarise the geometrical parameter effects of the FBAR.

5.4 Summary of Geometrical Parameter Effects

The analysis has shown that the k^2_{eff} of the Ku-band FBAR can be improved by optimising the thickness ratio of the electrode to the piezoelectric material. It is also shown that the width and length of the FBAR have no significant effect on k^2_{eff}. The optimisation maximised the k^2_{eff} of the FBAR, and thus a wider bandwidth has been achieved. The following are the key outcomes of the analysis:

1. The optimum thickness ratio of electrode to piezoelectric material ranges from 0.05 to 0.15 to achieve maximum value of k^2_{eff} of the FBAR.

2. A higher k^2_{eff} of the FBAR was achieved by using electrode material with higher acoustic impedance. Ruthenium is the better electrode material compared to Molybdenum in the design of Ku-band FBAR because of its higher acoustic impedance. Therefore, Ru is used as the electrodes of the FBAR. A k^2_{eff} of 6.36% has been achieved in the analysis.

3. The optimisation of the area size shows no significant effect on the series frequency, parallel frequency, k^2_{eff} and the Q factor of the FBAR. However, the area size can be used to achieve the required static

capacitance with minimal impact on electrical impedance and other parameters.

4. Two types of damping are considered in the 3-D simulation, which are the TED and material damping. The values of material damping coefficients (a and β) are 1.55e^4/s and 3.84e^{-14} s, respectively at 15 GHz. Meanwhile the TED was directly computed from the CoventorWare ® 2010. The study confirmed that the major loss is from the material damping and TED only contributes a small percentage (5%) of the overall losses. The analysis also verified that the Q_s and Q_p achieved from equation 3.14 and from the simulation are close to each other.

Based on the analysis of the geometrical parameter effects, the proposed Ku-band FBAR was designed using the same air-gap FBAR model as described in section 5.2. Based on the results obtained from Chapter 4, four different FBARs needed to be designed in order to construct Filter A and Filter B as listed in Table 4.6. The required f_s and f_p of the series FBAR A and FBAR B are 15.9 GHz and 16.3 GHz, respectively. Meanwhile, the required f_s and f_p of the shunt FBAR A and FBAR B are 14.7 GHz and 15.1 GHz, respectively. The k^2_{eff} are expected to achieve 6.5% for both FBARs. Based on the results obtained in sub-section 5.3.5, the Q factors predicted are around 300-400. The optimisation of the FBARs is carried out to achieve high k^2_{eff} with a high Q factor as discussed in the following sub-section.

5.5 Optimisation of Ku-band FBAR

In this section, the effects of the thickness ratio of electrodes to piezoelectric material and the active area will be analysed to obtain a high k^2_{eff} and Q factor for the Ku-band FBAR.

5.5.1 Optimisation of Thickness Ratio of Electrodes to Piezoelectric Material

As discussed earlier, the enhancement of the coupling coefficient of the FBAR is possible by controlling the thickness ratio of electrodes to piezoelectric materials (t_m/t_p). From the analysis in section 5.3, it is observed that the optimum ratio ranges from 0.05 to 0.15. Based on the FBAR parameters given in Table 4.6, modal analysis is carried out to achieve the required frequencies. From the results obtained, a few combinations of AlN and Ru based on the t_m/t_p are investigated. Once the thicknesses of the AlN and Ru are chosen, harmonic analysis is completed. The analysis suggests that 1 nm difference of the AlN or Ru thickness will result in frequency differences of 40-50 MHz. Therefore, targeting the precise resonance frequencies is quite difficult.

In order to verify the FBARs propagated in a longitudinal mode (Z-axis), the harmonic displacements of the FBARs are plotted as shown in Figure 5.19 (a) and Figure 5.20 (a). From the figures, it can be seen that the FBARs propagate in the longitudinal mode, which means that the magnitude of the Z-axis is higher than the magnitude of the X-axis and Y-axis. To verify that the f_s and f_p are the right breathing modes for the specified thickness, the graphs of piezoelectric charge responses of the FBARs are plotted as in Figure 5.19 (b) and Figure 5.20 (b). From Figure 5.19 (b), it is observed that the f_s of the series FBAR is the same frequency obtained where the maximum harmonic displacement of the FBAR occurs, as shown in Figure 5.19 (a). The same observation is made for the f_s of the shunt FBAR, as shown in Figure 5.20 (a) and Figure 5.20 (b).

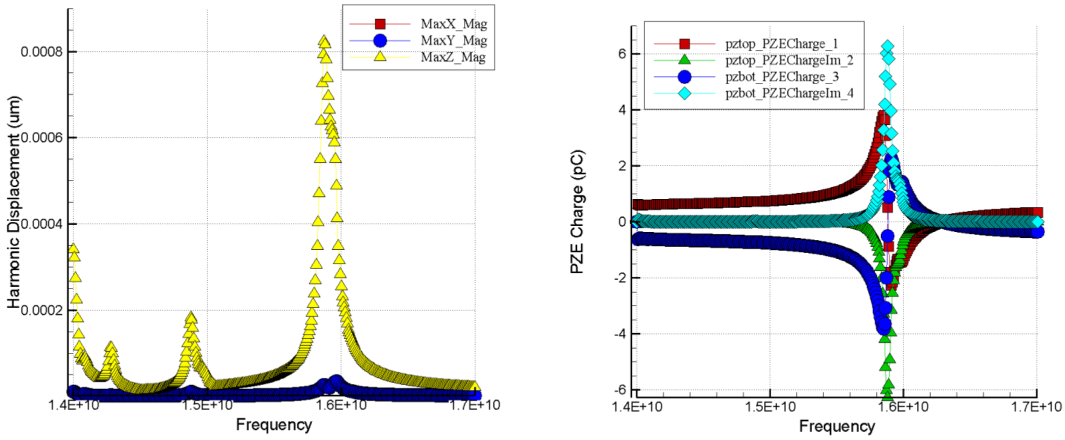

(a) (b)

Figure 5.19 Characteristics of Series Ku-band FBAR

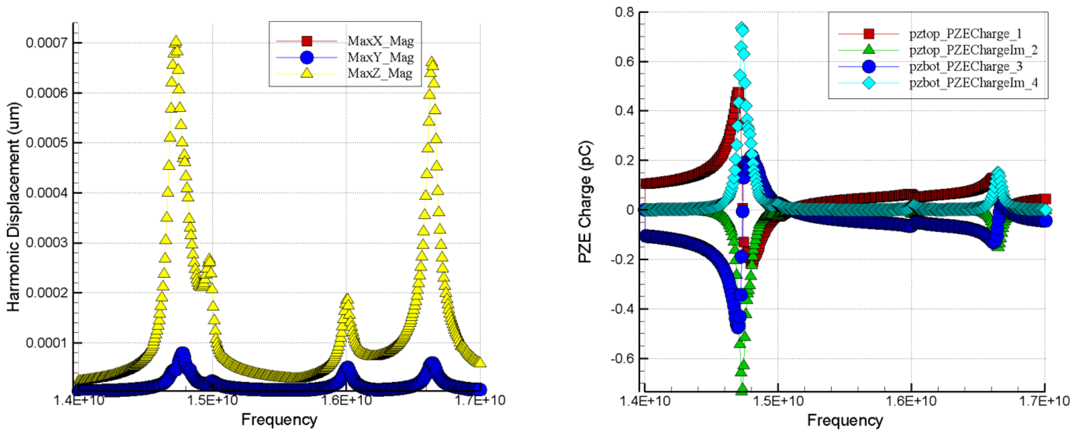

(a) (b)

Figure 5.20 Characteristics of Shunt Ku-band FBAR

Finally, the electrical impedances of the FBARs are illustrated in Figure 5.21. From the graphs, the f_p of both FBARs is determined. The Z_s and Z_p of both FBARs can also be extracted from the graphs.

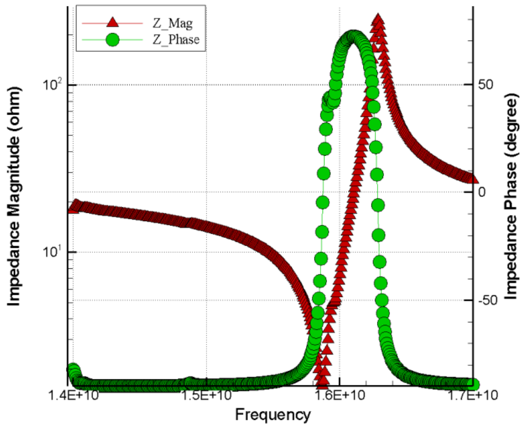

(a) series

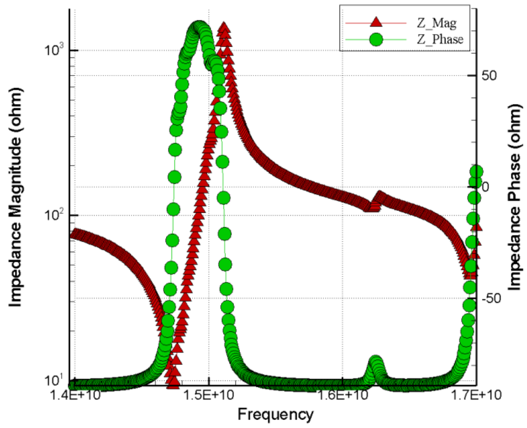

(b) shunt

Figure 5.21 Electrical Impedance of Ku-band FBARs

Table 5.7 and Table 5.8 summarise the FBAR parameters attained in the analysis. It was observed from Table 5.7 and Table 5.8 that the f_s and f_p of the FBARs are close to each other. From the analysis, only the series FBAR (a) and (b) and the shunt FBAR (a) and (b) are considered in this study. This is due to their wider bandwidths compared to the series FBAR (c) and shunt FBAR (c).

Table 5.7 Series FBAR Parameters

AlN (nm)	**Ru (nm)**	t_m/t_p	f_s **(GHz)**	f_p **(GHz)**	***BW* (GHz)**
(a) 205	21	0.10	15.89	16.32	0.43
(b) 185	25	0.14	15.87	16.29	0.42
(c) 162	30	0.19	15.91	16.32	0.41

Table 5.8 Parallel (Shunt) FBAR Parameters

AlN (nm)	**Ru (nm)**	t_m/t_p	f_s **(GHz)**	f_p **(GHz)**	***BW* (GHz)**
(a) 209	25	0.12	14.72	15.12	0.40
(b) 205	26	0.13	14.67	15.07	0.40
(c) 185	30	0.16	14.74	15.11	0.37

5.5.2 Optimisation of Active Area

As mentioned before, by designing an appropriate resonance area, the impedance matching of the FBAR can be achieved. It also has been shown that the area size has no significant effect on the f_s, f_p and Q factor. However, the area of the FBAR has a significant effect on the C_0. By referring to the values of C_0 given in Table 4.6, the area of the FBAR is calculated using equation 3.17. The results from the analysis are summarised in Table 5.9 and Table 5.10. It is observed that the values of C_0 of the FBARs from this analysis are very close to the C_0 reported in Table 4.6.

Table 5.9 FBAR Design Parameters for Filter A

FBAR	C_0 (pF)	AlN		Ru	
		t (nm)	Area (μm²)	t (nm)	Area (μm²)
Series (a)	0.6915	205	2.35×10^{-3}	21	1.48×10^{-3}
Series (b)	0.6837	185	2.21×10^{-3}	25	1.34×10^{-3}
Shunt (a)	0.0737	209	4.67×10^{-4}	25	1.35×10^{-4}
Shunt (b)	0.0651	205	4.62×10^{-4}	26	1.32×10^{-4}

Table 5.10 FBAR Design Parameters for Filter B

FBAR	C_0 (pF)	AlN		Ru	
		t (nm)	Area (μm²)	t (nm)	Area (μm²)
Series (a)	0.4855	205	1.75×10^{-3}	21	1.01×10^{-3}
Series (b)	0.4712	185	1.62×10^{-3}	25	9.12×10^{-4}
Shunt (a)	0.1053	209	5.79×10^{-4}	25	1.98×10^{-4}
Shunt (b)	0.1073	205	5.76×10^{-4}	26	1.94×10^{-4}

The detailed discussion on the Ku-band FBAR optimisation results will be presented in chapter 6.

5.6 Conclusion

This chapter presented the design and analysis of FBAR using 3-D FEM. The influence of various geometrical parameters and material losses on FBAR performance were analysed and explored in detail to find suitable solutions for designing a Ku-band FBAR with a high *Q* factor and wide bandwidth. The results confirm that the k^2_{eff} of the FBAR are solely influenced by the thickness of the piezoelectric film and electrode layers. Furthermore, the analysis also proved that Ru is an excellent material for FBAR electrodes as higher k^2_{eff} has been achieved. It is also shown that the width and length of the FBAR have no significant effect on the series frequency, parallel frequency, k^2_{eff} and *Q* factor of the FBAR. The estimation of material damping coefficients (α and β) using the Akhieser approximation is carried out to estimate more accurate values of the coefficients, thus a more realistic value of the *Q* factor is achieved. The calculated value of β is 3.84e^{-14} s. A *Q* factor of 300 has been achieved for the Ku-band FBAR. The study confirmed that the major loss of the FBAR is due to the material damping that caused significant changes in the value of the *Q* factor, while TED only contributes a small percentage of the overall losses. Based on the analysis, it is possible to specify the appropriate values of geometrical parameters that can be selected to achieve higher k^2_{eff} in designing the Ku-band FBAR. This chapter also presented the optimisation of the proposed Ku-band FBAR. The Ku-band FBAR has been designed with the optimum thickness ratio of electrode to the piezoelectric material to achieve a maximum value of k^2_{eff}. A detailed analysis of a Ku-band FBAR filter implementation using the optimised Ku-band FBAR will be discussed in the next chapter.

CHAPTER 6 : RESULTS AND ANALYSIS OF KU-BAND FBAR FILTER

6.1 Introduction

This chapter presents the optimisation and analysis of the proposed Ku-band Film Bulk Acoustic Wave Resonator (FBAR). The results of the optimisation are summarised and compared with other FBARs from the literature survey. This chapter also presents the design of the Ku-band FBAR filter implemented with the optimised Ku-band FBAR. This Ku-band FBAR filter will be characterised with respect to bandwidth at -3dB (BW_{-3dB}), insertion loss (I_L) and out-of-band (*OoB*) rejection. The performance of the designed Ku-band FBAR filter is compared to the Ku-band FBAR filter designed using the 1-D modelling described in Chapter 4. Finally, the results from the analysis are presented and compared to the results reported in the literature.

6.2 Results of Optimised Ku-band FBAR

The performance of the Ku-band FBAR is improved by optimising the geometrical parameters such as the t_m/t_p and the size of area (WxL) to meet the requirements for the Ku-band FBAR filter. The optimisation analysis demonstrates that the value of material damping coefficients (a and β) calculated from the Akhieser approximation based on the AlN material properties results in more accurate Q factors. The material loss of the FBAR can be largely attributed to β, which relates to the stiffness of the AlN. An increased value of β will lower the Q factor. A Q factor up to 300 has been achieved for the Ku-band FBARs.

Table 6.1 and Table 6.2 show the results of the optimised Ku-band FBAR. It has been shown that an optimum t_m/t_p will result in the highest k^2_{eff} up to 6.51%. However, in terms of the bandwidths, k^2_{eff} has no significant influence as the values of t_m/t_p of the FBAR are close to each other, being from 0.10 to 0.15 in this research. Therefore, it showed a slight difference on the bandwidths of the FBAR. Similarly, the f_s and f_p of the FBARs are close to each other. Further, it is found that area size influences the C_0 of the Ku-band FBAR, where C_0 is related to impedance matching. Area size is a critical parameter in designing the FBAR filter, thus optimisation is crucial.

Table 6.1 Optimised Series FBAR Parameters

AlN (nm)	**Ru (nm)**	t_m/t_p	f_s **(GHz)**	f_p **(GHz)**	k^2_{eff} **(%)**	***BW*** **(GHz)**	Q_s	Q_p
(a) 205	21	0.10	15.89	16.32	6.47	0.43	263.26	284.29
(b) 185	25	0.14	15.87	16.29	6.36	0.42	265.98	287.91

Table 6.2 Optimised Parallel (Shunt) FBAR Parameters

AlN (nm)	**Ru (nm)**	t_m/t_p	f_s **(GHz)**	f_p **(GHz)**	k^2_{eff} **(%)**	***BW*** **(GHz)**	Q_s	Q_p
(a) 209	25	0.12	14.72	15.12	6.49	0.40	285.45	304.03
(b) 205	26	0.13	14.67	15.07	6.51	0.40	286.84	306.51

6.3 Comparisons of Ku-band FBAR

Table 6.3 and Table 6.4 summarise and compare the series and shunt FBAR A and FBAR B parameters obtained from the 1-D simulation described in Chapter 4 and the 3-D FEM analysis presented in Chapter 5. Again, the parameter values are highly similar.

Table 6.3 Comparison of FBAR Parameters for Filter A

FBAR (series) / **Parameter**	**1-D**	**3-D FEM (a)**	**3-D FEM (b)**
C_o (pF)	0.6872	0.6915	0.6837
C_m (pF)	0.0351	0.0377	0.0373
L_m (nH)	2.86	2.66	2.69
k^2_{eff} (%)	6.06	6.47	6.36
f_s (GHz)	15.90	15.89	15.87
f_p (GHz)	16.30	16.32	16.30

FBAR (shunt) / **Parameter**	**1-D**	**3-D FEM (a)**	**3-D FEM (b)**
C_o (pF)	0.0614	0.0737	0.0651
C_m (pF)	0.0379	0.0403	0.0357
L_m (nH)	34.616	28.971	32.897
k^2_{eff} (%)	6.54	6.49	6.51
f_s (GHz)	14.70	14.72	14.67
f_p (GHz)	15.10	15.12	15.12

Table 6.4 Comparison of FBAR Parameters for Filter B

FBAR (series) / **Parameter**	**1-D**	**3-D FEM (a)**	**3-D FEM (b)**
C_o (pF)	0.468	0.485	0.471
C_m (pF)	0.024	0.026	0.025
L_m (nH)	4.20	3.78	3.97
k^2_{eff} (%)	6.06	6.47	6.36
f_s (GHz)	15.90	15.89	15.87
f_p (GHz)	16.30	16.32	16.29

FBAR (shunt) / **Parameter**	**1-D**	**3-D FEM (a)**	**3-D FEM (b)**
C_o (pF)	0.0901	0.105	0.107
C_m (pF)	0.058	0.057	0.058
L_m (nH)	23.58	20.28	19.96
k^2_{eff} (%)	6.54	6.49	6.51
f_s (GHz)	14.70	14.72	14.67
f_p (GHz)	15.10	15.12	15.12

The comparison of the electrical impedance between the 1-D modelling and 3-D FEM is shown in Figure 6.1. The 1-D model assumes the FBAR is lossless, which is not the case. The figure shows that using the 3-D FEM, minor spurious modes occurred between f_s and f_p. The material damping coefficient, β causes the f_p peak to become flatter, which means the electrical impedance is lower. This is because in 3-D FEM, the losses from the piezoelectric material and the electrodes are considered. However, there is an insignificant effect on f_s and f_p.

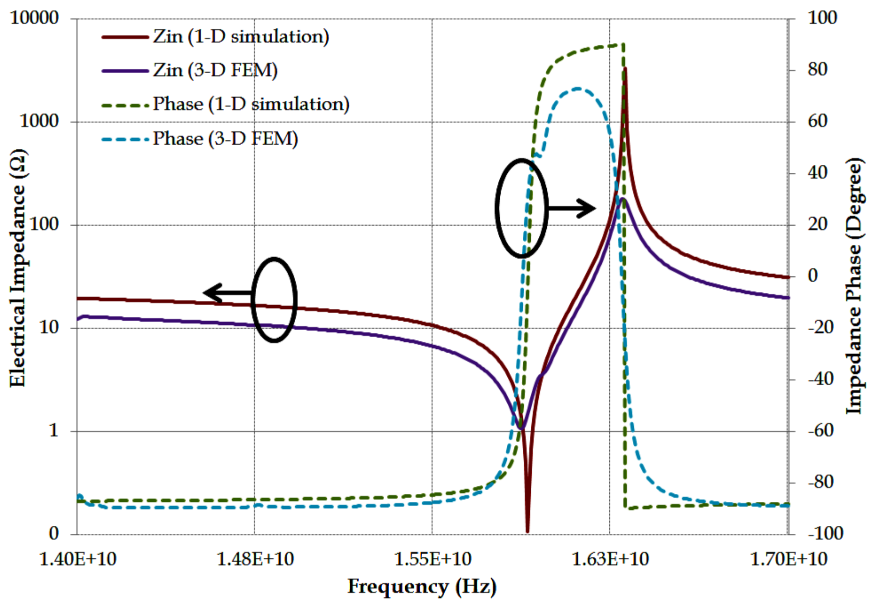

Figure 6.1 Comparison of Electrical Impedance of 1-D Simulation and 3-D FEM

There are differences between 1-D and 3-D FEM modelling in the Q factor analysis. The Q_s and Q_p calculated in 1-D using equation 3.14 are inflated because 1-D modelling does not take into account the influence of electrodes and other losses such as TED and material damping. When these losses are taken into account, it is observed that the Q factor reduces more than 50 times, as shown in Figure 6.2.

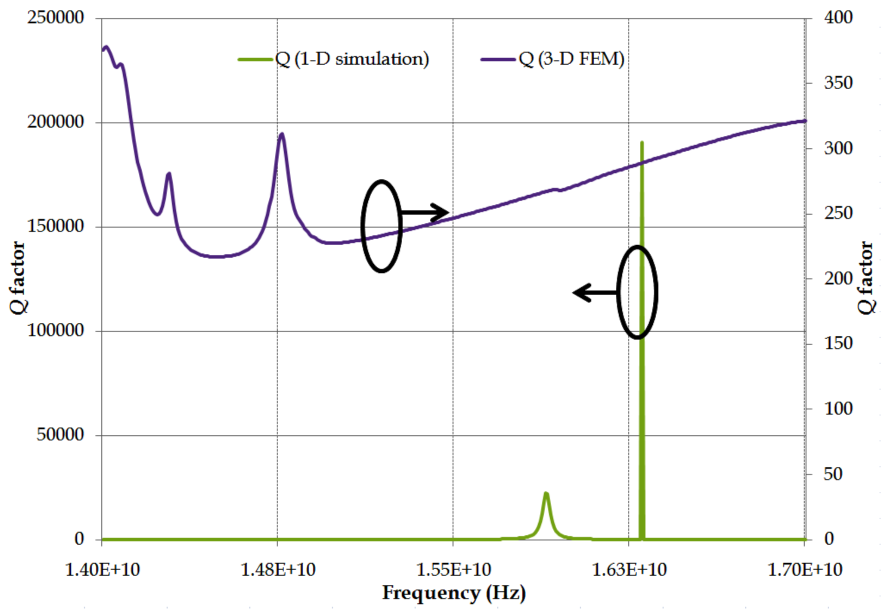

Figure 6.2 Comparison of *Q* Factor between 1-D Simulation and 3-D FEM

The performance of the Ku-band FBAR designed in this study is comparable to the other FBAR designs operating between 1 GHz to 20 GHz that have been reported in the literature. However, thus far, the only FBAR designed in Ku-band frequency range is from [80], as highlighted in Table 6.5. Compared to [80], the Ku-band FBAR described in this thesis has superior k^2_{eff}.

Table 6.5 Comparison of FBARs From The Literature and This Work

Reference	f_s **(GHz)**	f_p**(GHz)**	k^2_{eff} **(%)**	**BW (GHz)**	***Q***
[79]	19.8	19.998	6.25	0.198	189
[81]	9.025	9.3	6.40	0.225	247
[80]	5.08	5.24	6.20	0.16	900
	9.30	9.60	6.30	0.30	330
	13.75	14.25	6.00	0.50	300
[78]	5.21	5.47	7.00	0.26	329
[58]	5.17	5.31	6.40	0.14	913
[62]	5.10	5.25	4.70	0.15	700
	4.80	4.95	6.70	0.15	1000
[70]	3.69	3.71	1.06	0.02	1557
[76]	2.36	2.38	1.55	0.02	65
[75]	2.14	2.17	4.20	0.03	97
	2.09	2.13	4.90	0.04	64
[61]	2.18	2.19	1.50	0.01	332
[74]	1.85	1.91	6.59	0.06	1911
[73]	1.06	1.09	6.90	0.03	386
	1.10	1.13	7.84	0.03	159
This work					
FBAR series (a)	15.89	16.32	6.47	0.43	263
FBAR series (b)	15.87	16.29	6.36	0.42	266
FBAR shunt (a)	14.72	15.12	6.49	0.40	285
FBAR shunt (b)	14.67	15.07	6.51	0.40	286

6.4 Results and Analysis of Ku-Band FBAR Filter Utilising Optimised FBAR

This section presents the results and analysis of the Ku-band FBAR filter implemented with the FBAR designed and optimised as described in the previous chapter. The filters are designed using the transmission ABCD matrix by using the Z_s and Z_p obtained from the 3-D FEM. As shown in Table 6.6 and Table 6.7, there are two possible combinations to construct the FBAR Filter A and FBAR Filter B by using the series FBAR (a) and (b) and the shunt FBAR (a) and (b).

Table 6.6 FBAR Combinations for Filter A

FBAR	C_0 (pF)	Area (μm²)	f_s (GHz)	f_p (GHz)	BW (GHz)	k^2_{eff} (%)
(1)						
Series (b)	0.6837	1.34×10^{-3}	15.87	16.29	0.42	6.36
Shunt (a)	0.0737	1.35×10^{-4}	14.72	15.12	0.40	6.49
(2)						
Series (a)	0.6915	1.48×10^{-3}	15.89	16.32	0.43	6.47
Shunt (b)	0.0651	1.32×10^{-4}	14.67	15.07	0.40	6.51

Table 6.7 FBAR Combinations for Filter B

FBAR	C_0 (pF)	Area (μm²)	f_s (GHz)	f_p (GHz)	BW (GHz)	k^2_{eff} (%)
(1)						
Series (b)	0.4712	9.12×10^{-4}	15.87	16.29	0.42	6.36
Shunt (a)	0.1053	1.98×10^{-4}	14.72	15.12	0.40	6.49
(2)						
Series (a)	0.4855	1.01×10^{-3}	15.89	16.32	0.43	6.47
Shunt (b)	0.1073	1.94×10^{-4}	14.67	15.07	0.40	6.51

Figure 6.3 and Figure 6.4 show the electrical frequency response of the proposed Ku-band FBAR for Filter A using 3-D FEM. The designed Ku-band FBAR Filter A (1) and FBAR Filter A (2) utilising these FBARs based on the combinations given in Table 6.6 are depicted in Figure 6.5. The electrical frequency responses of the proposed Ku-band FBAR for Filter B using 3-D FEM are shown in Figure 6.6 and Figure 6.7. Based on the combinations given in Table 6.7, the designed Ku-band FBAR Filter B (1) and FBAR Filter B (2) using these FBARs are depicted in Figure 6.8.

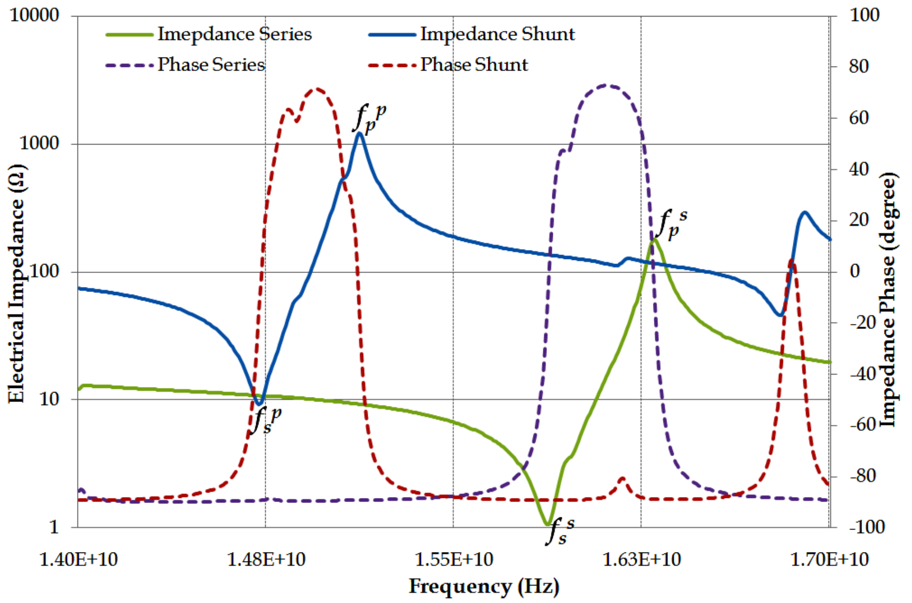

Figure 6.3 FBAR Electrical Impedances of Filter A (1)

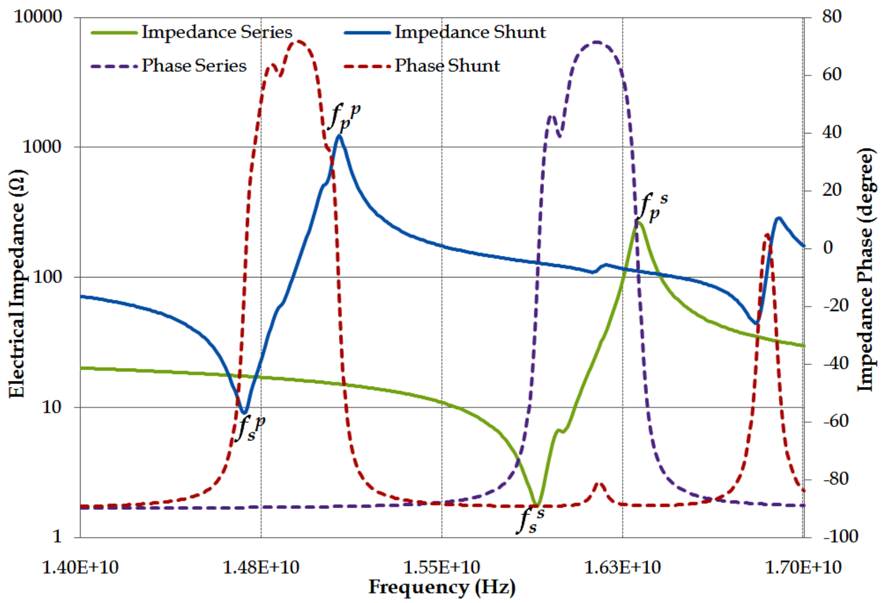

Figure 6.4 FBAR Electrical Impedances of Filter A (2)

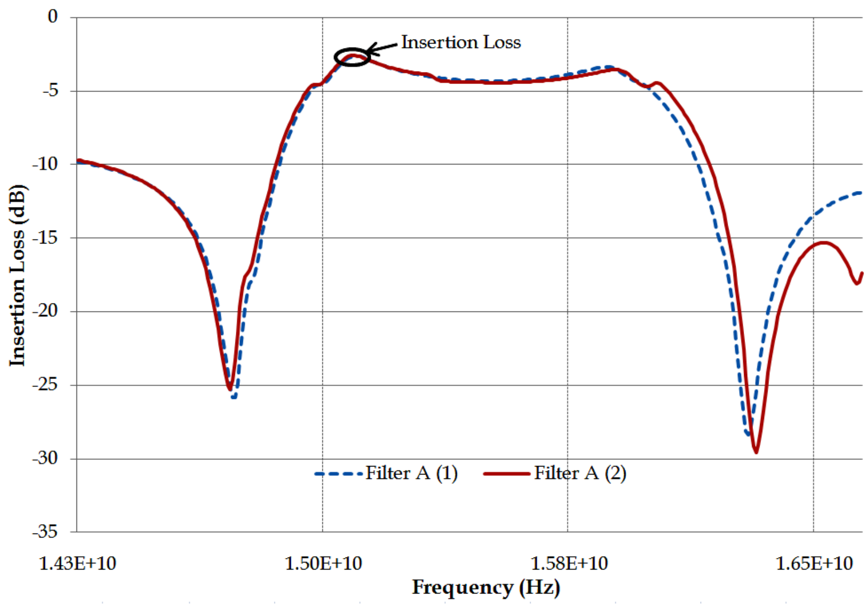

Figure 6.5 Transmission Response of FBAR Filter A at 6th Order

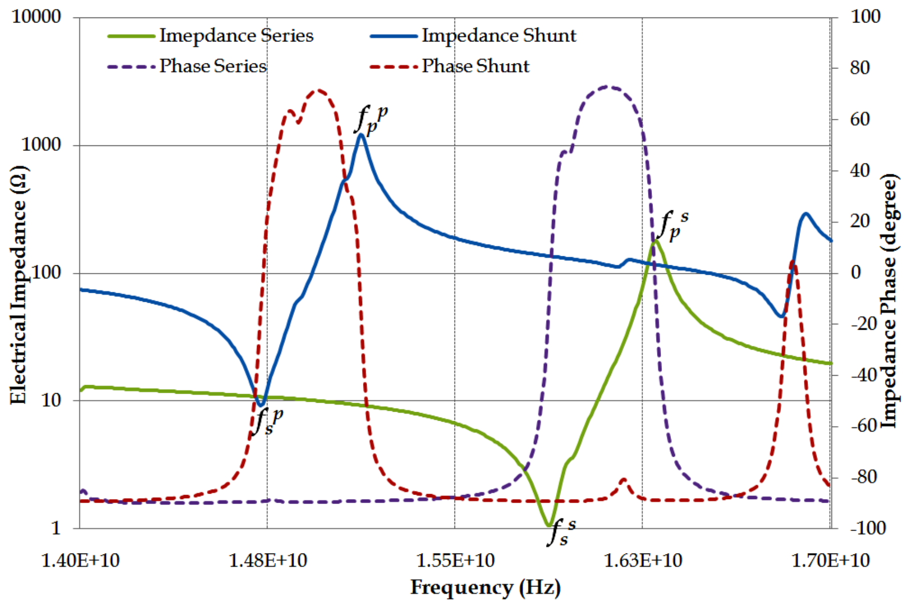

Figure 6.6 FBAR Electrical Impedances of Filter B (1)

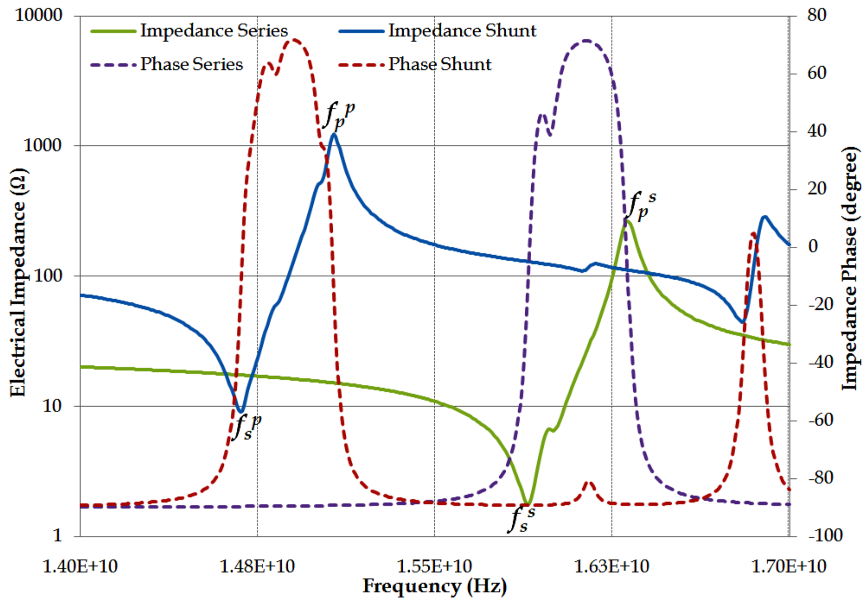

Figure 6.7 FBAR Electrical Impedances of Filter B (2)

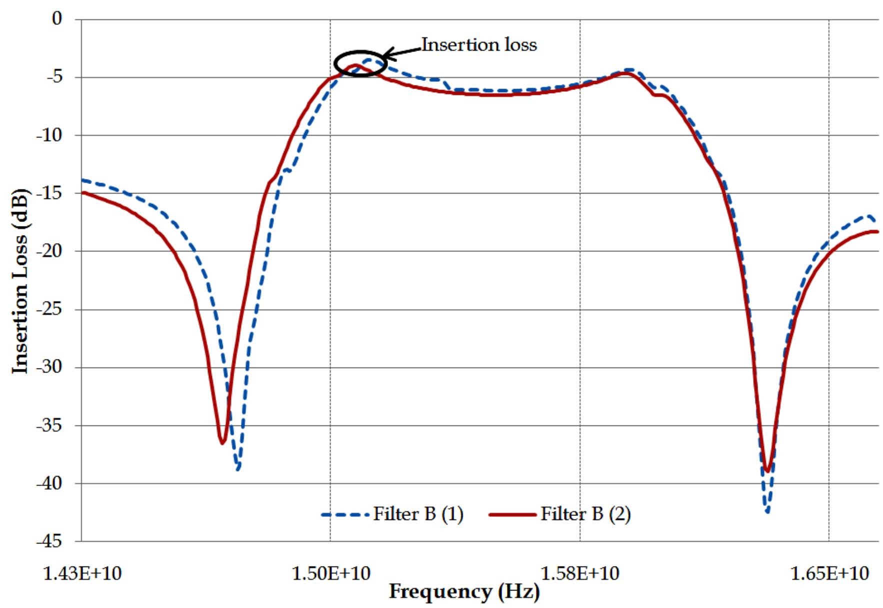

Figure 6.8 Transmission Response of FBAR Filter B at 6th Order

The characteristics of Ku-band FBAR filters using the FBAR designed in 3-D FEM are summarised in Table 6.8 and Table 6.9. For Filter A, at 8th order of Filter A (1) displays better I_L, OoB and BW_{-3dB} compared to the 8th order of Filter A (2). For Filter B, at 5th order, the Filter B (2) surpasses Filter B (1). At 6th order, Filter B (1) has a bandwidth of less than 1 GHz, which does not fulfil the requirements. Furthermore, also at 6th order, the I_L for Filter B (2) is -4.09 dB, and is thus too high. Generally, increases in the filter orders will lead to increases in *OoB* rejection, however; the I_L and BW_{-3dB} degrade. The analysis suggests that at specific filter orders, both Filter A and Filter B have achieved the target specifications. The 8th order filter A (1) is selected as the Ku-band FBAR filter.

Table 6.8 Characteristics of FBAR Filter A

Filter A (1)	***N*=2**	***N*=3**	***N*=4**	***N*=5**	***N*=6**	***N*=7**	***N*=8**
BW_{-3dB} (GHz)	1.35	1.28	1.19	1.18	1.13	1.12	1.09
I_L (dB)	-0.90	-1.36	-1.75	-2.43	-2.57	-3.22	-3.36
OoB (dB)	-3.01	-4.14	-5.99	-7.18	-8.95	-10.16	-11.90
Filter A (2)	***N*=2**	***N*=3**	***N*=4**	***N*=5**	***N*=6**	***N*=7**	***N*=8**
BW_{-3dB} (GHz)	1.31	1.23	1.16	1.13	1.07	1.06	1.05
I_L (dB)	-0.93	-1.33	-1.83	-2.58	-2.68	-3.34	-3.51
OoB (dB)	-3.01	-4.13	-5.99	-7.16	-8.94	-10.14	-11.88

Table 6.9 Characteristics of FBAR Filter B

Filter B (1)	***N*=2**	***N*=3**	***N*=4**	***N*=5**	***N*=6**
BW_{-3dB} (GHz)	1.22	1.14	1.07	1.04	0.99
I_L (dB)	-1.27	-1.75	-2.51	-3.19	-3.66
OoB (dB)	-4.27	-5.91	-8.50	-10.22	-12.71
Filter B (2)	***N*=2**	***N*=3**	***N*=4**	***N*=5**	***N*=6**
BW_{-3dB} (GHz)	1.31	1.21	1.51	1.10	1.06
I_L (dB)	-1.50	-1.93	-2.91	-3.47	-4.09
OoB (dB)	-4.56	-6.40	-9.21	-11.03	-13.67

6.5 Comparisons of the Ku-band FBAR Filter

Figure 6.9 shows the transmission response (S_{21}) of the 3rd-stage FBAR filter A (1) designed using the 1-D modelling and 3-D FEM. The results from both analyses match well within the pass-band. The attenuation poles of both filters also agree well. The disagreement on the suppression is due to piezoelectric material losses that were introduced in 3-D FEM. It can be concluded that the 1-

D modelling used in Chapter 4 can be applied to predict the characteristics of the FBAR filter.

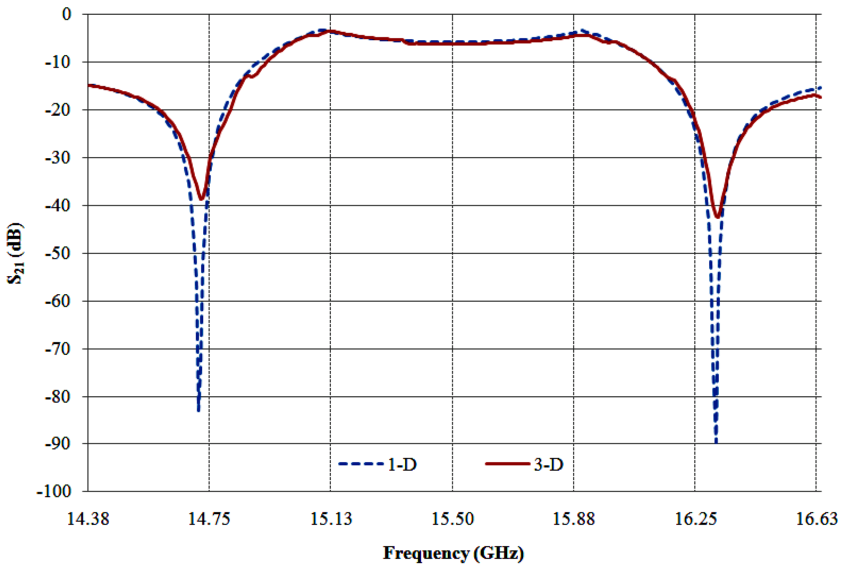

Figure 6.9 Comparison of FBAR Filter Transmission Response (S_{21}) between 1-D and 3-D FEM

Table 6.10 shows a comparison of FBAR filters operating in X-band to Ka band. All these filters were designed with a 4-stage ladder filter, which is equal to 8th order filter. The FBAR filters presented in this thesis have shown superior performance to those reported in [79], where the insertion loss is too high and the bandwidth is only 2%. To date, the FBAR filter designed in this thesis is the first FBAR filter ever reported operating in a Ku-band frequency range.

Table 6.11 shows a comparison of Ku-band FBAR filters designed in this work with other filters operating in Ku-band. All these filters were designed using different technology including DGS, interdigital and couple striplines. The comparison shows that the FBAR filter presented in this work has comparable performance to these other filters. Return loss of -10.55 dB is an acceptable value in filter application. However, the Ku-band FBAR filter designed in this work has the advantage of smaller area size and thus the size of the Ku-band transceiver can be reduced too.

Table 6.10 Comparison of FBAR Filters Characteristics

Reference	Centre Frequency (GHz)	Insertion Loss (dB)	Out-of-Band (GHz)	Bandwidth (GHz)	Filter Order
[4]	29.2 23.8	-3.80 -3.80	-11.0 -13.0	0.99 0.81	8th 8th
[81]	19.8	-4.10	-18.0	0.39	8th
[79]	9.08	-1.70	-21.0	0.28	8th
This work	15.5	-3.36	-11.9	1.09	8th

Table 6.11 Comparison of Ku-band Filter Characteristics

Characteristics / References	[21]	[21]	[8]	This work
Filter Design	DGS	Interdigital	Couple striplines	Filter A (1)
Centre Frequency (GHz)	14.7	15.5	14.527	15.5
Insertion Loss (dB)	-2.0	-1.5	-3.27	-3.36
Return Loss (dB)	-20	-15	-29.61	-10.55
Out-of-Band (dB)	--	--	--	-11.90
Bandwidth (GHz)	0.50	1.20	1.10	1.09
Size (mm^2)	--	--	5.5x3.8	0.58x0.15
Filter Order	2nd	--	--	8th

6.6 Conclusion

This chapter presented the results of the optimisation and analysis of the proposed Ku-band Film Bulk Acoustic Wave Resonator (FBAR). The Ku-band FBAR has been designed with the optimum thickness ratio of electrode to piezoelectric material to achieve a maximum value of k^2_{eff} of 6.47% for series FBARs and 6.51% for shunt FBARs. Therefore, FBARs with more than 1 GHz bandwidth are obtained. The designed Ku-band FBARs have Q_s of 263.26 and Q_p of 284.29 for series FBARs, and k^2_{eff} of 6.51%, Q_s of 286.84 and Q_p of 306.51 for shunt FBARs. The designed Ku-band FBAR filter using the optimised FBAR has a centre frequency of 15.5 GHz, insertion loss of -3.36 dB, out-of-band rejection of -11.90 dB and bandwidth of 1.09 GHz. These parameters render the present Ku-band FBAR filter superior to the other FBAR filters described in the literature. The designed Ku-band FBAR filter also features reduced size compared to other Ku-band filters while achieving acceptable performance. Therefore, the designed Ku-band FBAR filter is a suitable candidate to be implemented into the Ku-band transceiver.

CHAPTER 7 : CONCLUSION AND FUTURE WORK

7.1 Introduction

This chapter concludes the thesis, presents the future work that can be undertaken to enhance this work, and discusses the possible applications that can be implemented with the design. This chapter also discusses the major outcomes, limitation and assumptions of this research.

7.2 Major Outcomes

All the specific aims that were outlined in Chapter 1 have been achieved in this research. The major findings related to these specific aims are described below:

- To study the application of Ku-band transceivers;
  The detailed analysis of Ku-band transceiver architectures has been carried out to identify the key issues involved in achieving compact transceivers. Analysis shows that separately located modules and discrete components including filters are the causes of large and heavy weight Ku-band transceivers. Therefore, the need for a compact and low power consumption filter was found during this analysis.

- To study and investigate the design issues for Ku-band filters;
  The detailed analysis of various types of Ku-band filters was discussed. The analysis shows that these filters have wide bandwidths, which are more than 1 GHz. However, these filters have slow roll-off due to their low *Q* factor resonators. Another disadvantage of the current implemented Ku-band filters is they still require a large area. A better filter can be achieved by implementing a high *Q* factor resonator with minimum size. FBAR filters and FBAR diplexers have been developed for WiFi and WiMAX applications. These components have shown better

performance with reduce size and cost, due to a very high quality Q factor, good power handling and small size. This also can be achieved in Ku-band transceivers by implementing FBAR filters.

- To study and investigate the design issues for FBAR filters in frequencies more than 10 GHz;
  The analysis of FBAR filter design issues was presented to find proper solutions for designing a wide bandwidth FBAR filter in Ku-band. The resonance frequency of FBARs is determined by the thickness and phase velocity of the piezoelectric layer. Therefore, for FBARs operating at frequencies higher than 10 GHz, the thickness of the piezoelectric layer is in the hundred nanometre (nm) scale. AlN and Ru are chosen as the piezoelectric material and electrode due to their high acoustic velocity and high acoustic impedance, respectively. The air-gap type FBAR operating in Ku-band is designed using CoventorWare® 2010 and the optimisation of the geometrical parameters of the FBAR was fully analysed and discussed.

- To research and design a high Q factor and wide bandwidth FBAR for Ku-band;
  The air-gap type FBAR operating in Ku-band was proposed and was designed to achieve maximum k^2_{eff} and high Q. The design and analysis of the FBAR were performed using simple fabrication steps that were developed for air-gap type FBARs. The ratio electrode to piezoelectric material is used to estimate the value of k^2_{eff}. A maximum k^2_{eff} with high Q FBAR is achieved by optimising the geometrical parameters and losses from piezoelectric material and is used in designing the FBAR filter to improve the performance of the filter.

- To analyse the performance of FBAR filters using the newly designed FBAR;

The Ku-band FBAR filter using the proposed FBAR was analysed and discussed. The performance of the filter was discussed in detail.

7.3 Conclusion

All the specific aims of this research have been successfully achieved through the design of an air-gap FBAR. A wide bandwidth FBAR with a high Q factor that operates in Ku-band has been accomplished The influence of various geometrical parameters including the thickness, width and length of the piezoelectric film and electrode layers on the performance of FBARs is analysed to find suitable solutions for designing a wide bandwidth and high Q factor Ku -band FBAR. Analysis shows that the k^2_{eff} of the Ku-band FBAR can be improved by optimising the thickness ratio of electrode to the piezoelectric material (t_m/t_p). The optimum t_m/t_p is from 0.05 to 0.15 in order to achieve a maximum value of k^2_{eff} of the FBAR.

The material damping coefficients (α and β) of AlN are estimated using Akhieser approximation instead of using material properties of silicon to achieve more realistic value of Q factor. The values of α and β obtained are $1.55e^4$/s and $3.84e^{-14}$ s at 15 GHz respectively. The optimised Ku-band FBARs have achieved k^2_{eff} of 6.47%, Q_s of 263.26 and Q_p of 284.29 for series FBARs, and k^2_{eff} of 6.51%, Q_s of 286.84 and Q_p of 306.51 for shunt FBARs, resulting in an overall bandwidth of 430 MHz for series and 400 MHz for shunt FBARs.

Ku-band FBAR filter implemented with the optimised Ku-band FBARs are characterised by using the *ABCD* matrix method. The designed Ku-band FBAR filter has fulfilled all the target specifications. The FBAR filter has a centre frequency of 15.5 GHz operating from 15 GHz to 16 GHz, insertion loss of -3.36 dB, out-of-band rejection of -11.90 dB, bandwidth of 1.09 GHz and area size of 0.58 x 0.15 mm^2.

From this research, it is shown that the FBAR has good performance, reduced size and compatible with MMIC, CMOS and other standard IC manufacturing, which makes it a suitable candidate for implementation in a Ku-band transceiver system to achieve a compact, low cost and low power consumption transceiver.

7.4 Limitation and Assumptions

This research work was performed using the CoventorWare ® 2010 simulation tool. The static capacitance (C_0) computed with the assumption displacement is negligible. However, there is no significant difference in FBAR characteristics. This is because it is designed based on the C_0 obtained from 1-D modelling.

At frequencies higher than 10 GHz, the thickness of the AlN is less than 210 nm and the thickness of Ru is less than 26 nm. The fabrication of these thin films is a challenging task as they are prone to crack due to stress during the fabrication process.

7.5 Future Work

This work has presented a great understanding of the theoretical behaviour of the FBAR and its application to microwave filters. The Ku-band FBAR with wide bandwidth and a high *Q* factor will be a very important parameter in microwave applications. The suggested future work listed below can be applied in order to take advantages of the FBAR:

- The performance of Ku-band transceivers implemented with the Ku-band FBAR filter can be analysed, which is an essential step to further verify the advantage of the FBAR filter in achieving better performance in power consumption.

- This Ku-band FBAR can be implemented in the other transceiver circuits, such as in a voltage-controlled oscillator (VCO).

- Fabrication is a further step required to validate the performance of the FBAR obtained in this work.

APPENDIX A: MATLAB SYNTAX FOR ELECTRICAL IMPEDANCE OF FBAR USING EQUATION 4.5

1) Calculation of Z_s and Z_p for FBAR A

```
%------Calculation of Zs--------------
 Cos=0.68716e-12;
f1=14e9:0.0075e9:17e9;
fs1=15.9e9;
fp1=16.3e9;
n1=1./(1i*2*3.142*f1*Co1);
m1=f1.^2-fs1^2;
m21=f1.^2-fp1^2;
m31=m1./m21;

Z1=n1.*m31;
R1=abs (Z1);
R1_log=log (R1);
P1=-(180/3.142)*atan(Z1);

%--------Calculation of Zp-------------
Cop=0.061373e-12;
f2=14e9:0.0075e9:17e9;
fs2=14.7e9;
fp2=15.1e9;
n2=1./(2*3.142*f2*Co2);
m2=f2.^2-fs2^2;
m22=f2.^2-fp2^2;
m32=m2./m22;
```

```
Z2=n2.*m32;
R2=abs(Z2);
P2=-(180/3.142)*atan(Z2);

%-------------plot graphs------------
 figure (1),plotyy(f1,R1,f1,P1)
grid on
figure (2),plotyy(f2,R2,f2,P2)
grid on
```

2) Calculation of Z_s and Z_p for FBAR B

```
%------Calculation of Zs--------------
Cos=0.46813e-12;
f1=14e9:0.0075e9:17e9;
fs1=15.9e9;
fp1=16.3e9;
n1=1./(1i*2*3.142*f1*Co1);
m1=f1.^2-fs1^2;
m21=f1.^2-fp1^2;
m31=m1./m21;

Z1=n1.*m31;
R1=abs (Z1);
R1_log=log (R1);
P1=-(180/3.142)*atan(Z1);
```

```
%--------Calculation of Zp-------------

Cop=0.090089e-12;
f2=14e9:0.0075e9:17e9;
fs2=14.7e9;
fp2=15.1e9;
n2=1./(2*3.142*f2*Co2);
m2=f2.^2-fs2^2;
m22=f2.^2-fp2^2;
m32=m2./m22;

Z2=n2.*m32;
R2=abs(Z2);
P2=-(180/3.142)*atan(Z2);

%-------------plot graphs------------

figure (1),plotyy(f1,R1,f1,P1)
grid on
figure (2),plotyy(f2,R2,f2,P2)
grid on
```

APPENDIX B: MATLAB SYNTAX FOR ELECTRICAL IMPEDANCE OF FBAR USING EQUATION 3.16.

1) Calculation of Z_s and Z_p of FBAR A

```
%---------Calculation of Zs--------------
d=319e-9;v=10400;
Co=0.68716e-14;
k2eff=0.0606;
f=14e9:0.0075e9:17e9;

omega=2*pi*f;
k=omega/v;
a=k*d/2;
a_1= tan (a);
c=(a_1./a);

b=1-(k2eff*c);
Om_Co=(1i*omega*Co);
Op_om_co=1./Om_Co;

Z_in= Op_om_co.*b;
Zin_real=abs(Z_in);
Zin_imag=imag(Z_in);
Zin_phase=(180/3.142)*atan (Zin_imag);

%-------------plot graphs------------
plot (f,Zin_real);
ylabel('|Z|(Ohm)');
xlabel('Frequency (Hz)');
```

```
grid on

%------Calculation of Zp--------------
d=344e-9;v=10400;
Co=0.06137e-12;
k2eff=0.0654;
f=14e9:0.0075e9:17e9;

omega=2*pi*f;
k=omega/v;
a=k*d/2;
a_1= tan (a);
c=(a_1./a);

b=1-(k2eff*c);
Om_Co=(1i*omega*Co);
Op_om_co=1./Om_Co;

Z_in= Op_om_co.*b;
Zin_real=abs(Z_in);
Zin_imag=imag(Z_in);
Zin_phase=(180/3.142)*atan (Zin_imag);

%-------------plot graphs------------
plot (f,Zin_real);
ylabel('|Z|(Ohm)');
xlabel('Frequency (Hz)');
grid on
```

1) Calculation of Z_s and Z_p of FBAR B

```
%---------Calculation of Zs--------------
d=319e-9;v=10400;
Co=0.46813e-12;
k2eff=0.0606;
f=14e9:0.0075e9:17e9;

omega=2*pi*f;
k=omega/v;
a=k*d/2;
a_1= tan (a);
c=(a_1./a);

b=1-(k2eff*c);
Om_Co=(1i*omega*Co);
Op_om_co=1./Om_Co;

Z_in= Op_om_co.*b;
Zin_real=abs(Z_in);
Zin_imag=imag(Z_in);
Zin_phase=(180/3.142)*atan (Zin_imag);

%-------------plot graphs------------
plot (f,Zin_real);
ylabel('|Z|(Ohm)');
xlabel('Frequency (Hz)');
grid on

%------Calculation of Zp--------------
d=344e-9;v=10400;
Co=0.090089e-12;
```

```
k2eff=0.0654;
f=14e9:0.0075e9:17e9;

omega=2*pi*f;
k=omega/v;
a=k*d/2;
a_1= tan (a);
c=(a_1./a);

b=1-(k2eff*c);
Om_Co=(1i*omega*Co);
Op_om_co=1./Om_Co;

Z_in= Op_om_co.*b;
Zin_real=abs(Z_in);
Zin_imag=imag(Z_in);
Zin_phase=(180/3.142)*atan (Zin_imag);

%-------------plot graphs------------
plot (f,Zin_real);
ylabel('|Z|(Ohm)');
xlabel('Frequency (Hz)');
grid on
```

BIBLIOGRAPHY

[1] M. M. Tentzeris, "Multilayer (3D) Wireless, RF and Millimeter-Wave Passives and Modules Using SOP Technology," *Topical Meeting on Silicon Monolithic Integrated Circuits in RF Systems,* pp. 181-182, 2007.

[2] K. M. Lakin, "Thin Film Resonators and Filters," *Proceedings IEEE Ultrasonics Symposium*, pp. 895-906 1999.

[3] R. Ruby, P. Bradley, J. Larson, III, *et al.*, "Ultra-Miniature High-Q Filters and Duplexers using FBAR Technology," *Digest of Technical Papers IEEE International Solid-State Circuits Conference,* pp. 120-121, 2001.

[4] M. Hara, T. Yokoyama, T. Sakashita, *et al.*, "A Study of The Thin Film Bulk Acoustic Resonator Filters in Several Ten GHz Band," *IEEE International Ultrasonics Symposium*, pp. 851-854, 2009.

[5] "IEEE Standard Letter Designations for Radar-Frequency Bands," *IEEE Std 521-2002 (Revision of IEEE Std 521-1984),* pp. 1-3, 2003.

[6] R. Gilmore, C. Bruckner, and D. Dunn, "Ku-Band MMIC Transceiver for Mobile Satellite Communications," *21st European Microwave Conference,* pp. 1261-1265, 1991.

[7] K. Morrison, H. Rott, T. Nagler, *et al.*, "The SARALPS-2007 measurement campaign on Xand Ku-Band Backscatter of snow," *IEEE International Geoscience and Remote Sensing Symposium (IGARSS),* pp. 1207-1210, 2007.

[8] J. Jianhua, L. Yinqiao, H. Sha, *et al.*, "A compact LTCC Transmit Receive Module at Ku-band," *International Conference onMicrowave and Millimeter Wave Technology,* pp. 1239-1241, 2010.

[9] C.-H. Lee, Joy Laskar, *Compact Ku-band Transmitter Design for Satellite Communication Applications : From System Analysis to Hardware Implementation,* London: Kluwer Academic Publishers, 2002.

[10] E. R. Brown, E. B. Brown, and A. Hartenstein, "Ku-band Retrodirective Radar for Ballistic Projectile Detection and Tracking," *IEEE Radar Conference*, pp. 1-4, 2009.

[11] J. B. Shealy, T. Jackson, A. Rachlin, *et al.*, "A 2 watt Ku-band Linear (multi-carrier) Transmit Module for VSAT Applications," *IEEE MTT-S International Microwave Symposium Digest,* pp. 1055-1058 1999.

[12] L. Chang-Ho, A. Sutono, H. Sangwoo, *et al.*, "A Compact LTCC-based Ku-band Transmitter Module," *IEEE Transactions on Advanced Packaging,* vol. 25, pp. 374-384, 2002.

[13] W. J. Donnelly, J. R. Carswell, R. E. McIntosh, *et al.*, "Revised Ocean Backscatter Models at C and Ku band Under High-Wind Conditions," *Journal of Geophysical Research: Oceans,* vol. 104, pp. 11485-11497, 1999.

[14] S. Yuen, D. Cline, and K. Elder, "Airborne Ku-band Radar Remote Sensing of Terrestrial Snow Cover," *Geoscience and Remote Sensing Symposium, 2007. IGARSS 2007. IEEE International*, pp. 1211-1214, 2007.

[15] K.-y. Hashimoto, *RF Bulk Acoustic Wave Filters for Communications*: Artech House, 2009.

[16] L. Mang, E. Hickernell, R. Pennell, *et al.*, "Thin-Film Resonator Ladder Filter," *IEEE International Microwave Symposium Digest,* vol.2, pp. 887-890 1995.

[17] T. Mega, K. Monden, T. Ushio, *et al.*, "A Low-Power High-Resolution Broad-Band Radar Using A Pulse Compression Technique for Meteorological Application," *Geoscience and Remote Sensing Letters, IEEE,* vol. 4, pp. 392-396, 2007.

[18] Z. Zhuo, Z. Guoqiang, Z. Xingyao, *et al.*, "A Transceiver for Ku band Digital Monopulse Radar System," *International Conference on Microwave and Millimeter Wave Technology*, pp. 979-982, 2010.

[19] J. V. Evans, "Proposed U.S. Global Satellite Systems Operating at Ka-Band," *IEEEAerospace Conference*, vol.4, pp. 525-537 1998.

[20] G. Maral, *VSAT Networks*. West Sussex: John Wiley & Sons Ltd, 2003.

[21] H. Su, M. Xing, Y. Li, *et al.*, "Design of a Front-end of a Ku-band Transceiver Based on LTCC Technology," *11th International Conference on Electronic Packaging Technology & High Density Packaging,* pp. 851-855, 2010.

[22] R. R. Tummala, "SOP: What Is It and Why? A New Microsystem-Integration Technology Paradigm-Moore's Law for System Integration of Miniaturized Convergent Systems of the Next Decade," *Advanced Packaging, IEEE Transactions on,* vol. 27, pp. 241-249, 2004.

[23] R. Aigner, "MEMS in RF-Filter Applications: Thin Film Bulk Acoustic Wave Technology," *The 13th International Conference on Solid-State Sensors, Actuators and Microsystems, Digest of Technical Papers*, pp. 5-8 2005.

[24] E. Kerherve, P. Ancey, M. Aid, *et al.*, "4D-5 BAW Technologies: Development and Applications within MARTINA, MIMOSA and MOBILIS IST European Projects (Invited)," *IEEE Ultrasonics Symposium*, pp. 341-350, 2006.

[25] L. Wing-Yan, K. K. M. Cheng, and W. Ke-Li, "Multilayer LTCC Bandpass Filter Design with Enhanced Stopband Characteristics," *IEEE Microwave and Wireless Components Letters,* vol. 12, pp. 240-242, 2002.

[26] Z. Ge, "A Downsized and Integrated C-band Transceiver for VSAT," *Microwave and Optoelectronics Conference Proceedings*, pp. 33-36 1995.

[27] B. Yassini, Y. Ming, D. Smith, *et al.*, "A Ku-Band High-Q Tunable Filter With Stable Tuning Response," *IEEE Transactions on Microwave Theory and Techniques,* vol. 57, pp. 2948-2957, 2009.

[28] I. C. Reines, C. L. Goldsmith, C. D. Nordquist, *et al.*, "A Low Loss RF MEMS Ku-band Integrated Switched Filter Bank," *IEEE Microwave and Wireless Components Letters,* vol. 15, pp. 74-76, 2005.

[29] A. Bunin, V. Gevorkyan, Y. Kazantsev, *et al.*, "Resonant Section for Ku-band High-Power Bandpass Filter," *IEEE Region 8 International Conference on Computational Technologies in Electrical and Electronics Engineering,* pp. 549-551, 2010.

[30] M. Min, B. Jingpeng, W. Yafei, *et al.*, "A Bulk Micromachined Tunable Dual-Mode Ku-band Bandpass Filter," *9th International Conference on Solid-State and Integrated-Circuit Technology,* pp. 2480-2483, 2008.

[31] K. Entesari, T. Vaha-Heikkila, and G. M. Rebeiz, "Miniaturized Differential Filters for C- and Ku-band Applications," *33rd European Microwave Conference* pp. 227-229 2003.

[32] H. Campanella, *Acoustic Wave and Electromechanical Resonators*: Artech House 2010.

[33] B. Pillans, G. Rebeiz, and J. B. Lee, "Advances in RF MEMS Technology," *25th IEEE Annual Symposium on Technical Digest Gallium Arsenide Integrated Circuit (GaAs IC),* pp. 17-20, 2003.

[34] G. Lingpeng, J. K. O. Sin, L. Haitao, *et al.*, "Fully Integrated CMOS and High Voltage Compatible RF MEMS Technology," *Technical Digest IEEE International Electron Devices Meeting*, pp. 35-38, 2004.

[35] P. Gammel, G. Fischer, and J. Bouchaud, "RF MEMS and NEMS Technology, Devices and Applications," *Bell Labs Technical Journal,* vol. 10, pp. 29-59, 2005.

[36] F. Coccetti, D. Peyrou, M. Al Ahmad, *et al.*, "RF MEMS Status and Perspectives," *physica status solidi (c),* vol. 5, pp. 3822-3827, 2008.

[37] C. T. C. Nguyen, "RF MEMS in Wireless Architectures," *Proceedings. 42nd Design Automation Conference,* pp. 416-420, 2005.

[38] W. Kun, W. Ark-Chew, and C. T. C. Nguyen, "VHF Free-Free Beam High-Q Micromechanical Resonators," *Journal of Microelectromechanical Systems,* vol. 9, pp. 347-360, 2000.

[39] M. A. Abdelmoneum, M. U. Demirci, and C. T. C. Nguyen, "Stemless Wine-Glass-Mode Disk Micromechanical Resonators," *The Sixteenth Annual IEEE International Conference on Micro Electro Mechanical Systems*, pp. 698-701, 2003.

[40] M. Rinaldi, C. Zuniga, and G. Piazza, "5-10 GHz AlN Contour-Mode Nanoelectromechanical Resonators," *IEEE 22nd International Conference on Micro Electro Mechanical Systems (MEMS),* pp. 916-919, 2009.

[41] S. Bauerdick, A. Linden, C. Stampfer, et al., "Direct Wiring of Carbon Nanotubes for Integration in Nanoelectromechanical Systems," Journal of Vacuum Science & Technology B: Microelectronics and Nanometer Structures, vol. 24, pp. 3144-3147, 2006.

[42] A. Husain, Hone, J., Postma, H. W. C., Huang, X. M. H., Drake, T.,Barbic, M Laden, Scherer, Axel and Roukes, M. L., "Nanowire-Based Very-High-Frequency Electromechanical Resonators," *Applied Physics Letter,* vol. 83, pp. 1240-1242, 2003.

[43] G. A. Ozin, A. C. Arsenault, and L. Cademartiri, *Nanochemistry: A Chemical Approach to Nanomaterials*: Royal Society of Chemistry, 2008.

[44] G. D. Bachand and C. D. Montemagno, "Constructing Organic/Inorganic NEMS Devices Powered by Biomolecular Motors," *Biomedical Microdevices,* vol. 2, pp. 179-184, 2000.

[45] A. Zaki, H. Elsimary, and M. Zaghloul, "Miniature SAW Device for RF-Wireless Applications Using MEMS Technology," *49th IEEE International Midwest Symposium on Circuits and Systems*, pp. 109-112, 2006.

[46] C. C. W. Ruppel, L. Reindl, and R. Weigel, "SAW Devices and Their Wireless Communications Applications," *IEEE Microwave Magazine,* vol. 3, pp. 65-71, 2002.

[47] A. Muller, G. Konstantinidis, D. Neculoiu, *et al.*, "SAW and FBAR Resonators for GHZ Applications Based on Micromachining and Nanoprocessing of Wide Bandgap Semiconductors," *IEEE 25th Convention of Electrical and Electronics Engineers,* pp. 571-574, 2008.

[48] K.-W. Tay, P.-H. Sung, Y.-C. Lin, *et al.*, "Characteristics of ZnO Thin Film for Film Bulk Acoustic-Wave Resonators," *Journal of Electroceramics,* vol. 21, pp. 178-183, 2008.

[49] G. F. Perez-Sanchez and A. Morales-Acevedo, "Design of bulk acoustic wave resonators based on ZnO for filter applications," *6th International Conference on Electrical Engineering, Computing Science and Automatic Control*, pp. 1-6, 2009.

[50] L. Mai, V.-S. Pham, and G. Yoon, "ZnO-based Film Bulk Acoustic Resonator Devices on a Specially Designed Bragg Reflector," *Applied Physics A: Materials Science & Processing,* vol. 95, pp. 667-671, 2009.

[51] Y. Yoshino, "Piezoelectric Thin Films and Their Applications for Electronics," *Journal of Applied Physics,* vol. 105, pp. 061623-7, 2009.

[52] A. Muller, G. Konstantinidis, D. Neculoiu, *et al.*, "SAW and FBAR Resonators for GHz Applications based on Micromachining and Nanoprocessing of Wide Bandgap Semiconductors," *IEEE 25th Convention of Electrical and Electronics Engineers,* pp. 571-574, 2008.

[53] Y. Satoh, O. Ikata, T. Miyashita, *et al.*, "RF SAW Filters," *International Symposium on Acoustic Wave Devices for Future Mobile Communication Systems*, pp. 125-132, 2001.

[54] W. Kun, M. Frank, P. Bradley, *et al.*, "FBAR Rx Filters for Handset Front-End Modules with Wafer-Level Packaging," *IEEE Symposium on Ultrasonics,* vol.1, pp. 162-165 2003.

[55] S. Taniguchi, T. Yokoyama, M. Iwaki, *et al.*, " An Air-Gap Type FBAR Filter Fabricated Using a Thin Sacrificed Layer on A Flat Substrate," *IEEE Ultrasonics Symposium,* pp. 600-603, 2007.

[56] H. P. Loebl, C. Metzmacher, D. N. Peligrad, *et al.*, "Solidly Mounted Bulk Acoustic Wave Filters for the GHz Frequency Range," *Proceedings IEEE Ultrasonics Symposium,* pp. 919-923 vol.1, 2002.

[57] R. Ruby, "Review and Comparison of Bulk Acoustic Wave FBAR, SMR Technology," *IEEE Ultrasonics Symposium,* pp. 1029-1040, 2007.

[58] T. Nishihara, T. Yokoyama, T. Miyashita, *et al.*, "High Performance and Miniature Thin Film Bulk Acoustic Wave Filters for 5 GHz," *Proceedings IEEE Ultrasonics Symposium*, pp. 969-972, 2002.

[59] J. V. Tirado, "Bulk Acoustic Wave Resonators and Their Application to Microwave Devices," PhD, Universitat Antonoma de Barcelona, 2010.

[60] H. P. Loebl, M. Klee, C. Metzmacher, *et al.*, "Piezoelectric Thin AlN Films for Bulk Acoustic Wave (BAW) Resonators," *Materials Chemistry and Physics,* vol. 79, pp. 143-146, 2003.

[61] W.-K. Liu, K.-W. Tay, S.-C. Kuo, *et al.*, "Fabrication of piezoelectric AlN thin film for FBARs," *Science in China Series G: Physics Mechanics and Astronomy,* vol. 52, pp. 226-232, 2009.

[62] R. Kubo, H. Fujii, H. Kawamura, *et al.*, "Fabrication of 5GHz Band Film Bulk Acoustic Wave Resonators Using ZnO Thin Film," *IEEE Symposium on Ultrasonics,* vol.1, pp. 166-169 2003.

[63] Q. X. Su, P. Kirby, E. Komuro, *et al.*, "Thin-Film Bulk Acoustic Resonators and Filters Using ZnO and Lead-Zirconium-Titanate Thin Films," *IEEE Transactions on Microwave Theory and Techniques,* vol. 49, pp. 769-778, 2001.

[64] E. K. Kim, T. Y. Lee, Y. H. Jeong, *et al.*, "Air Gap Type Thin Film Bulk Acoustic Resonator Fabrication Using Simplified Process," *Thin Solid Films,* vol. 496, pp. 653-657, 2006.

[65] J. G. Gualtieri, J. A. Kosinski, and A. Ballato, "Piezoelectric Materials for Acoustic Wave Applications," *IEEE Transactions on Ultrasonics, Ferroelectrics and Frequency Control,* vol. 41, pp. 53-59, 1994.

[66] R. LANZ, "Piezoelectric Thin Films for Bulk Acoustic Wave Resonator Applications: From Processing to Microwave Filters," PhD, ÉCOLE POLYTECHNIQUE FÉDÉRALE DE LAUSANNE, Lausanne, 2004.

[67] R. Aigner, "MEMS in RF Filter Applications: Thin-film Bulk Acoustic Wave Technology," *Sensors Update,* vol. 12, pp. 175-210, 2003.

[68] R. Lanz and P. Muralt, "Solidly mounted BAW filters for 8 GHz based on AlN thin films," *IEEE Symposium on Ultrasonics*, pp. 178-181, 2003.

[69] P. Bradley, J. Kim, S. Ye, *et al.*, " 2X Size and Cost Reduction of Film Bulk Acoustic Resonator (FBAR) Chips with Tungsten Electrodes for PCS/GPS/800 MHz Multiplexers," *IEEE Ultrasonics Symposium*, pp. 1144-1147, 2007.

[70] Y. Aota, Y. Sakyu, S. Tanifuji, *et al.*, "Fabrication of FBAR for GHz Band Pass Filter with AlN Film Grown Using MOCVD," *IEEE Symposium on Ultrasonics,* pp. 337-340, 2006.

[71] K. Yong-Dae, S. Kuk-Hyun, S. Sang-Chul, *et al.*, "Highly Miniaturized RF Bandpass Filter Based on Thin-Film Bulk Acoustic-Wave Resonator for 5-GHz-band Application," *IEEE Transactions on Microwave Theory and Techniques,* vol. 54, pp. 1218-1228, 2006.

[72] M. Hara, T. Yokoyama, T. Sakashita, *et al.*, "Super-High-Frequency Band Filters Configured with Air-Gap-Type Thin-Film Bulk Acoustic Resonators," *Japanese Journal of Applied Physics,* vol. 49, pp. 07HD13-07HD13-4, 2010.

[73] M. Ylilammi, J. Ella, M. Partanen, *et al.*, "Thin Film Bulk Acoustic Wave Filter," *IEEE Transactions on Ultrasonics, Ferroelectrics and Frequency Control,* vol. 49, pp. 535-539, 2002.

[74] Y. P. Kuangwoo NAM, Byeoungju HA, Dongha SHIM and Insang Song, "Piezoelectric Properties of Aluminum Nitride for Thin Film Bulk

Acoustic Wave Resonator," *Journal of the Korean Physical Society,* vol. 47, pp. S309-S312, 2005.

[75] Z. Xinen, V. Lee, J. Phillips*, et al.*, "An Intrinsically Switchable FBAR Filter Based on Barium Titanate Thin Films," *IEEE Microwave and Wireless Components Letters,* vol. 19, pp. 359-361, 2009.

[76] G. F. P. Sanchez, A. Morales-Acevedo, B. R. Jackson*, et al.*, "Thin Film Bulk Acoustic Wave Resonators for their Application in Microwave Filters," *4th International Conference on Electrical and Electronics Engineering,* pp. 353-356, 2007.

[77] R. Kubo, H. Fujii, H. Kawamura*, et al.*, "Fabrication of 5GHz Band Film Bulk Acoustic Wave Resonators Using ZnO Thin Film," *IEEE Symposium on Ultrasonics*, pp. 166-169, 2003.

[78] Y. Aota, S. Tanifuji, H. Oguma*, et al.*, "FBAR Characteristics with AlN Film Using MOCVD Method and Ru/Ta Electrode," *IEEE Symposium on Ultrasonics,* pp. 1425-1428, 2007.

[79] T. Yokoyama, M. Hara, M. Ueda*, et al.*, "K-band Ladder Filters Employing Air-Gap Type Thin Film Bulk Acoustic Resonators," *IEEE Symposium on Ultrasonics,* pp. 598-601, 2008.

[80] K. Umeda, H. Kawamura, M. Takeuchi, *et al.*, "Characteristics of an AlN-Based Bulk Acoustic Wave Resonator in the Super High Frequency Range," *Vacuum,* vol. 83, pp. 672-674, 2008.

[81] M. Hara, T. Yokoyama, M. Ueda*, et al.*, "X-Band Filters Utilizing AlN Thin Film Bulk Acoustic Resonators," *IEEE Ultrasonics Symposium*, pp. 1152-1155, 2007.

[82] G. F. Pérez-Sánchez and A. Morales-Acevedo, "Electrode Optimization for Bulk Acoustic Wave Resonators Based on ZnO," *Materials Science and Engineering B: Solid-State Materials for Advanced Technology,* vol. 174, pp. 50-54, 2010.

[83] Q. Chen and Q.-M. Wang, "The Effective Electromechanical Coupling Coefficient of Piezoelectric Thin-Film Resonators," *Applied Physics Letters,* vol. 86, pp. 022904-022904-3, 2005.

[84] C. Chi-Jung and M. Z. Atashbar, "Finite Element Simulation of SMFBAR based Sensor," *IEEE International Conference on Electro/Information Technology*, pp. 190-195, 2009.

[85] C. Muller and M. A. Dubois, "Effect of Size and Shape on The Performances of BAW Resonators: A Model and Its Applications," *IEEE Symposium on Ultrasonics,* pp. 1552-1556, 2008.

[86] M. L. Johnston, I. Kymissis, and K. L. Shepard, "FBAR-CMOS Oscillator Array for Mass-Sensing Applications," *IEEE Sensors Journal,* vol. 10, pp. 1042-1047, 2010.

[87] G. Piazza, P. J. Stephanou, and A. P. Pisano, "AlN Contour-Mode Vibrating RF MEMS for Next Generation Wireless Communications," *Proceeding of the 36th European Solid-State Device Research Conference*, pp. 61-64, 2006.

[88] J. Hu, R. Parkery, R. Ruby, *et al.*, "A Wide-Ttuning Digitally Controlled FBAR-based Oscillator for Frequency Synthesis," *IEEE International Frequency Control Symposium,* pp. 608-612, 2010.

[89] D. Petit, E. Cesar, P. Bar, *et al.*, "Thermally Stable Oscillator at 2.5 GHz Using Temperature Compensated BAW Resonator and Its Integrated Temperature Sensor," *IEEE Ultrasonics Symposium,* pp. 895-898, 2008.

[90] P. Cong, T.-L. Ren, and L.-T. Liu, "A Novel Piezoelectric-based RF BAW Filter," *Microelectronic Engineering,* vol. 66, pp. 779-784, 2003.

[91] K. Dongsu, K. Dong Ho, R. Jong In, *et al.*, "A Quad-band Front-end Module for Wi-Fi and WiMAX Applications Using FBAR and LTCC Technologies," *Asia-Pacific Microwave Conference,* pp. 1-4, 2008.

[92] K. M. Lakin, "Thin Film Resonator Technology," *IEEE Transactions on Ultrasonics, Ferroelectrics and Frequency Control,* vol. 52, pp. 707-716, 2005.

[93] J. Hao, D. Shurong, and W. Demiao, "Design of Balanced RF Filter for Wireless Applications Using FBAR Technology," *IEEE Conference on Electron Devices and Solid-State Circuits*, pp. 57-60, 2005.

[94] O. Menendez, P. de Paco, R. Villarino, *et al.*, "Closed-Form Expressions for the Design of Ladder-Type FBAR Filters," *IEEE Microwave and Wireless Components Letters*, , vol. 16, pp. 657-659, 2006.

[95] M. Handtmann, S. Marksteiner, J. Kaitila, *et al.*, "Bulk Acoustic Wave Filters for GPS with Extreme Stopband Attenuation," *IEEE Microwave Symposium Digest*, pp. 371-374 Vol.1, 2004.

[96] C. Vale, J. Rosenbaum, S. Horwitz, *et al.*, "FBAR Filters at GHz Frequencies," *Proceedings of the 44th Annual Symposium on Frequency Control*, pp. 332-336, 1990.

[97] K. M. Lakin, G. R. Kline, and K. T. McCarron, "Thin Film Bulk Acoustic Wave Filters for GPS," *Proceedings Ultrasonics Symposium*, pp. 471-476 1992.

[98] K.-W. Kim, G.-Y. Kim, J.-G. Yook, *et al.*, "Air-Gap Type TFBAR-Based Filter Topologies," *Microwave and Optical Technology Letters,* vol. 34, pp. 386-387, 2002.

[99] M. e. Hassan, C. P. Moreira, A. A. Shirakawa, *et al.*, "A Multistandard RF Receiver Front-End Using A Reconfigurable FBAR Filter," *IEEE North-East Workshop on Circuits and Systems,* pp. 173-176, 2006.

[100] M. El Hassan, E. Kerherve, Y. Deval, *et al.*, "A Study on FBAR Filters Reconfiguration," *12th IEEE International Conference on Electronics, Circuits and Systems,* pp. 1-4, 2005.

[101] G. G. Fattinger, J. Kaitila, R. Aigner, *et al.*, "Thin Film Bulk Acoustic Wave Devices for Applications at 5.2 GHz," *IEEE Ultrasonics Symposium,* pp. 174-177, 2003.

[102] A. A. Shirakawa, J. M. Pham, P. Jarry, *et al.*, "Design of A Bulk Acoustic Wave Coupled-Resonator Filter Application in the WLAN band (5.15 - 5.35 GHz)," *IEEE MTT-S International Conference on Microwave and Optoelectronics*, pp. 117-120, 2005.

[103] K. M. Lakin, "Thin Film BAW Filters for Wide Bandwidth and High Performance Applications," *IEEE Microwave Symposium Digest,* vol.2, pp. 923-926, 2004.

[104] K. M. Lakin, "Bulk Acoustic Wave Coupled Resonator Filters," *IEEE International Frequency Control Symposium and PDA Exhibition,* pp. 8-14, 2002.

[105] W. P. Mason, *Electromechanical Transducers and Wave Filters*. New York: D. Van Nostrand, 1948.

[106] W. P. Mason, *Physical acoustics : Principles and Methods,* vol.1 A. New York: Academic Press, 1964.

[107] J. F. Rosenbaum, *Bulk Acouctic Wave Theory and Devices*. London: Artech House, 1988.

[108] D. S. Shim and D. A. Feld, "A General Nonlinear Mason Model and Its Application to Piezoelectric Resonators," *Int. J. RF Microw. Comput.-Aided Eng.,* vol. 21, pp. 486-495, 2011.

[109] K. M. Lakin, "Modeling of thin film resonators and filters," *IEEE International Microwave Symposium Digest*, pp. 149-152 1992.

[110] E. Schmidhammer, B. Bader, W. Sauer*, et al.*, "Design Flow and Methodology on The Design of BAW Components," *IEEE International Microwave Symposium Digest*, pp. 4, 2005.

[111] C. Min-Chiang, H. Zi-Neng, P. Shih-Yung*, et al.*, "Modified BVD-equivalent Circuit of FBAR by Taking Electrodes into Account," *Proceedings IEEE Symposium on Ultrasonics,* pp. 973-976, 2002.

[112] S. Sherrit, S. P. Leary, B. P. Dolgin*, et al.*, "Comparison of the Mason and KLM Equivalent Circuits for Piezoelectric Resonators in the Thickness Mode," *Proceedings IEEE Ultrasonics Symposium*, pp. 921-926, 1999.

[113] H. Jin, S. R. Dong, J. K. Luo*, et al.*, "Generalised Butterworth-Van Dyke Equivalent Circuit for Thin-Film Bulk Acoustic Resonator," *Electronics Letters,* vol. 47, pp. 424-426, 2011.

[114] T. Makkonen, A. Holappa, J. Ella*, et al.*, "Finite Element Simulations of Thin-Film Composite BAW Resonators," *IEEE Transactions on Ultrasonics, Ferroelectrics and Frequency Control,* vol. 48, pp. 1241-1258, 2001.

[115] J. E. A. Southin and R. W. Whatmore, "Finite Element Modelling of Nanostructured Piezoelectric Resonators (NAPIERs)," *IEEE Transactions on Ultrasonics, Ferroelectrics and Frequency Control,* vol. 51, pp. 654-662, 2004.

[116] S. Giraud, S. Bila, M. Aubourg*, et al.*, "Bulk Acoustic Wave Resonators 3D Simulation," *International Symposium on Signals, Systems and Electronics*, pp. 327-330, 2007.

[117] S. Adhikari, "Damping Models for Structural Vibration," PhD, Engineering Department, University of Cambridge, 2000.

[118] I. a. D. Chowdhury, S.P, "Computation of Rayleigh Damping Coefficients for Large Systems," *Electronic Journal of Geotechnical Engineering,* vol. 8, 2003.

[119] "FBAR Design Tutorial," *CoventorWare(R)2010, MEMS Design and Analysis Tutorials, Vol. 2*, 2010.

[120] M. T. Wauk, "Attenuation In Microwave Acoustic Transducer And Resonators," PhD, Applied Physics, Standford University, London, 1969.

[121] A. A. Shirakawa, J. M. Pham, P. Jarry, *et al.*, "Bulk Acoustic Wave Coupled Resonator Filters Synthesis Methodology," *European Microwave Conference,* , pp. 4, 2005.

[122] A. Ruimi, Y. Liang, and R. M. McMeeking, "Effect of Geometry on the Performance of MEMS Aluminum Nitride Trampoline Resonators in Longitudinal Resonance," *Journal of the Franklin Institute,* 2011.

[123] D. S. W. OR. (2003), *Overview of Smart Materials Technology*. Available: http://resources.edb.gov.hk/physics/articleIE/smartmaterials/SmartMaterials_e.htm,27 February 2013.

[124] K. M. Lakin and J. S. Wang, "Acoustic Bulk Wave Composite Resonators," *Applied Physics Letters,* vol. 38, pp. 125-127, 1981.

[125] "IEEE Standard on Piezoelectricity," *ANSI/IEEE Std 176-1987,* pp. 0_1, 1988.

[126] D. M. Pozar, "Microwave Network Analysis," *Microwave Engineering*, 2nd ed New York: John Wiley & Sons, pp. 206-237, 1988.

[127] T. Pensala, "Thin Film Bulk Acoustic Wave Devices," PhD, School of Science, Aalto University, Finland, 2011.

[128] J. Verdú, O. Menéndez, and P. de Paco, "Ladder-Type Filter Based on Bulk Acoustic Wave Resonators with Improved Out-of-Band Rejection," *Microwave and Optical Technology Letters,* vol. 50, pp. 103-107, 2008.

[129] G. G. Fattinger, "BAW Resonator Design Considerations - An overview," *IEEE International Frequency Control Symposium*, pp. 762-767, 2008.

[130] J. D. Larson, III, P. D. Bradley, S. Wartenberg, *et al.*, "Modified Butterworth-Van Dyke Circuit for FBAR Resonators and Automated Measurement System," *IEEE Ultrasonics Symposium*, pp. 863-868, 2000.

[131] F. D. Bannon, J. R. Clark, and C. T. C. Nguyen, "High-Q HF Microelectromechanical Filters," *IEEE Journal of Solid-State Circuits* vol. 35, pp. 512-526, 2000.

[132] O. Lewis and L. Chih-Shun, "Relationship of Resonant Frequency of Quartz Crystal to Mass Loading," *29th Annual Symposium on Frequency Control. 1975*, pp. 5-9, 1975.

[133] J. Kosinski, S. Mallikarjun, and A. Ballato, "Mass Loading Measurements of Quartz Crystal Plates," *Proceedings of the 43rd Annual Symposium on Frequency Control*, pp. 365-371, 1989.

[134] K. M. Lakin, G. R. Kline, and K. T. McCarron, "Development of Miniature Filters for Wireless Applications," *IEEE Transactions on Microwave Theory and Techniques* vol. 43, pp. 2933-2939, 1995.

[135] O. Heaviside, "Electromagnetic Induction and Its Propagation," *The Electrician,* 1885,1886 and 1887.

[136] J.-M. Kang, "Piezoelectric MEMS Resonator Characterization and Filter Design," Master Thesis, Massachusetts Institute of Technology, 2004.

[137] K. Kun-Wook, G. Myeong-Gweon, Y. Jong-Gwan, *et al.*, "Resonator Size Effects on the TFBAR Ladder Filter Performance," *IEEE Microwave and Wireless Components Letters,* vol. 13, pp. 335-337, 2003.

[138] "Overview in Using CoventorWare," *CoventorWare (R) 2010,* 2010.

[139] D. A. Berlincourt, D. R. Curran and H. Jaffe, "Piezoelectric and Piezomagnetic Materials and Their Function in Transducers," *Physical Acoustic*. vol. 1 Pt. A, ed New York: Academic Press, 1964.

[140] J. D. Larson, III and Y. Oshrnyansky, "Measurement of Effective k_t^2, Q, R_p,R_s vs. Temperature for Mo/AlN FBAR Resonators," *Proceedings. IEEE Symposium on Ultrasonics*, pp. 939-943, 2002.

[141] F. Z. Bi and B. P. Barber, "Bulk Acoustic Wave RF Technology," *IEEE Microwave Magazine,* vol. 9, pp. 65-80, 2008.

[142] L. Y. George L. Matthaei, E. M. T. Jones, *Microwave Filters, Impedance-Matching Networks and Coupling Structures*. New Jersey: Artech House, 1980.

[143] K. M. Lakin, J. Belsick, J. F. McDonald*, et al.*, "Improved Bulk Wave Resonator Coupling Coefficient for Wide Bandwidth Filters," *IEEE Ultrasonics Symposium*, pp. 827-831, 2001.

[144] T. N. M. Ueda, S. Taniguchi, T. Yokoyama, J. Tsutsumi, M. Iwaki, and Y. Satoh, "Film Bulk Acoustic Resonator using High-Acoustic-Impedance Electrodes," *Jpn. J. Appl. Phys.,* vol. 46, pp. 4642-4646, 2007.